# Multiphase Flow
# Computational & Experimental Methods

Editors:
**S. Hernández
& P. Vorobieff**

**WIT**PRESS

# Multiphase Flow

**WIT**PRESS

WIT Press publishes leading books in Science and Technology.
Visit our website for the current list of titles.
www.witpress.com

**WIT**eLibrary

Home of the Transactions of the Wessex Institute.
The WIT electronic-library provides the international scientific community with immediate
and permanent access to individual papers presented at WIT conferences.
http://library.witpress.com

*This page intentionally left blank*

# Multiphase Flow

## Computational & Experimental Methods

**Editors**

**S. Hernández**
*University of A Coruña, Spain*

**P. Vorobieff**
*University of New Mexico, USA*

**WIT**PRESS  **Southampton, Boston**

**Editors:**


**S. Hernández**
*University of A Coruña, Spain*

**P. Vorobieff**
*University of New Mexico, USA*

*The texts of the papers in this volume were set individually by the authors or under their supervision. Only minor corrections to the text may have been carried out by the publisher.*

# Preface

The research included in this volume focuses on using synergies between experimental and computational techniques to gain a better understanding of all classes of multiphase and complex flow. The included papers illustrate the close interaction between numerical modellers and researchers working to gradually resolve the many outstanding issues in our understanding of multiphase flow.

Recently multiphase fluid dynamics have generated a great deal of attention, leading to many notable advances in experimental, analytical and numerical studies. Progress in numerical methods has permitted the solution of many practical problems, helping to improve our understanding of the physics involved.

Multiphase flows are found in all areas of technology and the range of related problems of interest is vast, including astrophysics, biology, geophysics, atmospheric process, and many areas of engineering.

The Editors

*This page intentionally left blank*

# Contents

# X-RAY TOMOGRAPHY RECONSTRUCTION OF MULTIPHASE FLOWS AND THE VERIFICATION OF CFD

SANDY BLACK & MARC LAING
TUV SUD NEL, East Kilbride, Scotland.

### ABSTRACT

Experimental studies using an X-ray tomography system were performed on a 4-inch horizontal section of the multiphase flow loop at NEL for gas–water and gas–oil–water flows. Values of liquid holdup and water liquid ratio are reported alongside analysis of the phase linear fraction through the cross-section of the pipe. The X-ray system revealed areas of gas entrainment and separation of oil and water which are not evident from high-speed video footage. The flow pattern of the tests was stratified-wavy, and computational fluid dynamics (CFD) analysis was performed using the volume of fluid (VOF) method. The prediction of liquid holdup and gas distribution through the pipe height as determined by CFD, correlated well with that determined by X-ray tomography. However, the results suggest that a transient VOF with a high-order mesh resolution is required to account for gas entrainment. This study shows that an X-ray system can be utilised to provide quantifiable validation data which are of value to multiphase models in CFD and provide insight that is not apparent during high-speed video analysis. The data generated from this system will be of considerable value to multiphase flow specialists and instrumentation developers.

*Keywords: CFD, Multiphase, Void fraction, Tomography, X-Ray.*

## 1 INTRODUCTION

Experimental measurements of multiphase flows have been extensively studied in the literature for horizontal pipes [1] and vertical pipes [2]. From this information, flow pattern or flow regime maps have been generated through empirical relationships or mechanistic models [3,4] which are widely used today. For example, Mandhane *et al*. [4] identified six flow regimes in horizontal flow based on the superficial gas and liquid velocities, namely stratified, wavy, annular, bubble, slug and dispersed flow. The characteristics of these flow regimes may be simple, such as stratified flow where liquid flows at the bottom of the pipe and gas flows at the top or unsteady which can transition between regimes. An example would be slug flow where large gas bubbles are separated by pockets of liquid that fill the pipe, known as slugs. To determine these flow regimes, a typical approach is to use videos or photographs from laboratory test data. This approach can be highly subjective and more recently, sophisticated instrumentation such as high-speed video, gamma densitometry, electrical resistance probes and fast response X-ray tomography have been used to produce quantitative data. Subsequently, these data can be used to develop, verify, and validate models such as those used in computational fluid dynamics (CFD) with better accuracy [5].

The focus of this paper is to utilise an X-ray tomography system for the primary purpose of better understanding multiphase flows and verifying CFD simulations. The device reconstructs a 2D cross-sectional digital image of the flow field through computerised tomography (CT) and shows the distribution of gas, oil and water within the pipe. Moreover, the system delivers 'real-time' qualitative and quantitative data such as void fraction and water liquid ratio (WLR). Experimental measurements using the X-ray tomography system of gas–water and gas–water–oil flows were conducted in NEL's multiphase flow loop in a 4-inch horizontal section of pipework followed by multiphase CFD simulations. This approach is a significant improvement on the subjective nature of using a high-speed camera and an

engineer to determine the flow regime and evaluate the limitations of the models. Utilising this technology allows verification of CFD models to a higher degree of confidence than with previous approaches.

A description of the X-ray system is given in Section 2 followed by the description of the test facility and selected experimental results in Sections 3 and 4, respectively. A comparison of CFD predictions against the X-ray measurements is given in Section 5 followed by conclusion in Section 6.

## 2 X-RAY TOMOGRAPHY SYSTEM

Within a multiphase flow, the gas, oil and water will typically attenuate an X-ray beam at different rates due to the different attenuation coefficients of the media. This measurement provides a means to indicate the flow pattern and structure of a multiphase flow through pipework provided the attenuation of the gas, oil and water is sufficiently different [6]. The use of X-ray imaging can generally deliver measurements at higher sampling rates and spatial distribution compared to other non-invasive methods such as electrical capacitance tomography and gamma densitometry [6]. If more than one X-ray measurement is taken from different angles, the images can be numerically reconstructed to provide a computed tomography (CT) image. For the purposes of multiphase flow within a pipe, this would represent a 2-D cross section of the flow.

The REX-CELL™ 2X-RCN system designed by FlowCapture® is a commercially available non-invasive measurement device that uses X-ray CT techniques to characterise gas–oil–water in multiphase flows and is to some extent analogous to that proposed by Hu *et al*. [6]. The system can be installed in non-metal circular pipes up to 6 inches in diameter and 16 mm in thickness at inclinations between −90° and +90°. As shown in Fig. 1(a), the X-ray system consists of two independent sources and X-ray cameras which are oriented vertically and horizontally to the pipe. System operation, data acquisition and real-time data processing of the void fraction, liquid holdup and CT image is processed through a PC with the software, FlowDiary™. A collimator is used near the two X-ray sources to narrow the original cone-shaped beam to a rectangular beam. The X-ray cameras are positioned 140 mm from the centre of the pipe and are based on complementary metal-oxide-semiconductor
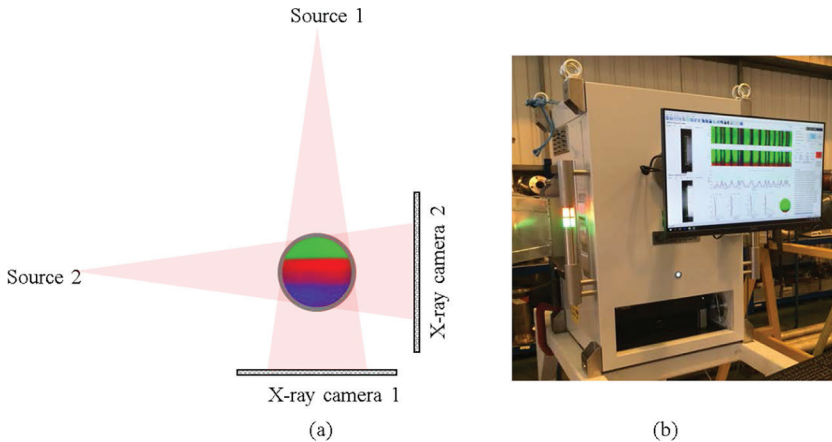


Figure 1: X-Ray tomography system: (a) schematic diagram, (b) installed system.

image sensor technology with an effective pixel area of 3024 × 864 pixels (74.8 μm × 74.8 μm pixel size). At this resolution, a maximum of 60 frames per second (fps) can be achieved, however when 4 × 4 pixel binning is considered a maximum of 191 fps can be achieved albeit with a reduced resolution of 768 × 216 pixels.

The system is installed over the pipe and is enclosed in lead shielding for safety as shown in Fig. 1(b). An X-ray must have sufficient power to penetrate the wall thickness, however at higher powers the attenuation of oil and water is similar which therefore becomes problematic when trying to distinguish between gas, oil and water in multiphase flows. Steel pipes typically have a higher attenuation than glass, Perspex or other composite pipes however cannot withstand higher pressures. For this reason, a fibre-reinforced thermoplastic polyether ether ketone (PEEK) carbon composite pipe was used which is rated to over 300 bar. The PEEK composite material is a commercially available alternative to traditional steelwork for the oil and gas industry with benefits in weight, erosion and corrosion resistance. The material provides the strength without compromising on wall thickness and is acquired for future experiments at pressures up to 140 bar in NEL's Advanced Multiphase Facility.

For all of the test conditions reported in this paper, the system was operated at 60 kV and 3.3 mA with a sampling frequency of 40 fps. The key output of the X-ray device is the phase area fraction (PAF) of the gas, water and oil. Calibration of the device is achieved at these settings by filling the line with gas, followed by water and then oil at the same pressures and temperatures expected during the test programme.

A typical result for a gas–oil–water test is shown in Fig. 2. The instantaneous processed data over a 5 min test period from the X-ray is shown in Fig. 2(a) where the colours green, red and blue represent gas, oil and water, respectively. The top and middle graphs from top to bottom represent the instantaneous calculated fraction of gas, oil and water from the top and side X-ray cameras, respectively. At each instant, a CT image is produced as illustrated in Fig. 2(c) where various slugs and other flow structures are also captured. The 3D image in Fig. 2(c) is constructed from each of the CT images. At each sample time, a PAF of the gas, oil and water fraction can be computed which is illustrated in the bottom graph of Fig. 2(a). The average PAF can then be computed over the sample period therefore giving information
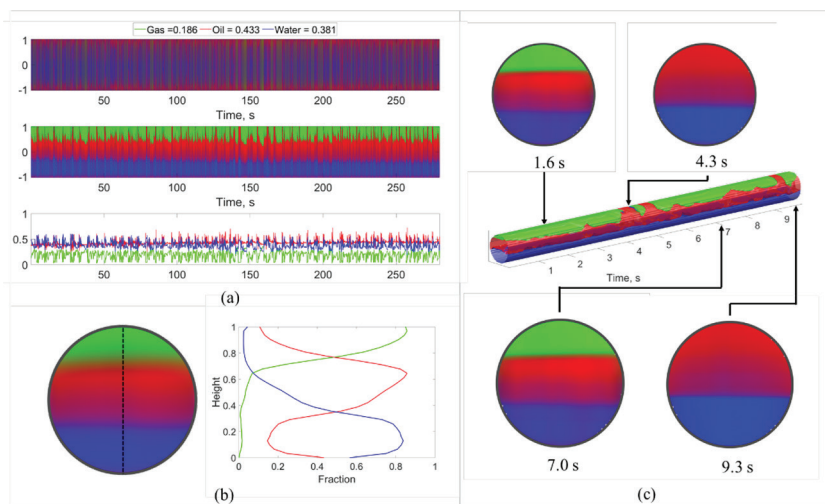


Figure 2: Typical output from X-ray device.

on gas void fraction, liquid holdup and WLR. Additionally, information regarding the distribution through the pipe can be extracted from the CT plots, as shown in Fig. 2(b) where the gas, oil and water fractions are shown with respect to pipe height. Clearly, in this situation gas is at the top of the pipe whilst in the liquid layer at the bottom of the pipe, the lighter density oil is separated from the water.

## 3  EXPERIMENTAL SETUP

The NEL Multiphase Facility is based around a three-phase separator which contains the working bulk liquid. The oil and water are re-circulated around the test facility using two variable speed pumps and nitrogen is used as the gas phase and can deliver up to 0.5 kg/s by evaporation of liquid nitrogen on demand. The delivery pressure of the nitrogen is up to 17 bar at the reference measurement location and after passing through the test section, nitrogen is exhausted to atmosphere from the separator.

The test section can accommodate test set-ups of lengths up to 60 m horizontal and 12 m vertical. Piping and adaptors are available to allow testing of 2, 3, 4 and 6-inch pipework and flow metres. The facility is manufactured entirely from stainless steel and is therefore capable of flowing brine substitutes and dead crude oils as the working fluids in addition to de-ionised water and refined oils. Perspex visualisation sections are also available in 2, 4 and 6-inch pipe sizes to allow for visual analysis of flow patterns which can be equipped with high-speed cameras to record the flow.

The test section used for the experimental test campaign and the corresponding dimensions are shown in Fig. 3:. The multiphase mixtures were introduced into a 2-inch Schedule 40 pipe and passed through a jet mixer to provide a uniform mixture condition at the inlet of the test section. The pipework was then orientated in a vertical loop of approximately 2 m in height. On the vertical pipework where the flow would be flowing downwards, the pipe size was increased to a 4-inch schedule 40 pipe (inner diameter of 102.26 mm). After the vertical bend, a 2.75 m section of 4-inch schedule 40 pipe was positioned before a 1.05 m Perspex viewing section. A high-speed camera of 120 fps was positioned at this location to provide visual flow patterns. A further 2 m of 4-inch pipe was placed before a 1 m length section of 4-inch PEEK pipe and the X-ray device was installed.

The fluids used in the test were nitrogen, a synthetic oil (Paraflex HT9) and an aqueous solution of magnesium sulphate and were typically performed at 10 bar. Typical properties of the gas, oil and water are given in Table 1.

An extensive number of test points were recorded as part of research undertaken for the UK's National Measurement System Flow Programme [7]. A selection of these test points examined in this paper is shown in Table 2. Tests 155, 158 and 159 are gas–water tests which correspond to gas volume fractions (GVFs) of 73%, 51% and 23%, respectively. Tests 208,
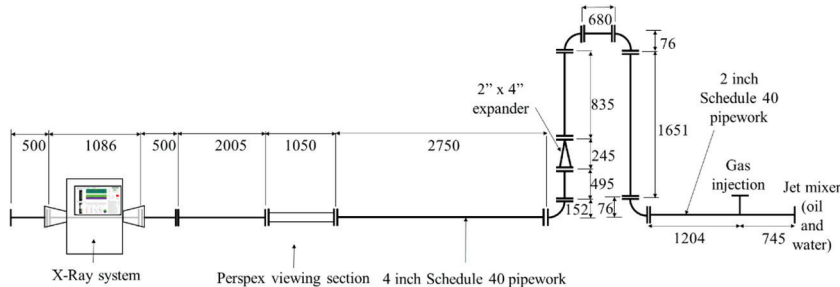


Figure 3: Line build.

Table 1: NEL Fluid Properties (20°C, 10 bar(a)).

|  | Gas | Oil | Water |
|---|---|---|---|
| Fluid | Nitrogen | Paraflex HT9 | $MgSO_4$ $7H_2O$ solution |
| Density (kg/m$^3$) | 12.7 | 830.0 | 1050.0 |
| Viscosity (cP) | $1.7710^{-2}$ | 16.00 | 1.30 |

Table 2: Test matrix.

| Test | Flow rate (m³/h) | | | GVF | WLR |
|---|---|---|---|---|---|
|  | Gas | Oil | Water | % | % |
| 155 | 41.72 | – | 8.76 | 82.6 | 100 |
| 158 | 25.17 | – | 23.86 | 51.3 | 100 |
| 159 | 10.70 | – | 35.61 | 23.0 | 100 |
| 208 | 42.06 | 4.51 | 4.34 | 82.6 | 49.0 |
| 205 | 23.43 | 11.36 | 11.44 | 50.6 | 50.2 |
| 218 | 10.82 | 24.86 | 10.95 | 23.2 | 30.6 |

205 and 218 correspond to gas–water–oil tests with GVF ratios of 83%, 51% and 23%, respectively with WLR of 49%, 50%, 30.6%.

## 4  EXPERIMENTAL RESULTS

### 4.1  Absolute error

To assess the absolute error of the X-ray tomography system, non-flowing (i.e. static) tests were performed. A known volume of fluid (VOF) was placed into a 3-inch sealed test section and placed into the X-ray system where a comparison between the absolute phase area average fractions of gas, oil and water was assessed. The absolute error of the system was shown by Black [7] to be within 3% and 5% for gas–liquid and gas–oil–water tests, respectively, which agrees with similar X-ray systems [6].

### 4.2  Two-phase results

Two-phase results of gas–water mixtures from the X-ray tomography system and snapshots from high speed videos are presented in Fig. 4 for tests 155, 158 and 159 which correspond to GVFs of 23%, 50%, 83%, respectively. The corresponding average PAFs over each 1 min test are shown in Table 3.

Fig. 4 clearly shows that the liquid holdup from the videos correlates well with the level predicted by the X-ray. For Test 155 (23% GVF), the video observation shows the flow is stratified-wavy (Fig. 4(a)) and this is captured by the small amplitude peaks in the X-ray output (Fig. 4(b)). The videos in Fig. 4(c)–(e) show that for higher GVF values of 52% and 83%, the waves hit the top of the pipe, with this occurring more frequently for the higher GVF test (Test 159). The output from the X-ray shows a drop in the gas content around 25 s
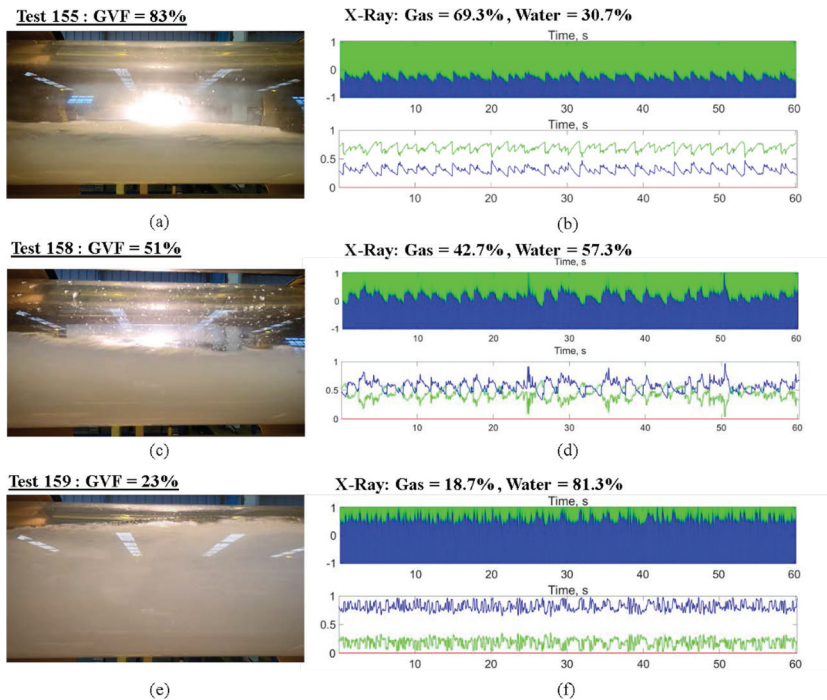
Figure 4: Two-phase gas water X-ray measurements and photographs for GVF of (a and b) 83%, (c and d) 50%, (e and f) 23%.

Table 3: PAF results for gas, oil and water for the multiphase tests.

| Test | X-ray PAF | | | Superficial velocities (m/s) | | |
|---|---|---|---|---|---|---|
| | Gas | Oil | Water | Gas | Oil | Water |
| 155 | 69.3 | – | 30.7 | 1.41 | – | 0.30 |
| 158 | 42.7 | – | 57.3 | 0.36 | – | 1.20 |
| 159 | 18.7 | – | 81.3 | 0.85 | – | 0.81 |
| 208 | 53.5 | 28.8 | 17.8 | 1.42 | 0.15 | 0.15 |
| 205 | 36.9 | 34.1 | 29.0 | 0.79 | 0.39 | 0.38 |
| 218 | 17.0 | 54.9 | 28.1 | 0.37 | 0.37 | 0.84 |

and 50 s for Test 158 (Fig. 4(d)), whereas this occurs regularly in Test 159 (Fig. 4(f)) due to the high VOF in the pipe.

The GVF in Table 2 is calculated from reference flow metres which are located approximately 600 pipe diameters upstream of the X-ray device. Experimental tests are run for a sufficient period to allow the flow to move completely through the system before flow rates are sampled. Due to the slip between the gas and the liquid, local liquid holdup can occur within the test section. Comparing the GVF in Table 2 with the gas void fraction measured by the X-ray in Table 3, the values from the X-ray are lower therefore giving a holdup of liquid within this section. To quantify the degree of slip, the slip ratio, $S$, can be used:

$$S = U_G \left(1 - \varepsilon_G\right)/U_L \varepsilon_G$$

(1)

where $U_G$ and $U_L$ are the superficial velocities of the gas and liquid based on a 4-inch pipe (I.D. 102.26 mm), respectively, as given in Table 3 and $\varepsilon_G$ is the gas void fraction measured by the X-ray. The slip ratio is calculated as 2.1, 1.4 and 1.3 for Tests 155, 158 and 159 which correspond to decreasing liquid-hold ups for the corresponding tests, i.e. the difference between the GVF measured at the reference meters and the X-ray are 13%, 9% and 4% for Tests 155, 158 and 159, respectively.

The corresponding distribution of gas and liquid over the height of the pipe is shown in Fig. 5. An interesting observation is made where the liquid at the bottom of the pipe shows that some gas entrainment has occurred. As discussed by Hu *et al.* [6], gas entrainment is a strong function of liquid and gas flow rates. Upstream of the X-ray system, the gas enters at a 90° angle to the water which has passed through a jet-mixer before being carried through a vertical U-bend. During this period, it is likely that a high degree of turbulent mixing of the gas into the liquid would occur, more notable for higher gas flow rates which is evident in Fig. 5.

### 4.3  Gas–oil–water results

There is a significant volume of work related to two-phase slug flows. However only a limited number of publications on three-phase X-ray results [6,7] are available. Gas–oil–water results from the X-ray and snapshots from high-speed videos are presented in Fig. 6 for Tests 208, 205 and 218 with GVF of 83%, 51% and 23%, respectively, with WLR of 49%, 50%, 30.6%. The corresponding average PAFs over each 1 min test are shown in Table 3.

Fig. 6 clearly shows similar trends compared to the two-phase results with similar GVF ratios where a stratified-wavy flow pattern is present in the videos and predicted by the X-ray. Small amplitude peaks are present which touch the top of the pipe more frequently as the GVF ratio is lowered. From the videos it is not clear if the water and oil are well mixed or have separated to some degree.

Comparing the GVF calculated from the reference flow metres in Table 2 against the gas PAF from the X-ray shows larger differences for higher GVF ratios of 29%, 14% and 6% for GVF of 83%, 51%, and 23% (i.e. Test 208, 205 and 218, respectively). Using the reference meter flow rates and assuming water and oil and uniformly mixed, the slip ratio is 4.1, 1.8 and 1.5 which relates to the trend of liquid holdup observed by the X-ray.

The time-average phase linear fraction from the X-ray is shown in Fig. 7 and shows that the distribution of gas (green) oil (red) and water (blue). As the data are averaged over the test period, the gas fraction is not equal to 1 in Test 205 and 218 (Fig. 7(b) and (c)) due to waves
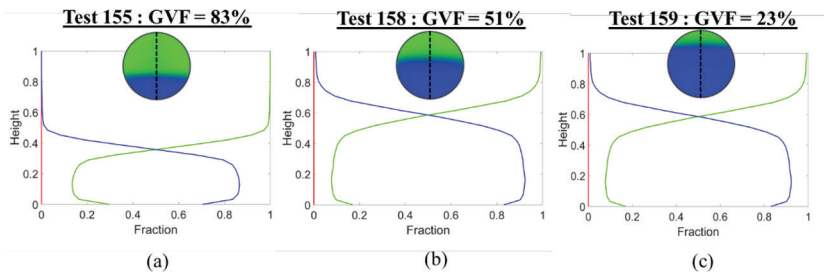


Figure 5: Two-phase gas water X-ray measurements over the height of the pipe for (a) Test 155, (b) Test 158 and (c) Test 159.
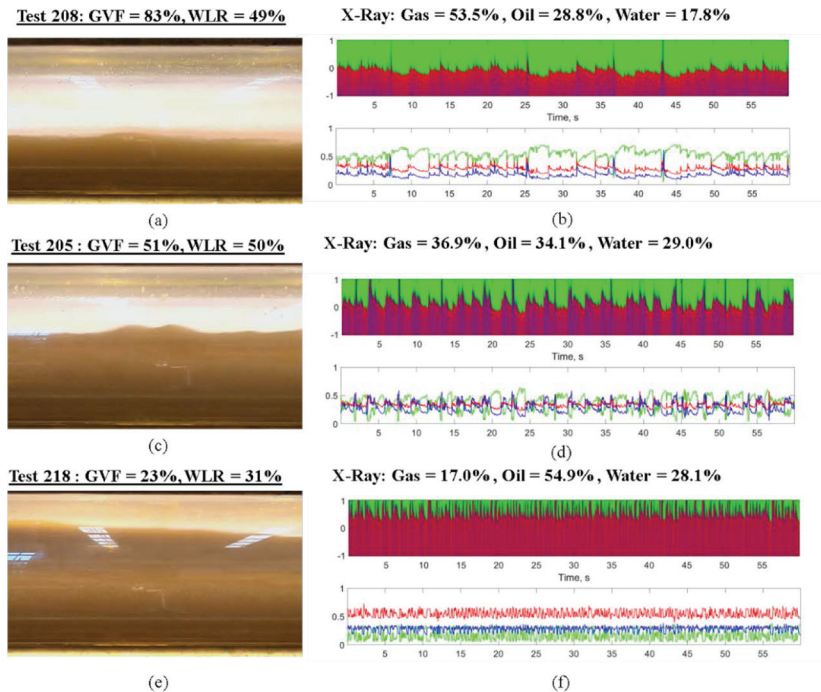
Figure 6: Gas–oil–water X-ray measurements and photographs
for (a) Test 208; (b) Test 205 and (c) Test 218.
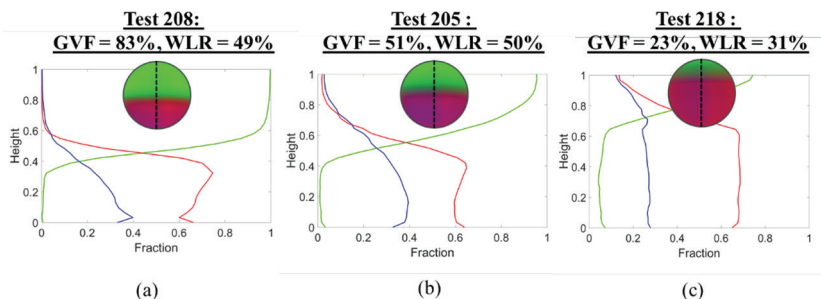


Figure 7: Gas–oil–water X-ray measurements over the height of
the pipe for (a) Test 208; (b) Test 205 and (c) Test 218.

hitting the top of the pipe as shown by the small amplitude fluctuations in Fig. 6(d) and (f).
The distribution of oil and water at the bottom of the pipe is only shown to be uniform in Test
218 (Fig. 7(c)). Peaks of oil are shown near the centre of the pipe in Fig. 7(a) and (b) for Test
208 and 205. This is due to the separation of the water and oil as the effects of gravity and
surface tension dominate over the momentum of the flow. From the flow rates in Table 2, it is
clear that Test 218 has the highest flow rates and therefore the X-ray results suggest sufficient
turbulent mixing is still present, as shown by the uniform distribution in the liquid layer
in Fig. 7(c).

## 5  CFD MODEL

### 5.1  Set-up

The commercial CFD software, ANSYS Fluent 19.1 with the VOF approach [8] was used to model the interaction between the gas and the liquid with a sharp/dispersed interface scheme. The VOF method assumes that the fluids are immiscible and solves a single set of momentum equations where a volume fraction for each fluid is transported through the domain. The VOF method is a common approach for multiphase flow CFD and has been evaluated against flow pattern maps and various experimental measurements and observations [9,10]. Surface tension was also included with the continuum surface force model [11] and constant values of 72 and 34 dynes/cm for gas–water/oil interfaces for oil–water mixtures was used, respectively. The effects of wall adhesion were not considered.

### 5.2  Geometry and mesh

A three-dimensional geometry was used which represented a segment of the test facility. The geometry consisted of two separate 2-inch inlets for the gas and liquid with a vertical 'U' bend which expands into a 4-inch section. The position of the X-ray on the model was the same as the experimental location. Initially, two fully structured meshes were evaluated for Test 155, namely mesh 1 and mesh 2 consisting of 1.6 million cells with an average cell size of 4.3 mm and 3.0 million cells with an average cell size of 3.5 mm, respectively. Mesh 1 and 2 predicted a liquid hold-up 69.4% and 68.9%, respectively. As the liquid hold-up values are with 5%, which is the limit of the X-ray equipment, mesh 1 was used for the remaining simulations.

### 5.3  Solution procedure

An initial transient simulation was performed for Test 155 which showed transient effects in the vertical U-bend but these were dampened by the location of the X-ray device. Instead a steady-state solution was used. This is also preferred as this method can be applied more readily to the near industrial-scale simulations. The tracking of the interface was solved using an implicit time discretisation and a coupled algorithm with a first-order upwind scheme for momentum and compressive scheme for the volume fraction was used. The k–$\omega$ SST model with turbulence damping coefficient of 10 was used for turbulence.

### 5.4  CFD results

#### 5.4.1  Two-phase results
Fig. 8(a), (b), (c) shows Tests 155, 158 and 159, respectively. A comparison between the time-averaged X-ray CT image and the steady-state CFD analysis for all of the cases in Fig. 8 compare well and the phase averaged values are within 4% as shown in Table 4. As discussed previously, Fig. 8 shows a degree of gas and liquid entrainment in each test which is not accounted for in the CFD model as the VOF method inherently assumes that the two fluids are immiscible. Despite this assumption, the liquid levels agree relatively well. The CFD analysis typically has a sharper gradient along the height of pipe which is due to the steady-state approximation and will not replicate a wavy stratified flow.
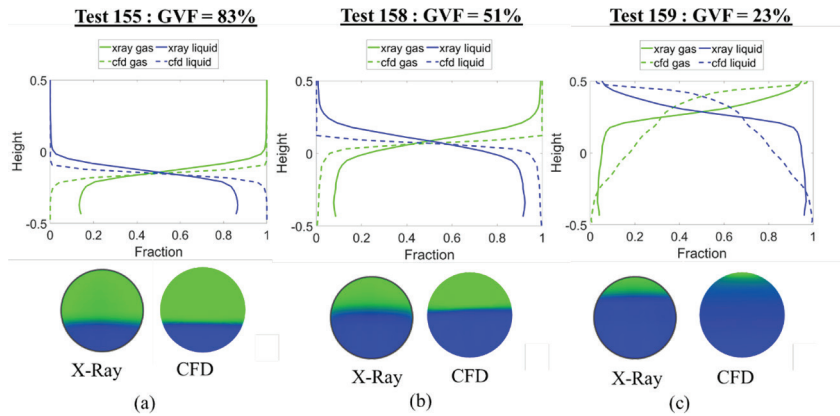
Figure 8: Results for Test case 155 showing (a and b) X-ray results and (b) CFD results.

Table 4: Absolute error between the X-ray and CFD simulations.

| Test | Absolute difference (%) | | |
|---|---|---|---|
| | Gas | Oil | Water |
| 155 | 0.1 | | −0.1 |
| 158 | −3.7 | | 3.7 |
| 159 | 1.3 | | −1.3 |
| 208 | 0.3 | −5.2 | 4.8 |
| 205 | −7.1 | 0.9 | 6.2 |
| 218 | 1.3 | 1.8 | −3.1 |

5.4.2  Three-phase results

Fig. 9 shows the comparison between the X-ray measurements and the CFD simulations for Tests 208, 205 and 218. The prediction from the VOF model matches the output from the X-ray relatively well as shown by comparing the X-ray CT image and cross-sectional from the CFD simulation in Fig. 9. Slight differences occur in the linear phase area gas fractions in Fig. 9 in the upper half of the pipe due to the wavy nature of the flow and the steady-state CFD analysis which only represents an ensemble of realisations (i.e. Reynolds averaging). It is important to reiterate that the inlet to the model is the exit of a jet mixer and it is assumed that the oil and water are well mixed. From the video evidence, it is suggested that at this point, the water and oil are well mixed; however, the X-ray shows otherwise. Relying on video evidence would lead to the choice of a steady-state implicit VOF approach. However, it is known to not be accurate when surface tension effects are important and is naturally diffusive. When the oil and water remain well mixed, this method is suitable for some gas–oil–water flows such as Test 218 (Fig. 9(c)), however this is inappropriate when the phases separate further downstream of the inlet.
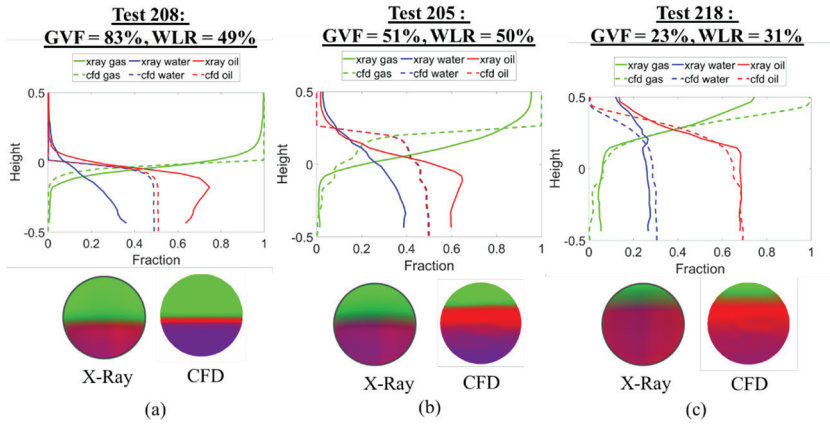
Figure 9: Results for Test case 218 showing (a and b) X-ray results and (c and d) CFD results.

## 6  CONCLUSION

Performing more detailed measurements of complex multiphase flows are of vital importance in aiding the understanding of multiphase flow model development. This study shows that an X-ray system can be utilised to provide quantifiable validation data which is of value to multiphase models in CFD and provide insight that is not apparent during high-speed video analysis. Measurements using an X-ray system were conducted on a 4-inch horizontal section of NEL's multiphase flow facility for nitrogen–water and nitrogen–oil–water flows where values of liquid holdup and water liquid ratio were examined. This also included the analysis of phase linear fraction through the cross-section of the pipe to reveal areas of gas entrainment in the liquid and the initial separation of oil and water within oil–water flows. The VOF was examined to compare against the X-ray measurement and adequately captured the gas void fraction for the test cases examined. The model was not capable of predicting regions of gas entrainment and oil and water separation as captured by the X-ray system. Further model investigations should include a transient VOF with a high-order mesh resolution to attempt to capture gas entrainment.

The analysis generated from the X-ray tomography device will help resolve the limitation in current CFD modelling techniques of multiphase flows and will be of considerable value to multiphase flow specialists and instrumentation developers.

## ACKNOWLEDGEMENTS

## REFERENCES

[1]  Hall, A.R.W., Flow Patterns in Horizontal Three-Phase Flows of Oil, Water and Gas. *Proceedings of Multiphase 1997,* 1997.

[2]  Beggs, D.H. & Brill, J.P., A Study of Two-Phase Flow in Inclined Pipes. *Journal of Petroleum Technology*, **25(5)**, pp. 607–617, 1973.

[3]  Baker, O., Simultaneous Flow of Oil and Gas. *Oil and Gas Journal*, **53**, pp. 185–190, 1954.

[4]  Mandhane, J.M., Gregory, G.A. & Aziz, K., A Flow Pattern Map for Gas-Liquid Flow in Horizontal Pipes. *International Journal of Multiphase Flow*, **1**, pp. 537–553, 1974.

[5]  Hill, T.J., Research in multiphase flow developed into new global discipline of flow assurance—an oil industry perspective. *Proceedings of the 11th North American Conference on Multiphase Technology*, 2018.

[6]  Hu, B., Langsholt, M., Liu, L., Andersson, P. & Lawrence, C., Flow structure and phase distribution in stratified and slug flows measured by X-ray tomography. *International Journal of Multiphase Flow*, **67**, pp. 162–179, 2014.

[7]  Black, S., Commissioning and Initial Performance of an X-ray tomography Device, *NEL Report Number 2018/559*, 2019.

[8]  Hirt, C.W. & Nichols, B.D., Volume of Fluid (VOF) method for the dynamics of free boundaries. *Journal of Computational Physics*, **39(1)**, pp. 201–225, 1981.

[9]  De Schepper, S.C.K., Heynderickx, G.J. & Marin, G.B., CFD modelling of all gas-liquid and vapor-liquid flow regimes predicted by the Baker chart. *Chemical Engineering Journal*, **138(1–3)**, pp. 349–357, 2008.

[10]  Parvareh, A., Rahimi, M., Alizadehdakhel, A. & Alsairfai, A.A., CFD and ERT investigations on two-phase flow regimes in vertical and horizontal tubes. *International Communications in Heat and Mass Transfer*, **37(1)**, pp. 304–311, 2010.

[11]  Brackbill, J.U., Kothe, D.B. & Zemach, C., A Continuum Method for Modelling Surface Tension. *Journal of Computational Physics*, **100(1)**, pp. 335–354,1992.

# EFFECT OF GAP ON THE FLOW CHARACTERISTICS IN THE WAKE OF A BLUFF BODY NEAR A WALL

G. NASIF, R. BALACHANDAR & R. M. BARRON
University of Windsor, Ontario, Canada.

## ABSTRACT

A numerical investigation is carried out to evaluate the influence of the gap between the bluff body and the bed on the wake characteristics generated in shallow flows. A sharp-edge bluff body with a fixed gap from the bed is employed in the study, and the results are compared with the no gap case. A sharp-edged bluff body was chosen to minimize the effect of Reynolds number and ensure fixed flow separation points. The transient three-dimensional Navier–Stokes equations are numerically solved using a finite volume approach with the detached eddy simulation turbulence model. The flow field in this study involves two different fluids, i.e. water and the air above it. The volume of fluid method is used for tracking the free surface separating the water and air. The fluid structures that are generated in the wake are identified using the $\lambda_2$-criterion. The results reveal that the gap flow will develop a new structure near the bed, which enhances the upwash flow immediately after the submerged jet is about to turn upwards due to the weak hydraulic jump. This structure plays an important role in recovering the free surface to its original shape at a shorter downstream distance from the bluff body than when there is no gap.

Keywords: *free surface, Navier–Stokes equation, numerical simulation, turbulent models, two-phase flow, viscous flow, wake flow, wall jet.*

## 1 INTRODUCTION

In shallow flow, the clearance between the ground and obstacles can considerably influence the wake flow characteristics. Examples of this type of flow are often found in engineering applications, e.g. the airflow around solar panels, flow around vehicles and the cooling of electronic components. Many investigations have been carried out with circular and square cylinders as a bluff body to examine the influence of the gap on the wake characteristics [1–5]. All these studies agree that the gap alters the wake characteristics if it is introduced in the wake flow. Shinneeb and Balachandar [6–8] carried out an experimental investigation using PIV to determine the gap height effect on the turbulent shallow wake generated by a vertical sharp-edged flat plate suspended in a shallow channel flow. The study disclosed that the size of the wake in the near-bed locations increases with the increase of the gap height as the gap flow enhances the lateral entrainment. The results also revealed that if the gap flow is weak and there is insufficient momentum to overcome the influence of the recirculation, the flow is engulfed by the recirculation zone formed just behind the bluff body. If the gap flow is relatively strong, it penetrates in the downstream direction, and only a portion of it is deflected upwards to feed the recirculation zone.

The main objective of the current study is to numerically assess the effect of the gap flow between the base of the sharp-edge bluff body and the open channel bed on the fluid structures in the wake at near-bed locations. These structures define the downstream location where the free surface restores its original shape behind the bluff body. The final goal of the numerical study is to provide an enhanced analysis not yet possible from the recent experimental studies. A three-dimensional time-dependent detached eddy simulation (DES) is used as the turbulence model in the study. Available data from previous PIV experiments [6–7] are used to validate the numerical results.

## 2  MODEL SETUP AND COMPUTATIONAL METHOD

Figure 1a is used as the computational domain to obtain an enhanced picture of the effect of the gap on the wake flow in this study. The incoming flow is a fully developed boundary layer type and is sheared in the vertical direction. This boundary layer type of flow can be destabilized by a sudden change of topology, introduction of horizontal shear or deceleration of the flow. In the present study, the destabilizing (and as a result, the wake) is generated by inserting a vertical sharp-edged plate in the open channel as shown in Fig. 1. The plate of width $D = 30$ mm is adjusted vertically to create different clearances with the bed, namely, $h/H = 0.0$ and 0.1, where $h$ is the gap height between the base of the plate and the bed, and $H$ is the height of the water in the channel. The wake flow simulations are performed using the finite volume method with the STAR-CCM+ commercial code [9].

In the current simulations, structured cells were used to mesh the computational domain. The mesh is clustered around the bluff body, near the bed and in the wake region to better capture the bed effect and the various flow features. Many grids were considered in the current study, namely, 10, 15, 20 and $22 \times 10^6$ cells. In each case, many parameters were checked and compared with experimental results. Furthermore, successive grids were compared to determine whether or not there was a change in the mean characteristics, wake size and turbulence structures. On this basis, the final computations were performed using $22 \times 10^6$ cells. Uniform cells (2 mm) have been used in the grid everywhere in the computational domain except at the wall locations. The homogeneous distribution of cells is employed to overcome difficulties faced in the earlier stage of the study in identifying the flow structures in the transitional regions. A minimum cell size of 0.05 mm appears adjacent to the wall and the bluff body. Ten layers of fine prism cells packed in a 1.0 mm width with a stretching factor of 1.5
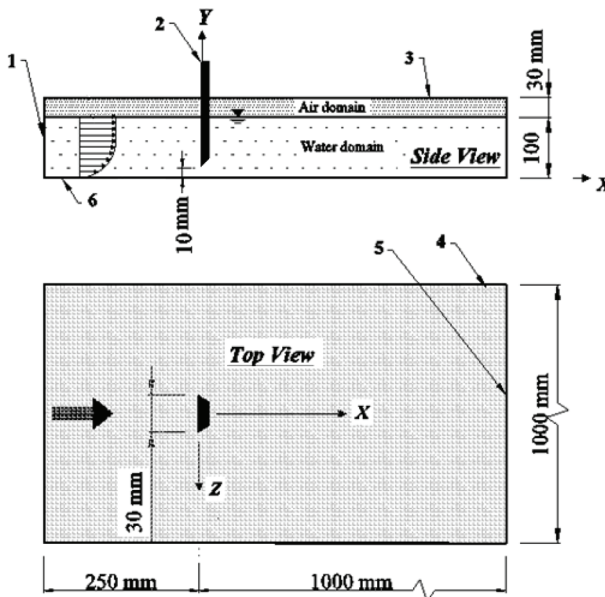


1: Boundary layer velocity profile (inlet); 2: Sharp-edged bluff body; 3 and 4: Channel ceiling and sides (slip walls); 5: Outlet boundary (atm. pressure); 6: Bed (no-slip wall).

Figure 1: Computational model with appropriate boundary conditions.

is employed to resolve the wall effect. First-order implicit time marching and second-order spatial differencing are used in the current study to discretize the governing equations. Customarily, the value of $y+$ ($y+ = 0.4$ in current study) is calculated based on the distance of the centre of the first cell row from the wall.

The volume of fluid (VOF) method suggested by Hirt and Nichols [10] is a free surface modelling technique for tracking the free surface. The VOF model can model two or more immiscible fluids by solving a single set of momentum equations and tracking the volume fraction of each of the fluids throughout the domain. The major complication associated with the VOF method is the smearing of the free surface. This problem originates from extreme diffusion of the transport equation at the interfaces. This issue can be mitigated by using the high-resolution interface capturing (HRIC) scheme [11] to discretize the convective terms in the governing equations. The normalized variable diagram (NVD) [12] is very useful for analysing boundedness properties of convective discretization schemes and provides the methodology used in constructing high-resolution schemes. In high-resolution schemes the local Courant–Friedrichs–Lewy (CFL) condition (CFL $\leq 1.0$) should be satisfied to ensure numerical stability. In the current study, different time steps were tested to satisfy the CFL condition and a final time step was set as $1 \times 10^{-3}$ s. Twenty internal iterations were employed at each time step. The frequency of vortex shedding corresponds to a shedding period $T = 0.51$ s. The time of 60 s is used for data averaging, which yields $t_{av}/T > 100$.

DES [13] is a modification of a RANS model which treats near-wall regions in a RANS-like manner, and it treats the rest of the flow in an LES-like manner. The model was originally formulated by replacing the distance function in the Spalart–Allmaras model with a modified distance function. The $k$-$w$ SST (shear stress transport) turbulence model is a two-equation eddy viscosity model [14–15] and has been selected as the RANS part of the DES turbulence model in this study. The $k$-$w$ SST model solves additional transport equations for turbulent kinetic energy $k$ and specific dissipation rate $w$, from which the turbulent kinematic viscosity ($v_t = k/w$) can be derived. The transport equations of $k$ and $w$ are described in [16].

Validations are carried out with a no-gap case by comparing the numerical results from the simulations, i.e. mean and statistical features, with available data from previous PIV experiments reported in [6–7]. Figures 2 and 3 show selected samples of the validation process; here $U$, $W$ and $U_s$ represent the streamwise, transverse and the upstream approaching velocity at the given horizontal location from the bed, respectively. The comparisons between the experimental and computational results for the normalized mean quantities and for other statistical quantities (not shown here) reveal that the current model can produce results with adequate accuracy at different elevations from the bed. The model predicts the experimental data with less than 12% maximum difference occurring in the horizontal plane $y/H = 0.1$.

## 3  RESULTS AND DISCUSSION

Nasif *et al*. [18–20] numerically investigated the three-dimensional fluid structures in the shallow wake flow in the absence of the gap using the $\lambda_2$-criterion. In the previous studies, the interactions between the fluid structures, bed, free surface and the bluff body in the mean and transient flow are analysed and addressed. At this point, to understand the effect of the gap flow on the turbulent structures and therefore on the free surface, it is worthwhile to briefly review the turbulent structures that are present in the mean flow from previous investigations for the case with no gap.

Figure 4 shows the three-dimensional fluid structures shaded by the normalized streamwise vorticity ($\omega_x D/U_\infty$) for the case of no gap, where $\omega_x$ and $U_\infty$ represent the streamwise vorticity and the free-stream velocity, respectively. In this figure, fluid structures are extracted
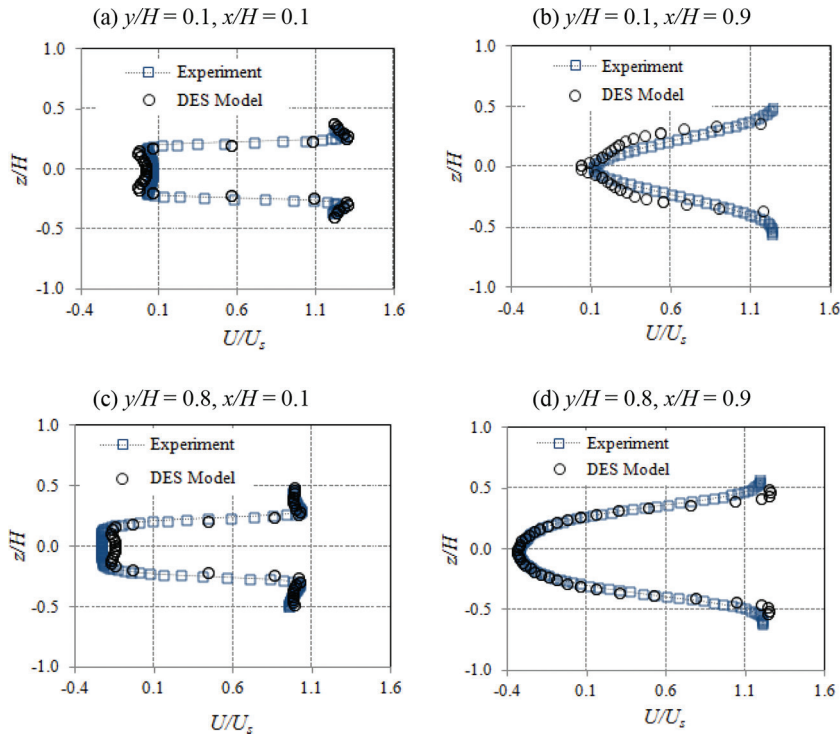
Figure 2: Computational and experimental [6–7] normalized mean streamwise velocity profiles at four different locations in the wake flow [17].
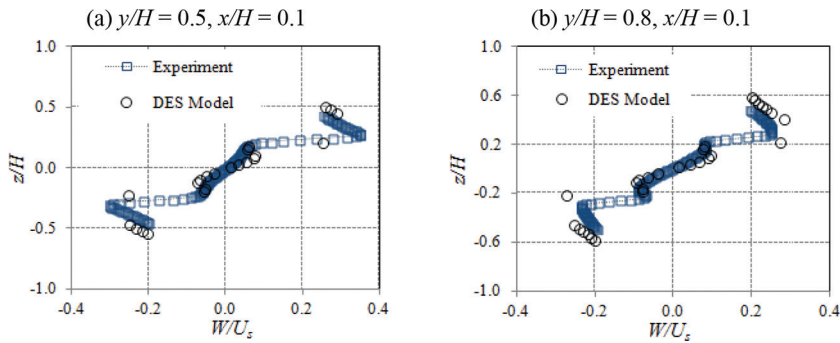


Figure 3: Computational and experimental [6–7] normalized mean transverse velocity profiles at two different locations in the wake flow [17].

using $\lambda_2 = -1.0$. This scalar value is chosen based on the fact that it reveals the well-defined patterns in the wake flow. As shown in Figs. 4b and c, the structures are clipped at two different elevations from the bed for better illustration of the fluid structures details. The horseshoe vortex structure is obvious in Fig. 4. It stretches downstream from the front of the bluff body and contributes to the three-dimensional characteristics in the wake flow. A collar vortex, embedded in a region of high vorticity in the near-bed location, emanates from the edges of

(a) Structures zone: 0.0<$y/H$<1.0



(b) Structures zone: 0.0<$y/H$<0.8



(c) Structures zone: 0.0<$y/H$<0.25



Figure 4: $\lambda_2$ isosurface ($\lambda_2 = -1.0$) for the mean flow coloured by streamwise vorticity vector component for the no-gap case.

the body. The sense of rotation of the collar vortex is similar to that of the horseshoe vortex [18]. At downstream locations ($x/H > 2.0$), two bed-parallel counter-rotating tubes (see Fig. 4c) are generated inwards next to the legs of the horseshoe vortex. These tubes reside near the bed and have the same sense of rotation as the horseshoe legs. The mechanism of formation and development of these tube structures in the mean flow is elaborated in [18–19]. The surface-normal tubes shown in Fig. 4b immediately after the bluff body represent the

averaging of the structures that shed from the sides of the bluff body in the transient flow. These structures absorb the required energy from the outer accelerating flow to overcome the wall shear stress and maintain its existence in the near-wake location. As one moves farther downstream, the accelerating flow region turns to a decelerating flow region and the kinetic energy that feeds the wake region is not sufficient to overcome the wall shear stress. Consequently, the interaction between the surface-normal tubes and the bed weakens as the kinetic energy of the accelerating flow is depleted downstream. This is the location where these structures start to detach from the bed and align with the mean flow, forming the mid-depth tubes as shown in Fig. 4b. One of the important signatures of shallow-wake flows is the existence of the surface-parallel tubes as shown in Fig. 4a. These structures are buried inside the surface layer [21] and act to transport the fluid particles from the wake core to the outer region. These structures are generated immediately underneath the free surface due to the impingement of moving fluid particles through the wake central plane with the free surface. Other minor structures, i.e. frontal structures and air–water interfacial structures were also captured at the water–air interface as shown in Fig. 4a.

Contrary to the no-gap case that is shown in Fig. 4, only traces of the horseshoe structure are sustained as the gap is introduced in the wake flow as shown in Fig. 5. The major portion of the horseshoe vortex appears to be shrunk and attenuated. This can be attributed to two different effects: on the one hand, the presence of the gap reduces the combined interaction between the approach flow, the bluff body and the bed, and therefore weakens the horseshoe structure. On the other hand, the gap flow enhances the lateral entrainment as will be explained later and acts to disintegrate and thus prevent the formation of the horseshoe structure. The effect of the gap flow is also apparent on the other turbulent structures in the wake flow as shown in Fig. 5. These structures become irregular and asymmetrical about the centre plane of the wake.

Another observation that can be drawn from Fig. 5 is that the recirculation region, immediately behind the bluff body, becomes smaller compared to the case of no gap. This is because the gap flow will sustain this region with additional kinetic energy and consequently increases the momentum and reduces the volume of this region. A new structure can also be identified in Fig. 5c, which appears near the bed, immediately after the recirculation region at the centre of the wake (blue structure). This three-dimensional structure, which is absent in the case of no gap, is stretched upwards to the vertical location $y/H = 0.2$. The presence of this structure in the wake flow will enhance the wall normal velocity and accelerate the restoration of the free surface to its original level at the shorter downstream distance from the bluff body as will be investigated shortly.

Figure 6 shows the normalized wall-normal velocity ($V/U_\infty$) for the two cases that are used in the current study. In this figure, the data are extracted at the centre plane of the wake. The approaching free-stream velocity, $U_\infty$, was used as the velocity scale for normalizing the mean velocity. The thick dotted line, marked as "free surface" at location $y/H \approx 1.0$, represents the air–water interface. A distinguishing feature of the shallow wakes is the three-dimensional roll-up structure [18–19, 22] between the bed and the free surface that has been observed immediately behind the bluff at the wake centre plane in Fig. 6a. This horizontally oriented structure, which is a three-dimensional spiral structure and has a positive rotation sense, plays a role to bridge both parts of the surface-normal tube (shown in Fig. 4b) and acts to transport the fluid particles from the wake core to the outer surroundings [20]. This structure does not considerably enhance the wall-normal velocity and therefore the free surface restores its original shape at a downstream location of $x/H = 2.2$ from the bluff body as shown in Fig. 6a.

(a) Structures zone: 0.0<*y/H*<1.0



(b) Structures zone: 0.0<*y/H*<0.8



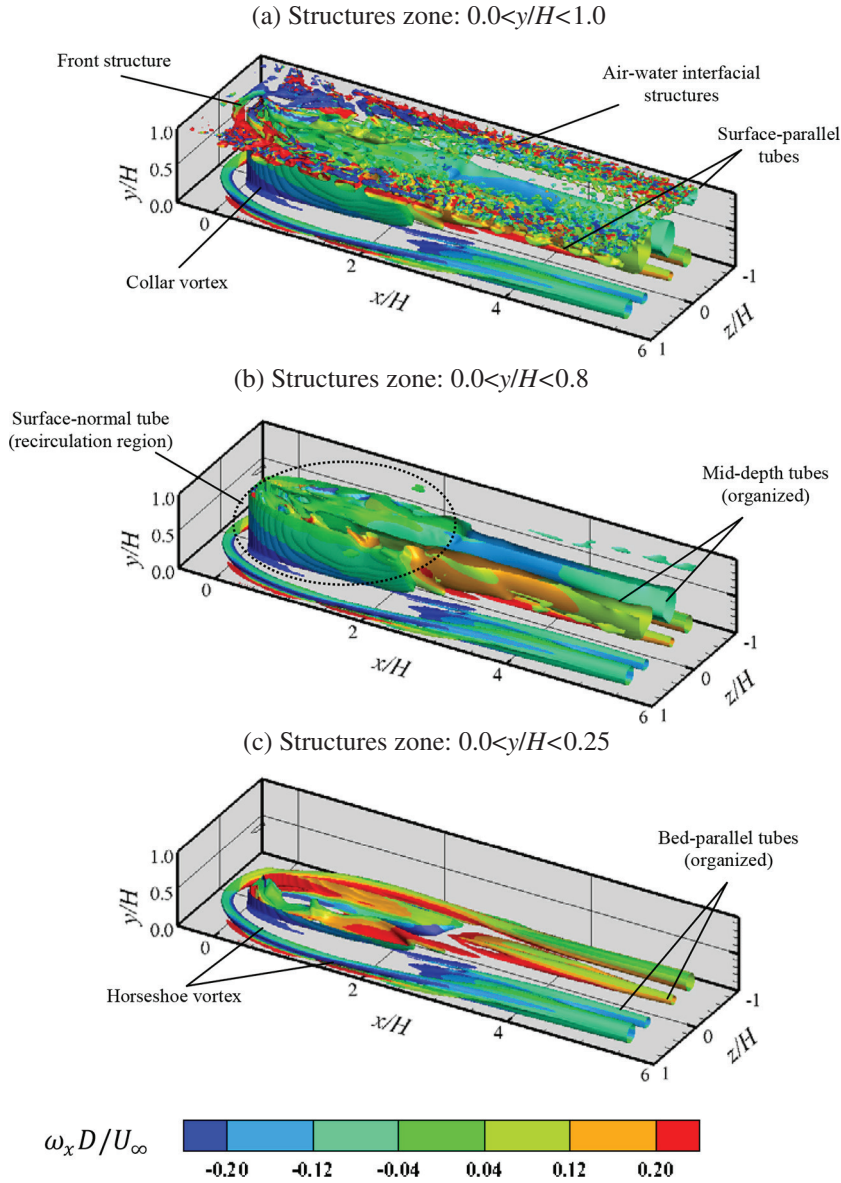(c) Structures zone: 0.0<*y/H*<0.25



$\omega_x D/U_\infty$
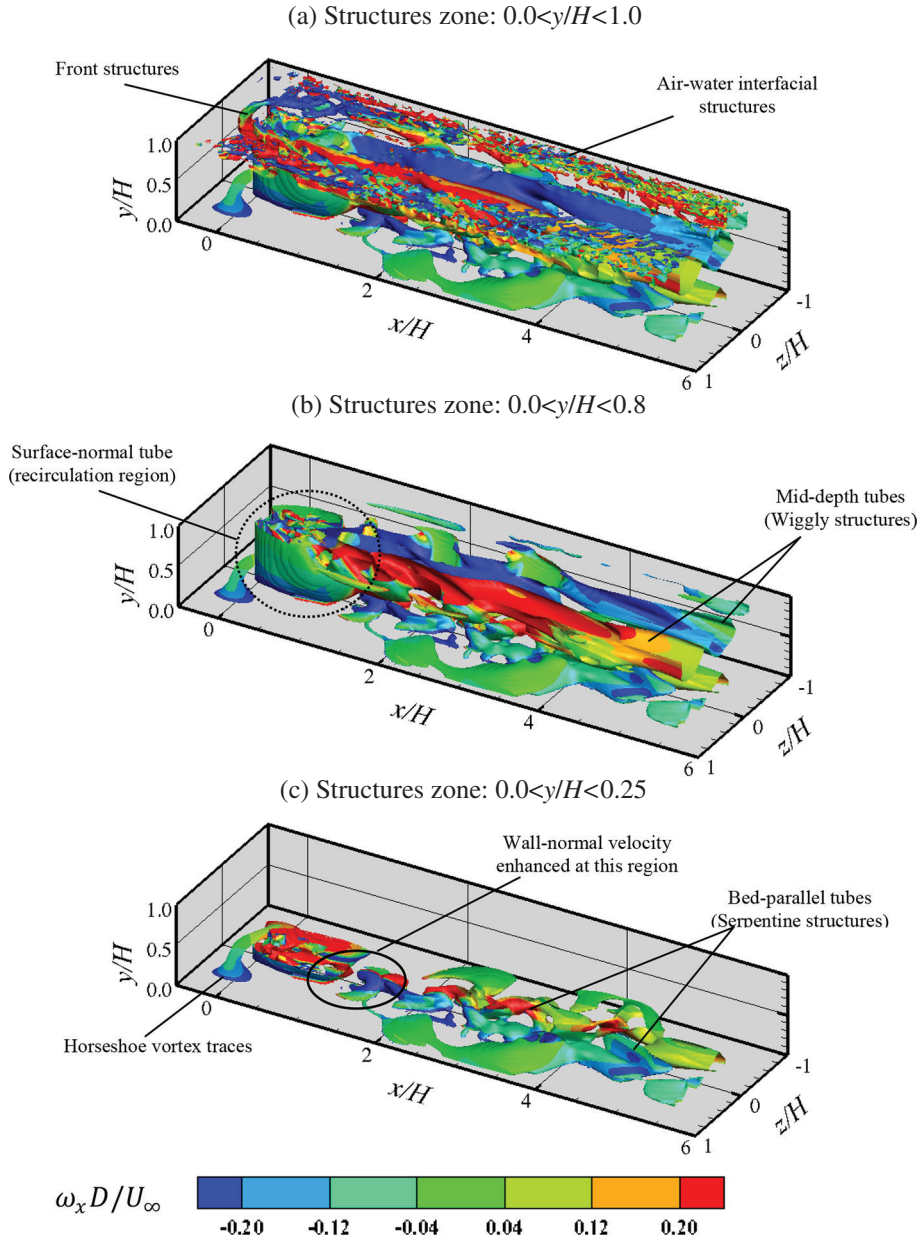


Figure 5: $\lambda_2$ isosurface ($\lambda_2 = -1.0$) for the mean flow coloured by streamwise vorticity vector component for the gap size $h/H = 0$.

As the gap flow is introduced in the wake, the wall jet turns upward at a downstream distance of about $x/H = 1.0$ due to the weak hydraulic jump (details are not shown here), pushing the three-dimensional roll-up structure towards the bluff body and raising it away from the bed by a dista nce equivalent to the gap height. A new structure, which has a counter rotation sense to the three-dimensional roll-up structure, will be generated near the bed at downstream

Figure 6: Vector plot of the mean velocity field superimposed by contours of the normalized vertical velocity ($V/U_\infty$) in the vertical plane $z/H = 0.0$.

location $x/H = 1.35$ as shown in Fig. 6b. This structure appears as a three-dimensional blue hump in Fig. 5c. The mechanism of formation of this structure is attributed to the high momentum that is associated with the wall jet, which penetrates and overcomes the reverse flow region with negative stream velocity. The strong interaction between the counter-rotating structures near the bed for the case with the gap will enhance the wall-normal velocity as shown in Fig. 6b (red contour). The wall-normal velocity enhancement occurs in the region marked in Fig. 5c. The enhancement of the wall-normal velocity in the presence of the gap explains the restoration of the free surface at shorter distances downstream of the bluff body. The free surface restores its original position at $x/H = 1.4$ in the latter case as shown in Fig. 6b.

Figure 7 shows the contours of the normalized mean lateral velocity ($W/U_\infty$) extracted at downstream locations of $x/H = 0.5$ and 1.35, respectively, for the two cases that have been investigated in the current study. The downstream distance $x/H = 1.35$ has been chosen at the same location of the new structure that enhances the wall-normal velocity in the case of the gap. It is obvious from Figs. 7a and b that the concavity in the free surface in the lateral direction is comparable for either case at the downstream location $x/H = 0.5$. This indicates that the gap flow has no influence on the free surface at a short distance from the bluff body. However, the effect of the gap flow is apparent on the free surface at downstream location $x/H = 1.35$ as shown in Figs. 7c and d. The depression in the free surface spans in the lateral direction between $-1.2 < z/H < 1.2$ as shown in Fig. 7c, while the free surface approximately restored its origin position at $y/H = 1.0$ for the case with the gap as illustrated in Fig. 7d.

In light of the above discussion (see Figs. 5–7), one can conclude that the free surface starts to restore its original shape at approximately a downstream location $x/H = 1.0$, a location of the interaction between the new structure that is generated due to the gap flow and three-dimensional roll-up structure as shown in Fig. 6b. Another conclusion which can be drawn from Fig. 7 is that
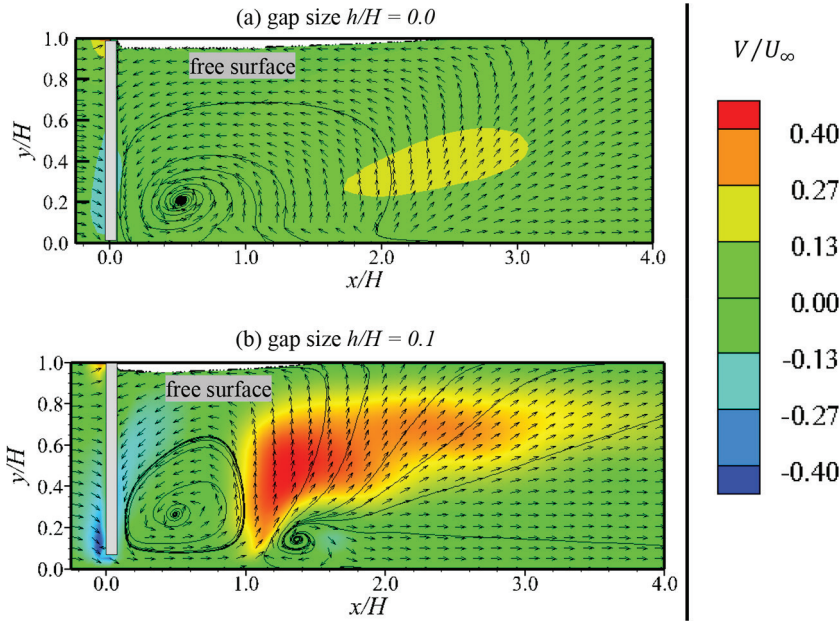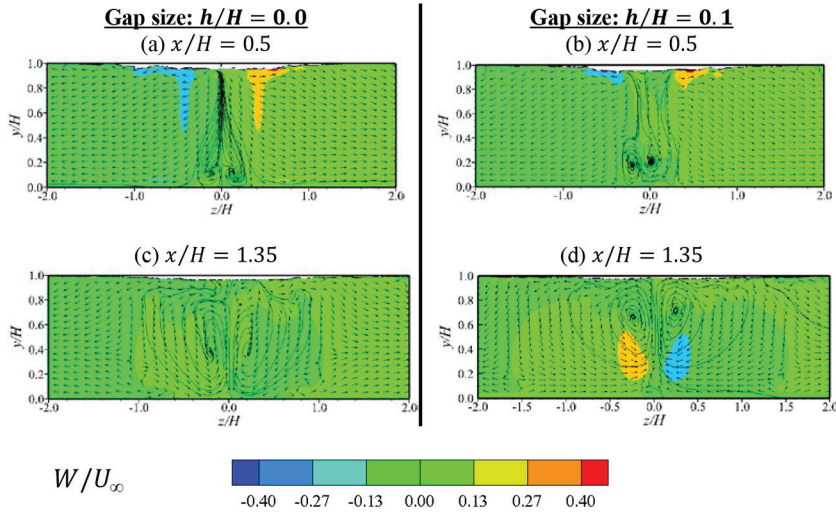
Figure 7: Vector plot of the mean velocity field superimposed by contours
of the normalized transverse velocity ($W/U_\infty$) in the vertical plane.

the gap flow enhances the entrainment at downstream location $x/H = 1.35$, i.e. beyond the locations where the enhancement of the wall-normal velocity occurs, as shown in Fig. 7d. The wall-normal velocity will increase the inward transverse flow since it entrains more fluid into the wake region at these regions. This observation agrees with the experimental investigations that were performed by Shinneeb and Balachandar [6]. The gap flow has a slight effect on the lateral entrainment at the vertical plane $x/H = 0.5$ as shown in Fig. 7b. However, the wall jet will affect and scramble the topological feature of the two spiral structures (two foci) on the sides of the wake centre plane and lifts them a bit from the bed in the near-wake region. The enhancement in the wall-normal velocity and the lateral velocity for the case of the gap will also affect the topological feature of the structures in the far-wake region (details are not shown here). The degree of randomness of the structures increases as one moves further downstream.

## 4  CONCLUSION

The present study is oriented towards an investigation of the influence of the gap in a wake on the flow characteristics, fluid structures and the free surface restoration. The numerical study was carried out using the finite volume technique. The fluid structures were identified using the $\lambda_2$-criterion which successfully distinguishes the rotational contribution of the vorticity distribution. The following results are concluded from the current study:

- A new structure at the near-bed location is generated when the gap is introduced in the wake flow. The interaction between this structure and the adjacent structures will enhance the wall-normal component velocity and restore the free surface to its original shape at a shorter downstream location in the presence of the gap case.
- One of the consequences of the gap is to reduce the size of the wake. The gap flow will sustain this region with additional kinetic energy and consequently reduces the wake size.
- The lateral entrainment from the surroundings to the wake region increases as the gap is introduced in the wake flow. This can be attributed to the increase of the magnitude of the positive wall-normal velocity component which is enhanced by the gap flow.

- As the gap is introduced in the wake flow, the fluid structures become irregular and asymmetrical about the centre plane of the wake. The degree of randomness increases in the far-wake region.
- The major portion of the horseshoe vortex appears to be intermittent and attenuated as the gap is introduced in the wake.

REFERENCES

[1]  Dey, S., Lodh, R. & Sarkar, S., Turbulence characteristics in wall-wake flows downstream of wall-mounted and near-wall horizontal cylinders. *Environmental Fluid Mechanics*, **18(4)**, pp. 1–31, 2018.

[2]  Panigrahi, P.K., PIV investigation of flow behind surface mounted detached square cylinder. *Journal of Fluids Engineering*, **131(1)**, 011202, 2009.

[3]  Wang, X.K. & Tan, S.K., Experimental investigation of the interaction between a plane wall jet and a parallel offset jet. *Experiments in Fluids*, **42(4),** pp. 551–562, 2007.

[4]  Martinuzzi, R.J., Bailey, S.C.C. & Kopp, G.A., Influence of wall proximity on vortex shedding from a square cylinder. *Experiments in Fluids*, **34(5)**, pp. 585–596, 2003.

[5]  Taniguchi, S. & Miyakoshi, K., Fluctuating fluid forces acting on a circular cylinder and interference with a plane wall. *Experiments in Fluids*, **9(4)**, pp. 197–204, 1990.

[6]  Shinneeb, A.M. & Balachandar, R., Effect of gap flow on the shallow wake of a sharp-edged bluff body–mean velocity fields. *Journal of Turbulence*, **17(1)**, pp. 94–121, 2016.

[7]  Shinneeb, A.M. & Balachandar, R., Effect of gap flow on the shallow wake of a sharp-edged bluff body–turbulence parameters. *Journal of Turbulence*, **17(1)**, pp. 122–155, 2016.

[8]  Shinneeb, A.M., Balachandar, R. & Zouhri, K., Effect of gap flow on the shallow wake of a sharp-edged bluff body—Coherent structures. *Physics of Fluids*, **30(6)**, 065107, 2018.

[9]  CD-adapco, STAR-CCM+ V10.06.009, *User Manual*, 2015.

[10]  Hirt, C.W. & Nichols, B.D., Volume of fluid (VOF) method for the dynamics of free boundaries. *Journal of Computational Physics*, **39(1)**, pp. 201–225, 1981.

[11]  Muzaferija, S., A two-fluid Navier-Stokes solver to simulate water entry. In *Proceedings of 22nd Symposium on Naval Architecture,* pp. 638–651, 1999.

[12]  Leonard, B.P., The ULTIMATE conservative difference scheme applied to unsteady one-dimensional advection. *Computer Methods in Applied Mechanics and Engineering*, **88(1)**, pp. 17–74, 1991.

[13]  Spalart, P.R., Comments on the feasibility of LES for wings, and on a hybrid RANS/LES approach. In *Proceedings of First AFOSR International Conference on DNS/LES*, 1997.

[14]  Wilcox, D.C., Simulation of transition with a two-equation turbulence model. *AIAA Journal*, **32(2)**, pp. 247–255, 1994.

[15]  Wilcox, D.C., *Turbulence Modeling for CFD*. La Canada, CA: DCW Industries, Vol. 2, pp. 103–217, 1998.

[16]  Hoffmann, K. & Chiang, S., *Computational Fluid Dynamics*, Vol. 3, 4th ed., Engineering Education System, Wichita, KS, USA, 2000.

[17]  Nasif, G., Balachandar, R. & Barron, R.M., Influence of bed proximity on the three-dimensional characteristics of the wake of a sharp-edged bluff body. *Physics of Fluids,* **31(2)**, p. 025116, 2019.

[18]  Nasif, G., Barron, R.M. & Balachandar, R., DES evaluation of near-wake characteristics in a shallow flow. *Journal of Fluids and Structures*, **45**, pp. 153–163, 2014.

[19] Nasif, G., Balachandar, R. & Barron, R.M., Characteristics of flow structures in the wake of a bed-mounted bluff body in shallow open channels. *Journal of Fluids Engineering*, **137(10)**, 101207, 2015.

[20] Nasif, G., Balachandar, R. & Barron, R.M., Mean characteristics of fluid structures in shallow-wake flows. *International Journal of Multiphase Flow*, **82**, pp. 74–85, 2016.

[21] Maheo, P., *Free Surface Turbulent Shear Flow*, PhD dissertation, California Institute of Technology, CA, USA, 1999.

[22] Akilli, H. & Rockwell, D., Vortex formation from a cylinder in shallow water. *Physics of Fluids*, **14(9)**, pp. 2957–2967, 2002.

*This page intentionally left blank*

# CPFD MODEL FOR PREDICTION OF FLOW BEHAVIOR IN AN AGGLOMERATED FLUIDIZED BED GASIFIER

NORA C. I. S. FURUVIK, RAJAN JAISWAL, RAJAN K. THAPA & BRITT M. E. MOLDESTAD
Department of Process, Energy and Environmental Technology, Faculty of Technology, Natural Science and
Maritime Science, University of South-Eastern Norway, Norway.

## ABSTRACT
Renewable energy sources have significant potential for limiting climate change and reducing green-house gas emissions due to the increased global energy demand. Fluidized bed gasification of biomass is a substantial contribution to meeting the global energy demand in a sustainable way. However, ash-related problems are the biggest challenge in fluidized bed gasification of biomass. Bed agglomeration is a result of interaction between the bed material and alkali metals present in the biomass ash. The agglomerates interfere with the fluidization process and might result in total de-fluidization of the bed. The study focuses on ash challenges related to the fluidization behavior in gasification of biomass. A model is developed and verified against results from previous performed experiments in a cold flow model of a bubbling fluidized bed. The commercial computational particle fluid dynamics (CPFD) software Barracuda Virtual Reactor is used for the computational study. The simulations show that the CPFD model can predict the fluidization process of an agglomerated fluidized bed gasifier.
*Keywords: agglomeration, Barracuda VR, bubbling fluidized bed, CPFD simulation, flow behavior.*

## 1 INTRODUCTION
Global warming is perhaps the most pressing environmental challenge in our time, and there is an urgent need to promote the use of renewable energy sources in order to ensure a sustainable future. The massive expansion in the use of fossil fuels and the rising fears over the effects of the increased $CO_2$ emissions have forced the countries to search for climate-friendly alternatives to fossil fuels [1]. Biomass-based energy is presently the largest contributor of renewable energy, and according to World Bioenergy Association, biomass annually accounts for 10.3% of the global energy supply [2]. The leading energy conversion technology for utilization of biomass fuels is fluidized bed gasification, which converts biomass into a gaseous mixture in the presence of heat and a gasifying medium [3].

Fluidized beds are noted for their high heat transfer, uniform heating and high productivity. Despite being a promising technology for sustainable heat and power generation, biomass gasification has operational problems that can restrict its commercialization [1]. Interactions between the bed material and the molten ash components cause formation of agglomerates, resulting in the ash components adhering to each other to form larger entities [4]. Bed agglomeration is the main obstacle for successful applications of biomass gasification [5]. Presence of agglomerates in the bed alters the flow behavior in the gasifier, causing changes in the fluidization properties and consequently loss of control of important operating parameters such as pressure drop, minimum fluidization velocity and bubble behavior. In the most severe cases, bed agglomeration can lead to total de-fluidization of the bed [6].

Due to the operational problems caused by bed agglomeration, extensive studies have been performed to gain more insight into the ash-related issues in biomass gasification. These research activities have provided important knowledge about ash from biomass, and the relation between ash composition and the ash melting temperatures. However, only few data are available on the ash melting and agglomeration, and its relation to the fluidization behavior

in a biomass gasification reactor. Understanding the phenomenon of agglomeration is crucial to optimizing the design and the operation conditions of a bubbling fluidized bed gasification reactor. The objective of this work is to develop a computational particle fluid dynamics (CPFD) model that describes how the agglomerates affect the fluidization process in a bubbling fluidized bed reactor.

The model is based on theoretical and experimental studies. The commercial CPFD software package, Barracuda Virtual Reactor (VR) 17.1.0 is used for the computational study. The CPFD model is validated against previous performed experimental results carried out in a cold flow model of a bubbling fluidized bed [7].

## 2  BED AGGLOMERATION

Ash melting and subsequently formation of agglomerates is one of the major challenges in fluidized bed gasification of biomass [4]. Bed agglomeration occurs due to chemical reactions and physical collisions between the bed material and biomass ash with high content of alkali species. The phenomenon is illustrated in Fig. 1, which is based on [8]. Bed agglomeration happens as the inorganic alkali ash components interact with the bed material to form a sticky layer on the surface of the bed materials. As the ash particles and the bed material continue to collide, the ash coating grows thicker. Eventually, the bed particles grow towards larger agglomerates that will interfere with the fluidization process [4].

The main problem with ash melting and agglomeration in fluidized beds is the issue of de-fluidization. The agglomerated ash-particles (Fig. 2) differ considerably from the bed particles in shapes, sizes and densities, and are therefore difficult to fluidize adequately. At the time of de-fluidization, a sudden decrease in the pressure drop over the bed is observed as the sticky and cohesive agglomerated ash particles form small volumes in the bed. These volumes are not fully fluidized, leading to improper circulation of the biomass and thereby non-uniform temperature distribution and decreased heat transfer in the bed. Inside the de-fluidized volumes, the temperatures will be increased, which in turn increases the stickiness of the particle surfaces resulting in enhanced agglomeration [7].

The poor mixing and the decreased heat transfer that occur due to bed agglomeration change the bubble behavior in the bed. While normal fluidization conditions give well-distributed bubble frequency through all sections along the bed, the fluidization in the agglomerated bed is characterized by instabilities with frequent bubbling and channeling of fluid. Eventually, the bed takes a sluggish appearance. The unwanted collapse of the fluidized bed is rarely recognized until sudden de-fluidization occurs, and might lead to shutdown of the whole installation [4]. Figure 3 illustrates the bubble behavior in a normal fluidized bed compared to the bubble behavior in an agglomerated fluidized bed.
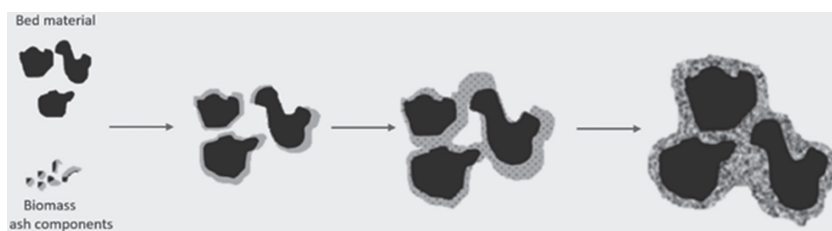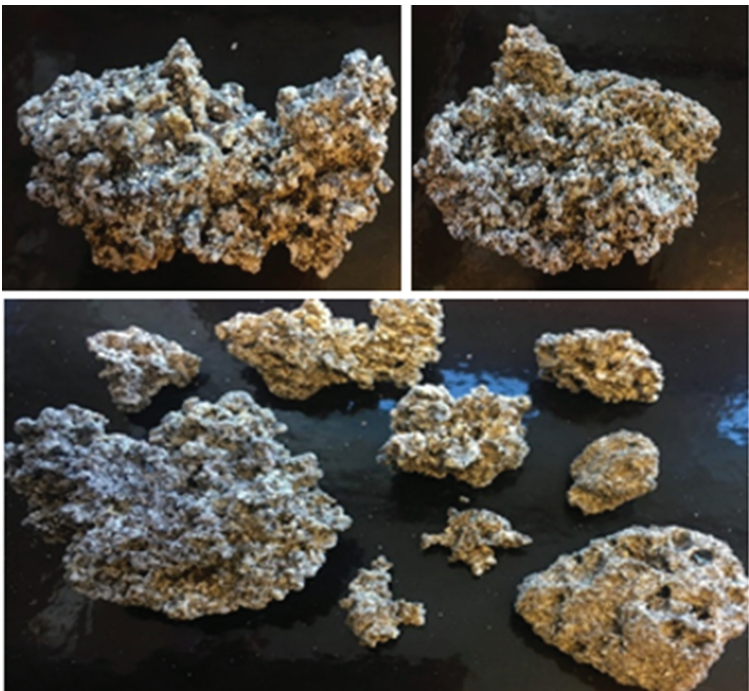


Figure 1: Formation of agglomerates.

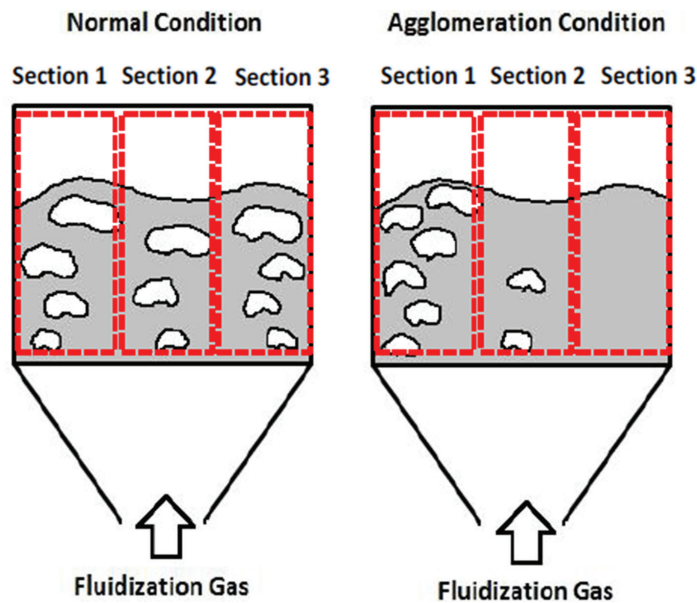Figure 2: Agglomeration of silica sand particles.



Figure 3: Bubble frequency in a fluidized bed [9].

## 3 MODEL DEVELOPMENT

### 3.1 Model description

The CPFD software package Barracuda VR 17.1.0 was used to simulate the flow characteristics in an agglomerated bubbling fluidized bed. Barracuda VR uses the Multiphase Particle In-Cell (MP-PIC) approach that is based on the Eulerian–Lagrangian approach, where the transport equations are solved for the continuous fluid phase and each of the discrete particles are tracked through the calculated fluid field. The fluid–particle interaction is considered as source terms in the transfer of mass, momentum and energy between the two systems. CPFD simulations are hybrid numerical methods where the Eulerian approach is used for solving the fluid phase, and the Lagrangian computational particle approaches for the modeling of the particle phase [10]. Chladek *et al*. [11] and Jayarathna *et al*. [12] describe the transport equations in detail.

The Barracuda software package includes several drag models. In order to find the most suitable model for the simulations of flow characteristics in an agglomerated fluidized bed gasifier, different drag models were tested. The best fit between the numerical model (simulation) and the experimental results was achieved with the Wen–Yu drag model. Wen–Yu drag model is based on a variety of experiments performed by Richardson and Zaki [13]. The correlation developed from the experimental data achieved by Richardson and Zaki [13] is valid when the internal forces are negligible, meaning that the viscous drag forces dominate the flow behaviour.

In general, the drag force caused by the fluid on the particles is calculated from:

$$F_p = m_p \cdot D \cdot \left( u_f - u_p \right) \tag{1}$$

where $m_p$ is the particle mass, $D$ the drag function, $u_f$ the superficial velocity of the fluid and $u_p$ the superficial velocity of the particles. The Wen–Yu drag function is dependent on the fluid and the particle properties and is expressed by the drag coefficient ($C_d$):

$$D = \frac{3}{8} \cdot C_d \cdot \frac{\rho_f \cdot \left( u_f - u_p \right)}{\rho_p \cdot r_p} \tag{2}$$

where $\rho_f$ and $\rho_p$ is the density of the fluid and the particle, respectively, and $r_p$ the particle radius. $C_d$ is a function of Reynolds number *(Re)* and the fluid volume fraction ($\theta_f$), and is determined according to a set of conditions shown in eqn (3).

$$C_d = \begin{cases} \dfrac{24}{Re} \cdot \theta_f^{n_0} \ 0.5 < Re \\ \quad . \\ \dfrac{24}{Re} \cdot \theta_f^{n_0} \cdot \left( c_0 + c_1 \cdot Re^{n_1} \right) 0.5 \le Re \le 1000 \\ \quad . \\ c_2 \cdot \theta_f^{n_0} \ Re > 1000 \end{cases} . \tag{3}$$

Reynolds number is determined by

$$Re = \frac{2 \cdot \rho_f \cdot r_p \cdot \left(u_f - u_p\right)}{\mu_f} \tag{4}$$

where $\mu_f$ is the viscosity of the fluid. More detailed information of the Wen–Yu drag model are presented by Wen and Yu [14].

### 3.2  Computational setup

The cold flow model of the fluidized bed used in the experimental study is shown in Fig. 4.

A three-dimensional Cartesian coordinate system was used to describe the cylindrical column with a height of 140 cm and a diameter of 8.4 cm. In the present study, the static bed height was 21 cm. The computational grid is shown in Fig. 5. The mesh size was 0.01 m x 0.01 m x 0.01 m and the number of control volumes was 13,284. Isothermal temperature at 300 K was used, and the fluidizing gas was air at atmospheric pressure that was flowing through the gas distributor from the bottom of the column. The total pressure was monitored at positions 3.5 cm (P1) and 13.5 cm (P2) above the distributor. The simulation was run for 50 s with a time step of 0.001 s. The simulation parameters are summarized in Table 1. The Wen–Yu drag model was selected, and the coefficient values $c_0$, $c_1$, $c_2$, $n_0$ and $n_1$ were equal to 1.0, 0.15, 0.44, −2.65 and 0.687, respectively.

Quartz sand with a Solid density of 2,650 kg/m$^3$ was used as bed material. The particle size of the sand ranged from 150 μm to 340 μm with a mean diameter of 175 μm. The particle size distribution was determined by sieving analysis. The maximum close pack volume fraction was set to 0.54, which was calculated based on the ratio of the bulk density and the particle density. The maximum momentum from the redirection of particles collision was
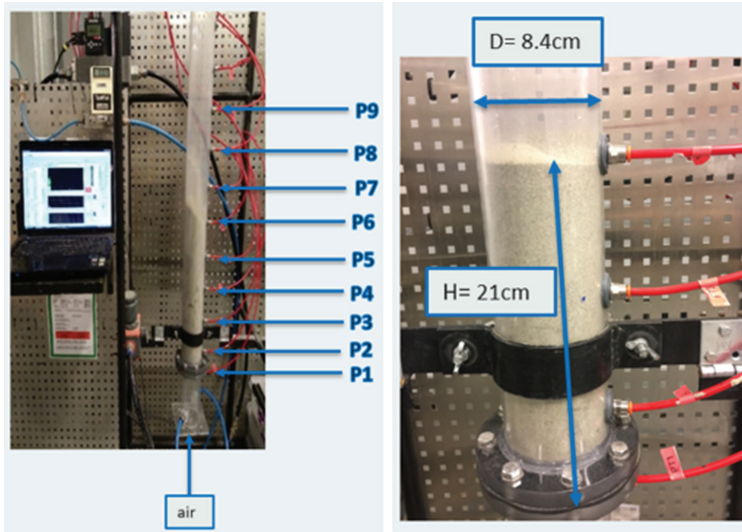


Figure 4: Cold flow model of bubbling fluidized bed.
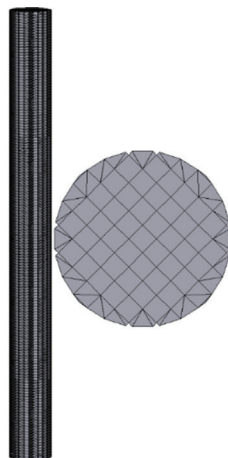
Figure 5: Computational grid.

Table 1: Simulation parameters.

| Parameter | Value |
|---|---|
| Number of grid cells | 13,284 |
| Static bed height | 21 cm |
| Fluidizing agent | Air |
| Type of flow | Isothermal @ 300 k |
| Superficial gas velocity | 0.02: 0.005: 0.15 m/s |
| Simulation time for each flowrate | 50 s |
| Drag model | Wen–Yu |
| Drag coefficients ($c_0$, $c_1$, $c_2$, $n_0$, $n_1$) | Default values |

assumed to be 40%, the normal-to-wall and tangential-to-wall momentum retention were 0.3 and 0.99, respectively. The particle properties are listed in Table 2.

The flow behavior in an agglomerated fluidized bed was studied by comparing three different CPFD simulations, where agglomerates were present in the bed. The different cases were defined with 5%, 10% and 15% of agglomerates. In order to simulate agglomerates, a coarser

Table 2: Particle properties.

| Particle | Property | | | |
|---|---|---|---|---|
| | Mean diameter (μm) | Density (kg/m$^3$) | Sphericity | Close pack volume fraction |
| Bed material | 175 | 2,650 | 0.86 | 0.54 |
| Agglomerates | N/A | 1,506 | 0.6 | N/A |

grid was used and the number of grid cells was reduced from 13,284 to 5,782. The size of the agglomerates was limited by the chosen grid, which allowed a maximum particle size of 1.0 cm. The agglomerates ranged from 0.5 cm to 1.0 cm in diameter, with density equal to 1,506 kg/m$^3$. The density of the agglomerates was determined based on mass and volume [7].

## 4  RESULTS AND DISCUSSION

The Wen–Yu drag model was used in the CPFD simulations. The model was validated by customizing it to the previous performed experimental results for sand particles with a mean diameter of 175 μm [7]. The pressure drop in the bed was plotted as a function of the superficial air velocity. As the superficial velocity is steadily increased, the bed expands slightly. The drag caused by the fluid on the particles increases and at some point, the particles begin to move. At a certain velocity, the particles will be suspended by the upward-flowing fluid [15]. This state is referred to as the minimum fluidization and the corresponding superficial velocity is the minimum fluidization velocity ($u_{mf}$). Figure 6 compares the simulation with the experimental result. The simulated minimum fluidization velocity was 0.039 m/s, which is slightly higher than the experimental value of 0.035 m/s.

The deviation between the simulation and the experiment can be related to how the characteristics of the particles influence on the fluidization processes, and how the numerical model accounts for the particle size distribution. Barracuda uses the MP-PIC-based Euler–Lagrangian approach, which means that instead of tracking each individual particle in the bed separately, particles with the same properties are grouped into parcels. Each parcel is represented by one computational particle, in which the equation for motion is solved as the discrete particle moves through the flow field [16]. Another explanation for the deviation might be erroneous assumptions for the drag model coefficients, $c_0$, $c_1$, $n_0$ and $n_1$. The value of $c_2$ will not influence on the results as it only has significance when $Re > 1,000$. Which is not the case for the present work. In order to find the model that shows the best agreement with the experimental results, several simulations with different values for the coefficients were performed. Finally, the default values provided in Barracuda were chosen for all the coefficients. In Fig. 6, it is seen that the simulation has a significant peak in the pressure drop at the onset of fluidization. However, the pressure drop decreases quickly after fluidization and stabilizes at approximately the same value as in the experiment, corresponding to the weight of the particles [11].
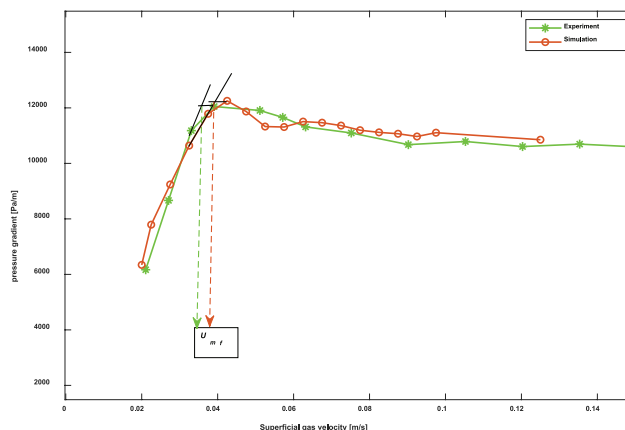


Figure 6: Pressure drop as a function of increasing superficial air velocity.

The result shows that the validated CPFD model describes the fluidization of the sand particles with good agreement, and the model was used to simulate the fluidization conditions in an agglomerated fluidized bed. Figure 7 shows how bed agglomeration changes the fluidization characteristics of the bed. Smooth fluidization is a result of hydrodynamic, gravitational and inter-particle forces. When agglomerates are present in the bed, the inter-particle forces take control over the bed behavior, and the agglomerates will interfere with the fluidization process. As the sticky particles grow into larger entities, the particles lose their original weight and are no longer able to be fluidized by the initial gas velocity. Under fluidized conditions, the pressure drop through the bed is equal to the total hydrostatic pressure of the bed, but due to channeling and agglomerated zones, agglomerated fluidized beds are characterized by lower pressure drop than normal fluidized beds.

The decreased pressure drop in the agglomerated fluidized beds indicates that the beds are not completely fluidized, as the bubbles collapse at the bottom of the bed instead of passing through the entire bed. Figure 8 illustrates the distribution of the particle species in the agglomerated fluidized bed, initially (Fig. 8a) and after fluidization (Fig. 8b). Blue color indicates bed



Figure 7: Simulation of fluidization in normal and agglomerated fluidized bed.



Figure 8: (a) Initial particle species and (b) particle species after fluidization.

particles, while red color indicates agglomerates. The bed material are in motion at the top of the bed, while the agglomerates remain at the bottom and one side of the column resulting in the gas flowing in channels. In biomass gasification, agglomeration causes improper circulation of the biomass and non-uniform temperature distribution in the bed. The non-uniform temperature distribution forms zones wit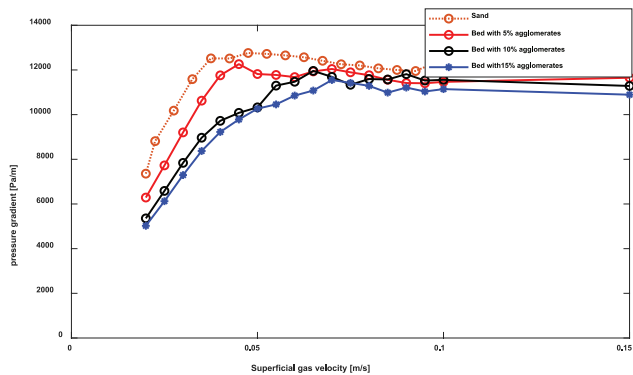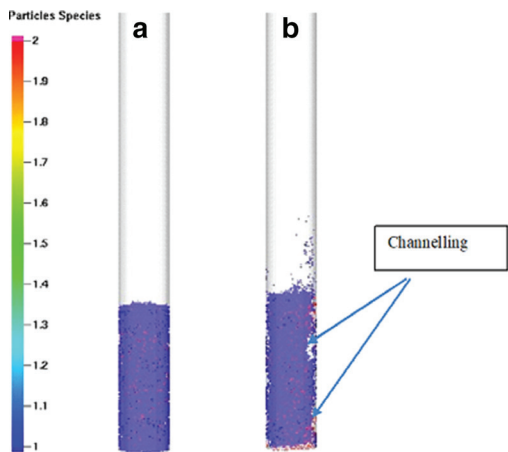h de-fluidized volumes and increased temperatures. Higher temperatures increase the stickiness of the particle surfaces and might result in enhanced formation of agglomerates. Eventually, the bed takes a sluggish appearance.

## 5 CONCLUSION

The objective of this study was to develop a CPFD model for simulation of the flow behavior in an agglomerated fluidized bed gasifier. The simulations were performed using the commercial CPFD software package Barracuda VR.

The agglomerates consist of a large amount of primary particles clustered together. They have irregular shapes, sizes and structures, and are therefore difficult to fluidize and handle adequately.

The simulations show that bed agglomeration influences the fluidization characteristics of a bubbling fluidized bed. The pressure drop decreases and the minimum fluidization velocity increases when agglomerates are present in the bed. Moreover, the formation of agglomerates cause large instabilities with uneven distribution of bubbles and channeling that lead to loss of fluidization. When channeling occurs in the bed, there is less contact between gas and particles and the heat and mass transfer operation is weakened. Consequently, de-fluidized zones occur, which in turn can lead to unscheduled shutdowns of the whole installation.

## REFERENCES

[1] Sansaniwal, S.K., Rosen, M.A. & Tyagi, S.K., Global challenges in the sustainable development of biomass gasification: an overview. *Renewable and Sustainable Energy Reviews*, **80**, pp. 23–43, 2017. https://doi.org/10.1016/j.rser.2017.05.215

[2] World Bioenergy Association, *WBA Global Bioenergy Statistics*, 2017.

[3] Basu, P., *Biomass Gasificaion, Prolysis and Torrefaction*, 2nd edn., Academic Press Inc.: UK, 2013.

[4] Bartles, M., Lin, W., Nijenhuis, J., Kapteijn, F. & Ommen, R., Agglomeration in fluidized beds at high temperaures: Mechanisms, detection and prevention. *Progress in Energy and Combustion Science*, **34(5)**, pp. 633–666, 2008. https://doi.org/10.1016/j.pecs.2008.04.002

[5] Wang, L., Weller, C.L., Jones, D.D. & Hanna, M.A., Contemporary issues in thermal gasification of biomass and its application to electricity and fuel production. *Biomass and Bioenergy*, **32(7)**, pp. 573–581, 2008. https://doi.org/10.1016/j.biombioe.2007.12.007

[6] Khadilkar, A.B., Rozelle, P.L. & Pisupati, S.V., Investigation of fluidized bed agglomerate growth process using simulations and SEM-EDX characterization of laboratory-generated agglomerates. *Chemical Engineering Science*, **184**, pp. 172–185, 2018. https://doi.org/10.1016/j.ces.2018.03.035

[7] Furuvik, N.C.I.S., Jaiswal, R. & Moldestad, B.M.E., Flow behaviour in an agglomerated fluidized bed gasifier. *International Journal of Energy and Environment*, **10(2)**, pp. 55–64, 2019.

[8] Moradian, F.A., *Behaviour in Fluidized-Bed Combustion and Gasification of Biomass and Waste Fuels*, Thesis for the Degree of Doctor of Philosophy, University of Borås, Sweden, 2016.

[9] Montes, A., *Factors Affecting Bed Agglomeration in Bubbling Fluidized Bed Biomass Boilers*, Electronic Thesis and Dissertation Repository, September 2014.

[10] Thapa, R.K. & Halvorsen, B.M., Stepwise analysis of reactions and reacting flow in a dual fluidized bed gasification reactor. *WIT Transactions on Engineering Sciences*, **82**, pp. 37–48, 2014.

[11] Chladek, J., Jayarathna, C.K., Moldestad, B.M.E. & Tokheim, L.A., Fluidized bed classification of particles of different size and density. *Chemical Engineering Science*, **177**, pp. 155–162, 2018. https://doi.org/10.1016/j.ces.2017.11.042

[12] Jayarathna, C.K., Moldestad, B.E. & Tokheim, L.A., Validation of results from Barracuda® CFD modelling to predict minimum fluidization velocity and pressure drop of Geldart A particles. *Proceedings of the 58th SIMS Conference*, 2017.

[13] Richardson, J.F. & Zaki, W.N., Sedimentation and fluidisation: Part I. *Chemical Engineering Research and Design*, **75**, pp. S82–S100, 1997. https://doi.org/10.1016/s0263-8762(97)80006-8

[14] Wen, C. & Yu, Y., Mechanics of fluidization. *Chemical Engineering Progress Symposium Series*, **62**, pp. 100–111, 1966.

[15] Kunii, D. & Levespiel O., *Fludization Engineering*, 2nd edn., Butterworth-Heinemann: USA, 1994.

[16] Crowe, C.T., Schwarzkopf, J.D., Sommerfield, M. & Tsuji, Y., *Multiphase Flows with Droplets and Particles*, 2nd edn., Taylor & Francis Group: USA, 2012.

# EULERIAN MULTI-PHASE CFD MODEL FOR PREDICTING THE PERFORMANCE OF A CENTRIFUGAL DREDGE PUMP

NICOLÒ BECCATI[1], CRISTIAN FERRARI[1], MARCO PARMA[2] & MASSIMO SEMPRINI[2]
[1] CNR – IMAMOTER, Institute for Agricultural and Earthmoving Machines of the Italian National Research Council, Ferrara, Italy.
[2] ITALDRAGHE S.P.A., San Giovanni in Marignano, Italy.

## ABSTRACT

Dredge pumps are a complex engineering topic in comparison to water pumps. Mixtures of seawater with several types of soils do not behave as a homogenous fluid, and numerical simulations of these machines can be very challenging. Typical numerical approaches to simulations of dredge pumps are single-phase equivalent slurry and multi-phase liquid–solid, where the specification of the particle flow field can be Eulerian or Lagrangian. The single-phase slurry approach is not sufficient to describe the effects of particle size and concentration of the solid phase on pump performance; for this reason, this paper examines a multi-phase CFD model applied to a dredge pump. The solid phase is modelled with an Eulerian approach, in order to reduce the computational effort required by a Lagrangian method, mainly used for low solid-phase concentrations. The primary purpose of the presented model, developed using commercial software ANSYS CFX, is to predict head losses in a dredge pump working with several particle sizes, from 0.1 to 5 mm, and different volume concentrations of the solid phase, from 20% to 30%. For numerical solid-phase calibration, the effect of the particle size on pump performance is associated with non-Newtonian rheology of the simulated Eulerian phase. The numerical model is validated via experimental tests on the dredge pump using seawater. The calibration of the particle size effect is obtained from scientific literature data about dredge pump losses in different conditions. The model presented could be a useful tool for the analysis of existing dredge pumps or for the design of new machines.
*Keywords: centrifugal pumps, CFD, dredge pumps, Eulerian–Eulerian, multi-phase flow.*

## 1 INTRODUCTION

Centrifugal pumps are often used to handle large amounts of solid-water slurries, with some decrease in performance due to differences in density and flow path with respect to water [1], similar to the effects of non-Newtonian fluids on the impeller [2–4]. Scientific literature on dredge pump design [5–7] provides many correlations and methods in order to predict and measure pump performance using different solid densities, particle sizes and concentrations, based on empirical studies. Empirical equations can provide a good preliminary study for any design concept of a dredge pump, but modern CAE techniques based on numerical simulations may be a more useful tool, if they are calibrated well on the applications to simulate. For this reason, this paper investigates a CFD model in order to provide a calibration algorithm for a multi-phase dredge pump simulation, validated using experimental tests and literature-based equations.

Slurry centrifugal pumps are often studied with CFD techniques, using different approaches like the single-phase equivalent slurry [8], the Eulerian–Eulerian multi-phase [9] or the Eulerian–Lagrangian multi-phase [10]. Every approach has different pros and cons, depending on the spendable computational effort, the physics numerical calibration and the final goal to achieve. For water-sand slurries with high solid-phase concentrations (> 20%), the computational fluid dynamics is often studied with an Eulerian–Eulerian approach [11–14], that permits good results without over-demanding computational simulations (Fig. 1).

<div align="center">(a)            (b)</div>
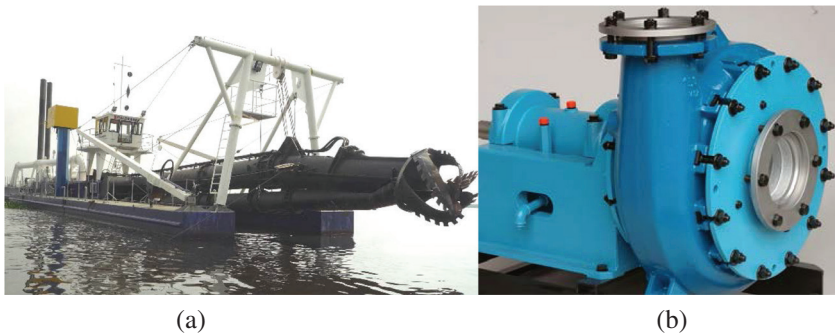
Figure 1: Examples of dredging machinery: (a) offshore dredger;
(b) dredge pump. Courtesy of Italdraghe S.p.A.

## 2 ANALYSED MACHINE

The analysed machine is a centrifugal dredge pump. The impeller has four blades and the rotational speed available is normally around 1000 rpm ($\omega_0$). The pump mostly transports solid particles around 25% volume concentration, with particle diameter sizes in the 0.1–10 mm range, depending on the dredging site. The best working efficient point with seawater is 70 m hydraulic head ($H_0$) at 1000 m$^3$/s flow rate ($Q_0$). The impeller geometry specifications are given in Fig. 2.

### 2.1 Experimental tests

Pump performance was tested on an existing dredging plant, using seawater at 20°C. The hydraulic head was measured with the outlet–inlet pressure difference with analogue



- $b_0$ = 220 mm.
- $b_1$ = 150 mm.
- $b_2$ = 125 mm.
- $b_3$ = 50 mm.

- $d_0$ = 200 mm.
- $d_1$ = 230 mm.
- $d_2$ = 580 mm.
- $d_3$ = 100 mm.

Figure 2: Impeller geometric dimensions.

Table 1: Experimental operating points with seawater.

| $\omega/\omega_0$ | 0.6 | | | 0.7 | | | 0.8 | | |
|---|---|---|---|---|---|---|---|---|---|
| $H/H_0$ | 0.31 | 0.29 | 0.27 | 0.38 | 0.36 | 0.31 | 0.52 | 0.49 | 0.44 |
| $Q/Q_0$ | 0.18 | 0.38 | 0.54 | 0.20 | 0.41 | 0.60 | 0.24 | 0.48 | 0.70 |

pressure gauges, while the flow rate was measured using an ultrasonic flowmeter on the outlet duct. The rotational pump speed was set by regulating the attached diesel motor power. The measured hydraulic head versus flow rate, by varying the pump rotational speed is given in Table 1.

## 3  CFD MODEL

The simulations are carried out with the commercial CFD code ANSYS CFX, Release 19.2 [15]. The code solves the 3D Cauchy momentum equation using an element-based finite-volume method. The geometry is generated using the commercially available software SOLIDWORKS and then imported into the meshing software ANSYS ICEM, in order to mesh the domain. Then, boundary conditions are imposed on the volume, by defining the multiple frames of reference, the transient analysis parameters and the properties of the materials involved. The multi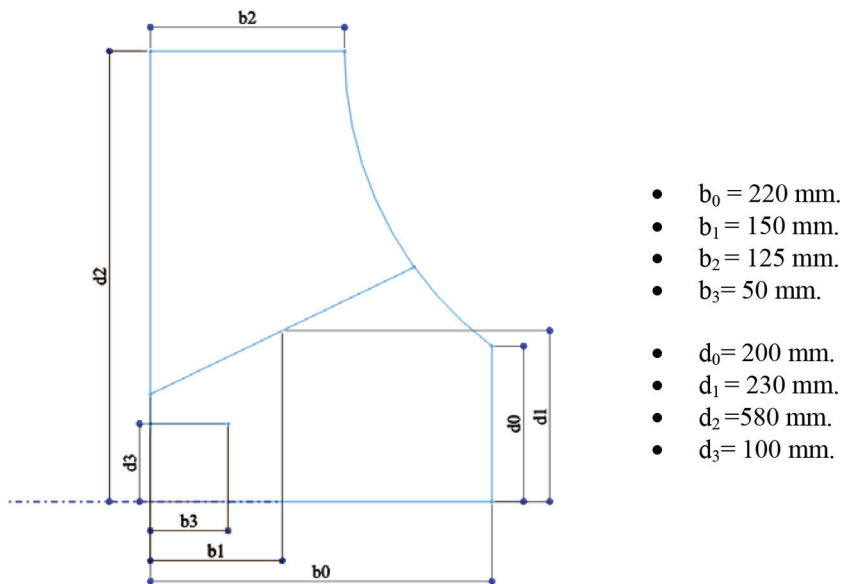phase flow simulations largely use the Eulerian–Eulerian approach for the solutions. This approach is based on the principle of interpenetrating continua [16], where the phases share the same volume. The phases, each of which are described by its physical properties and its own velocity, pressure, concentration and temperature field, share the same volume and penetrate each other in space exchanging mass, momentum and energy. For the issue being investigated, the "Volume of Fluid" model was applied, in order to simplify the multiphase simulations and reduce the computational time effort. The simplification performed makes it possible to solve the bulk transport equations that can be derived by summing the individual phasic transport equations for seawater (w) and solid (s):

$$\rho_m = \sum \rho_i r_i. \tag{1}$$

$$\bar{U}_m = \frac{1}{\rho_m} \sum \rho_i r_i \bar{U}_i. \tag{2}$$

$$\mu_m = \sum \mu_i r_i. \tag{3}$$

$$i = w, s.$$

The equations describing the mathematical model are mass continuity (4), momentum continuity (5) and volume conservation (6). The energy continuity is not simulated for the isothermal hypothesis applied.

$$\frac{\partial}{\partial t}(\rho_m r_i) + \nabla \cdot (\rho_m r_i \bar{U}_m) = 0. \tag{4}$$

$$\frac{\partial}{\partial t}(\rho_m \bar{U}_m) + \nabla \cdot (\rho_m \bar{U}_m \otimes \bar{U}_m) = -\nabla p + \nabla \cdot \left( \mu_m \left( \nabla \bar{U}_m + (\nabla \bar{U}_m)^T \right) \right). \tag{5}$$

$$\sum r_i = 1. \tag{6}$$

These six nonlinear partial differential equations must be solved for the six dependent variables ($U_{mx}$, $U_{my}$, $U_{mz}$, $r_w$, $r_s$, p) [17].

## 3.1  Mesh and grid sensitivity

The pump volume is divided into two finite-volume domains in order to perform a multiple frame of reference simulation: the stationary domain of the volute and a rotational domain of the impeller (see Fig. 3). Between the domains, two interfaces are set with the Mixing Plane model applied as transition from rotor to stator. In this approach, the flow field data are averaged circumferentially from both frames of reference at the interface and passed to the adjacent zone as boundary conditions.

The number of elements is defined after a grid sensitivity analysis, based on the monitoring of the pump hydraulic head. Three grids were generated: mesh 1, composed of $0.5 \cdot 10^6$ elements, mesh 2, composed of $1.3 \cdot 10^6$ elements and mesh 3, composed of $3 \cdot 10^6$ elements. In CFD simulations, the numerical results are dependent from the number of elements of the grid used for the simulations. So, as a first step, it is needed a grid sensitivity analysis on the numerical results, in order to find the minimum number of elements that doesn't affect the numerical results. This permits to reach the independence of the numerical results on the number of elements. When CFD simulations involve turbulence, it is needed a very dense grid on the walls, in order to solve correctly the adhesion effect and solve the boundary layer. The inlet and outlet ducts in the volute domain were elongated in order to make the numerical simulations more stable.

## 3.2  Boundary conditions

All the simulations are carried out as steady-state analysis. The multi-phase model is set as homogeneous, calculating a unique flow field for the materials involved. The hydraulic head versus flow rate curves are calculated by varying the flow rate developed by the pump. The flow rate value is imposed on the outlet surface of the volute, while the inlet surface is set as a constant relative pressure condition. The solid-phase concentration inside the domains is set as the initial overall condition on the simulated volume and on the outlet flow rate. All the walls are set as smooth walls, with a No Slip condition applied (Table 2).



(a)                                                        (b)
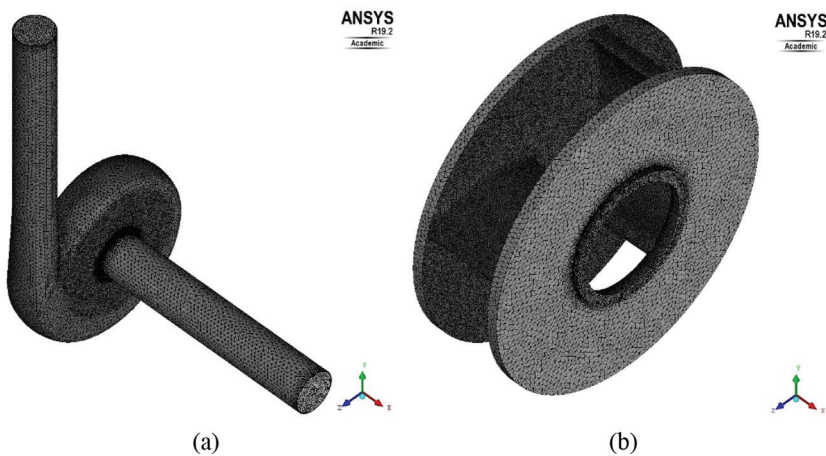
Figure 3: 3D mesh of the dredge pump domains: (a) volute and (b) impeller.

Table 2: Simulation settings applied.

| Setting | Value | Setting | Value |
|---------|-------|---------|-------|
| Seawater density | 1025 kg/m$^3$ | Solid density | 2660 kg/m$^3$ |
| Advection scheme | High Resolution | Turbulence model | κ-ω SST |
| Inlet rel. pressure | 0 bar | Outlet flow rate | 0–3 $Q_0$ |

### 3.3 Seawater simulation results

The validation of the numerical model is reached with single-phase simulations with seawater: once the numerical convergence is reached, with residual criteria set at $10^{-4}$, the hydraulic head, which varies with the flow rate and the rotational speed, is compared with the experimental results. Figures 4 and 5 show a good match between the numerical and the experimental results; the numerical pump model is then validated.
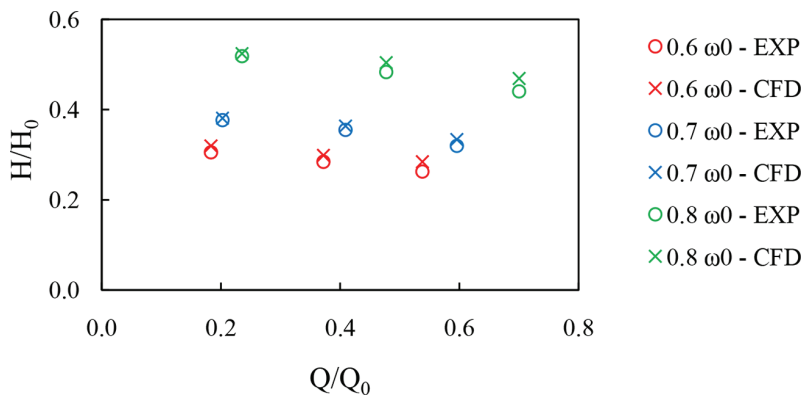


Figure 4: Comparison between experimental and numerical data with seawater.



(a)

(b)
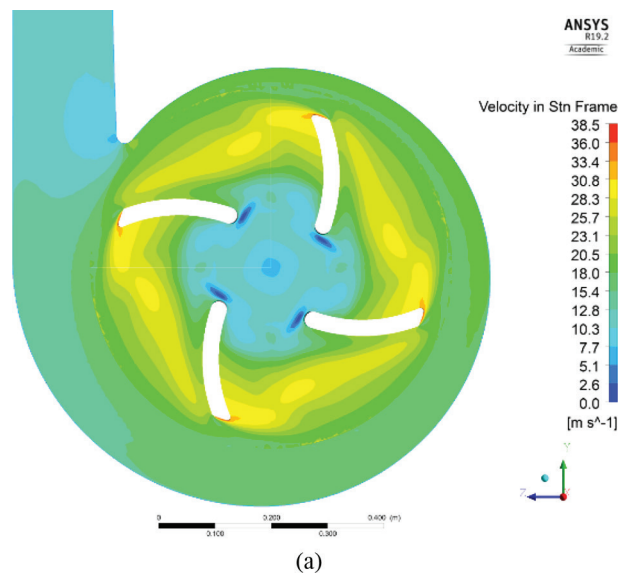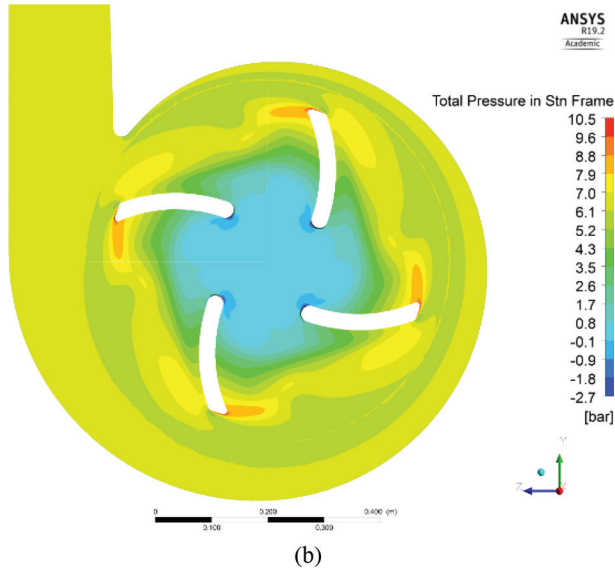
Figure 5: YZ middle-plane contours with seawater: (a) velocity and
(b) total pressure.

## 4  NUMERICAL CALIBRATION

The rheological models that better describe the behaviour of a water–sand suspension like the one presented here are the non-Newtonian models, like the Bingham model [18], the Ostwald–de Waele model [19] and the Herschel–Bulkley model [20–22]. The last one is the model used for the calibration of the Eulerian solid-phase rheology: $\tau = \tau_o + K\dot{j}^n$. (7)

The Herschel–Bulkley model is set on the numerical viscosity properties of the solid phase, in order to match a hydraulic head reduction effect of the non-Newtonian viscosity [23] to the prediction of the head degradation due to the solid effect [24]. While the power index value can be related to the concentration of the solid phase [22], the effect of the particle size is related here to the yield stress value of the viscosity model. The calibration of the yield stress is performed through a sensitivity analysis of the expected head reduction at the fixed particle size with the numerical results by varying the yield stress value on the pump. The prediction of the effect of the particle size on the hydraulic head reduction is calculated with the $K$-factor value, taking into account the effect of the pump radius [3].

For the calibration analysis, the flow rate developed was set constant at $Q_0$ value, while the solid concentration was set at 20% and 30%. For every particle size, the resulting yield stresses at different solid concentrations were mediated, in order to extract a unique value of the yield stress. The calibration curve of the yield stress versus particle size is provided in Fig. 6; the logarithmic trend is used as the formulation in the numerical yield stress setting, following eqn (8). $\tau_0 = 931.8\ln(\theta) + 7540$. (8)

The plastic viscosity value, related to the solid concentration [7], is given by the Thomas eqn (9):

$$K = \mu_w(1 + 2.5r_s + 10.05r_s^2 + 0.00273\exp(16.6r_s)). \tag{9}$$
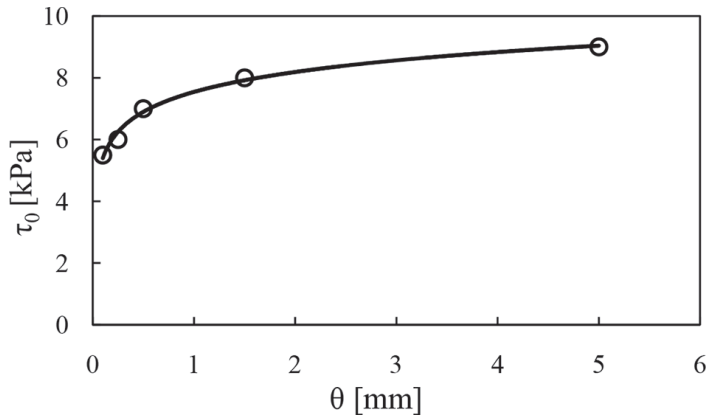
Figure 6: Logarithmic trend curve of yield stress versus particle size.

## 5 RESULTS

The simulations were carried out at five values of particle size, between 0.1 and 5 mm, two values of solid concentrations, 20% and 30%, and seven values of flow rate at constant speed $\omega_0$ (Figs. 7 and 8). The performance curves of hydraulic head versus bulk flow rate were given with a cubic trend line on the resulting points. The hydraulic head was calculated with the following eqn:

$$H = \Delta p / \rho_m g. \tag{10}$$

The results show a hydraulic head reduction, related to seawater, up to 30% developing 5 mm solid size at 30% volume concentration (Fig. 9). The decreasing performance matches the predictions made with the empirical formulae used for calibration at the larger particle
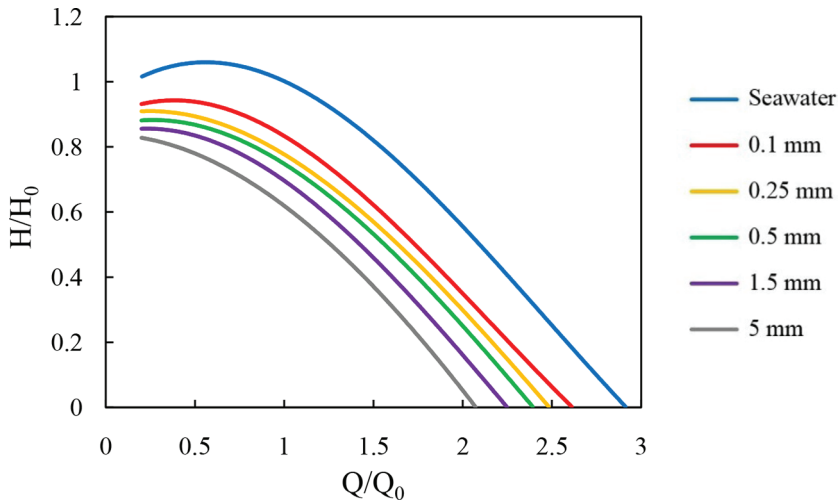


Figure 7: Numerical bi-phase curves with 20% of solid.
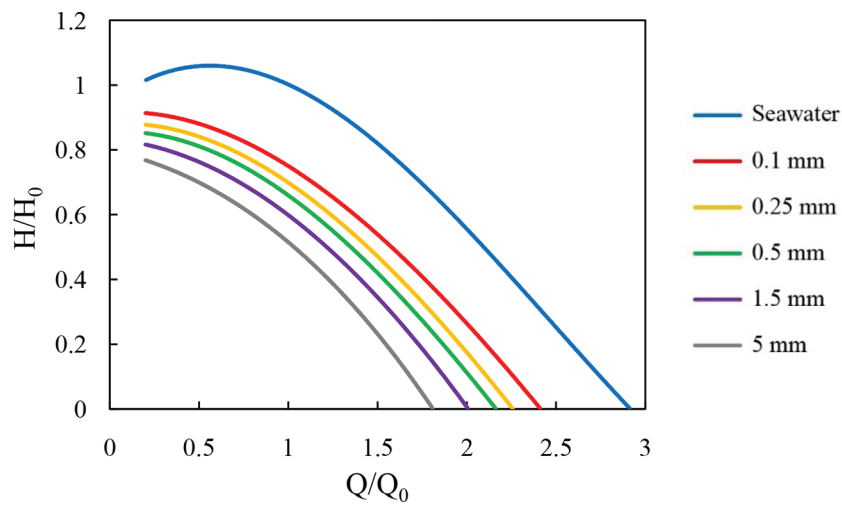
Figure 8: Numerical bi-phase curves with 30% of solid.



(a)
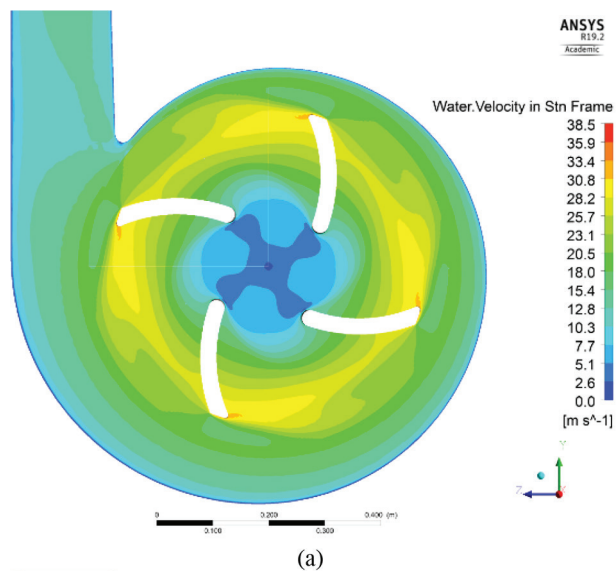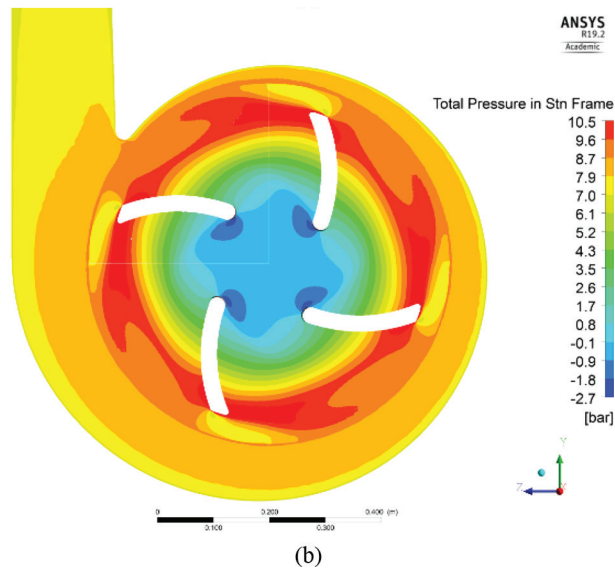
Figure 9: YZ middle-plane contours with 30% concentration of 5 mm solid particles: (a) velocity and (b) total pressure.

sizes. The greatest deviation from the hydraulic head reduction predictions is present at the lower particle sizes, where the numerical results show a 5–10% decrease, while the empirical formulae show 2–3%.

## 6 CONCLUSION

This paper presents a multi-phase CFD model applied to a dredge pump. The slurry is modelled with a two-phase solid–water mixture using an Eulerian–Eulerian approach, in order to better compute the high solid-phase concentrations involved. The numerical model is developed in order to predict the hydraulic head losses at different particle sizes, from 0.1 to 5 mm, using a non-Newtonian viscosity model applied to the Eulerian solid phase. The validation is performed using experimental test performance levels with seawater, while the calibration of the rheology parameters was performed using scientific literature criteria. The results show a good agreement on the hydraulic losses at higher transported particle sizes, while the greatest deviation is reached at lower particle sizes. Using fast simulations, the presented model can analyse the performance levels of existing dredge pumps or predict losses in new dredge pump concepts. Further analysis and improvements on the presented model can be made, for example, by changing the geometry, empirical formulations for loss predictions or exploring other non-Newtonian models for the solid-phase numerical properties.

## NOMENCLATURE

| Variable | Description | Variable | Description |
|---|---|---|---|
| $\omega_0$ | Reference rotational speed | $H_0$ | Best efficiency point hydraulic head |
| $Q_0$ | Bulk volume flow rate at best efficiency point | $b$ | Axial length |
| $d$ | Diameter | $\omega$ | Rotational speed |
| $H$ | Hydraulic head | $Q$ | Bulk volume flow rate |
| $\rho$ | Density | $r$ | Volume fraction |
| $\bar{U}$ | Flow velocity | $\mu$ | Dynamic viscosity |
| $p$ | Pressure | $\tau$ | Shear stress |
| $\tau_0$ | Yield stress | $K$ | Plastic viscosity |
| $\dot{\gamma}$ | Shear rate | $n$ | Power index |
| $\theta$ | Particle size | $g$ | Standard gravity |

## REFERENCES

[1] Gülich, J.F., *Centrifugal Pumps*, 3rd edn., Springer-Verlag Berlin Heidelberg, pp. 929–40, 2014.

[2] Karassik, I.J., Messina, J.P., Cooper, P. & Heald, C.C., *Pump Handbook*, 4th ed., The McGraw-Hill Companies, Inc., 2008.

[3] Wilson, K.C., Addie, G.R., Sellgren, A. & Clift, R., *Slurry Transport Using Centrifugal Pumps*, Springer Science+Business Media, Inc., 2006.

[4] Buratto, C., Occari, M., Aldi, N., Casari, N., Pinelli, M., Spina, P.R. & Suman, A., Centrifugal pumps performance estimation with non-Newtonian fluids: review and critical analysis, *Proceedings of 12th European Conference on Turbomachinery Fluid dynamics & Thermodynamics*, pp. 1–13, 2017.

[5] Herbich, J.B., *Handbook of Dredging Engineering*, 2nd ed., McGraw-Hill Professional, 2000.

[6] Vlasblom, J.W., *Dredge Pumps*, Delft University of Technology Lecture notes, 2004.

[7] Miedema, S.A. & Ramsdell, R.C., *Slurry Transport: Fundamentals, A Historical Overview & The Delft Head Loss & Limit Deposit Velocity Framework*, Delft University of Technology, 2016.

[8] Ye, D.X., Li, H., Zou, C.H. & Jiang, B., Characterization of the fluidization of medium consistency pulp suspensions in a centrifugal pump, *WIT Transactions on Engineering Sciences*, **89**, pp. 67–76, 2015.

[9] Pagalthivarthi, K.V., Gupta, P.K., Tyagi, V. & Ravi, M.R., CFD predictions of dense slurry flow in centrifugal pump casings. *International Journal of Mechanical and Mechatronics Engineering*, **5(3)**, pp. 538–550, 2011.

[10] Shen, Z., Chu, W., Li, X. & Dong, W., Sediment Erosion in the Impeller of a Double-suction Centrifugal Pump-A case study of the Jingtai Yellow River Irrigation Project, China, Wear.

[11] Nabil, T., El-Sawaf, I. & El-Nahhas, K., Sand-water slurry flow modelling in a horizontal pipeline by computational fluid dynamics technique, *Int. Water Technol. J*, **4(1)**, pp. 1–17, 2014.

[12] Wanker, R., Goekler, G. & Knoblauch, H., Numerical modeling of sedimentation utilizing a Euler/Euler approach, *WIT Transactions on Engineering Sciences*, **30**, pp. 327–336, 2001.

[13] Yang, J. & Chalaturnyk, R.J., Computational fluid dynamics simulation of a very dense liquid-solid flow using a Eulerian model. *WIT Transactions on Engineering Sciences*, **50**, pp. 305–314, 2005.

[14] Tebowei, R., Hossain, M., Oluyemi, G. & Islam, S., Modelling effects of particle size and pipe gradient on sand transport in multiphase pipes. *WIT Transactions on Engineering Sciences*, **89**, pp. 323–334, 2015.

[15] ANSYS, Inc., *ANSYS CFX-Solver Theory Guide*, Release 19.2, 2018.

[16] Enwald, H., Peirano, E. & Almstedt, A.E., Eulerian two-phase flow theory applied to fluidization. *Int. J. Multiphase Flow*, **22**, pp. 21–66, 1996.

[17] Hiltunen, K., Jäsberg, A., Kallio, S., Karema, H., Kataja, M., Koponen, A., Manninen, M. & Taivassalo, V., *Multiphase Flow Dynamics Theory and Numerics*, VTT Publications 722, Edita Prima Oy, Helsinki, 2009.

[18] Shakibaeinia, A. & Jin, Y.C., Lagrangian multiphase modeling of sand discharge into still water, *Advances in Water Resources*, **48**, pp. 55–67, 2012.

[19] Konijn, B.J., Sanderink, O.B.J. & Kruyt, N.P., Experimental study of the viscosity of suspensions: Effect of solid fraction, particle size and suspending liquid, *Powder Technology*, **266**, pp. 61–69, 2014.

[20] Olhero, S.M., Ferreira & J.M.F., Influence of particle size distribution on rheology and particle packing of silica-based suspensions, *Powder Technology*, **139**, pp. 69–75, 2004.

[21] Mueller, S., Llewellin, E.W. & Mader, H.M., The rheology of suspensions of solid particles, *Proceedings of the Royal Society A: Mathematical, Physical and Engineering Sciences*, **466(2116)**, pp. 1201–1228, 2010.

[22] Mangesana, N., Chikuku, R.S., Mainza, A.N., Govender, I., van der Westhuizen, A.P. & Narashima, M., The effect of particle sizes and solids concentration on the rheology of silica sand based suspensions. *The Journal of The Southern African Institute of Mining and Metallurgy*, **108**, pp. 237–243, 2008.

[23] Li, W.G., Effects of viscosity of fluids on centrifugal pump performance and flow pattern in the impeller. *International Journal of Heat and Fluid Flow*, **21(2)**, pp. 207–12, 2000.

[24] Engin, T. & Gur, M., Comparative evaluation of some existing correlations to predict head degradation of centrifugal slurry pumps. *ASME Journal of fluids engineering*, **125(1)**, pp. 149–57, 2003.

*This page intentionally left blank*

# A VALIDATION STUDY FOR A NEW EROSION MODEL TO PREDICT EROSIVE AIRFOIL DEFOULING

ARTHUR RUDEK[1,2], DAVID MUCKENHAUPT[1], THOMAS ZITZMANN[1],
GERALD RUSS[1] & BARRY DUIGNAN[2]
[1] Hochschule Darmstadt, University of Applied Sciences, Germany.
[2] Technical University Dublin, Ireland.

## ABSTRACT

A new defouling erosion model for Lagrangian particle tracking is used to predict defouling of amorphous, heterogeneous coatings such as those typically found in aircraft compressors. The main problem description, the mathematical formulation and the underpinning experiment of the model are presented in a previous communication by the authors. In this work, the Ansys CFX implementation of the model is described and an experiment is presented for the validation of the model. Air flows laden with a number of dry-ice particles are observed in an optically accessible stream channel containing a flat plate target. The defouling process of these particles is recorded with HSCs and the main parameters, such as indentation size in fouling layers, are processed and compared to corresponding numerical results. The model parameters considered are particle impact velocity and angle as well as particle and fouling material. Typical coatings which are relevant to commercial aircraft defouling processes are investigated. The target plate angle and the air velocity are varied and dry-ice particles of random size and shape are injected into the flow. The experiment is set up in a wind-tunnel test-rig and all recordings are made using two HSCs, a digital camera and Prandtl probe measurement. Experimental and numerical defouling results show good overall agreement for steep target angles but significant deviations for low target angles. Potential improvement to the defouling erosion model is discussed based on these results. The model as presented is used in large-scale compressor defouling simulations in the development process of on-wing aircraft maintenance systems.
*Keywords: aircraft engine defouling, $CO_2$ dry-ice blasting, solid particle erosion, validation experiment.*

## 1 INTRODUCTION

On-wing aircraft engine cleaning is a current topic of research for commercial aircraft operators. Engine maintenance cost represents approximately 35% to 40% of an airline's total maintenance cost [1]. Periodic on-wing engine cleaning results in greater operating efficiency and lower emission rates. In this work compressor defouling is addressed. Compressor fouling is mainly caused by in-service ingestion and deposition of various types of solid and fluid foulants from ambient air, such as unburned hydrocarbons, insects, soil, salt, etc. [2–4]. This leads to decreased engine efficiency and power output and higher fuel consumption, pollutant emission and increased operational cost [3, 5–10]. To counteract this, a number of aircraft engine compressor defouling systems have been developed in recent decades. These are mostly based on solid (e.g. coal-dust, nut-shells) or liquid (e.g. water droplets, solvents) particle injection into the engine core while the engine is dry cranked [10–13]. The most recent research at Hochschule Darmstadt (hda) and Dublin Institute of Technology (DIT) in cooperation with Lufthansa Technik AG (LHT) resulted in the new Cyclean 2.0 cleaning system which is based on pressurized air which carries dispersed $CO_2$ dry-ice particles. The particles clean the compressor blades by erosive wear. The basic principles of the system are described in [14]. Further details of the system including particle laden in-engine flow investigations and simulations are described by the authors in [15, 16] and the entire study dealing with numerical simulations of the novel Cyclean 2.0 cleaning procedure is described in detail in [17].

## 2  STATE OF THE ART

The numerical simulation of the new Cyclean 2.0 cleaning system operating with dry-ice was one of the key goals in the research mentioned above. The simulations must be carried out with the commercial numerical code ANSYS CFX and must incorporate an appropriate erosion prediction formulation. The Ansys CFX code incorporates a number of erosion models which are typically used in turbomachinery, such as those from FINNIE [18] and GRANT and TABAKOFF [18]. However, an extensive literature review, most of which was presented in RUDEK *et al.* [15] by the authors, revealed that no erosion model is available at present, which is capable of predicting the erosion of amorphous and heterogeneous coating materials, such as fouling layers typically found on aircraft engine blades.

To address this, the new energy-based erosion model introduced by the authors in Rudek *et al.* [15] was developed. It uses the experimental "Dynamic Indentation Testing" (DI) in order to determine the behavior of fouling material under erosion during engine cleaning. Several other researchers have taken a comparable approach to determine the erosion of technical coatings, such as paint, and their work is summarized in detail in Rudek *et al.* [15] and briefly described below.

The new defouling erosion model considered in this work is based on an energy balance comparable to the dynamic hardness definition by Sundararajan *et al.* [19]

$$Hd := \frac{\frac{1}{2} \cdot m_P \cdot \left(v_{p,1}^2 - v_{p,2}^2\right)}{V_{imp}} = \frac{1}{2} \cdot \frac{m_P}{V_{imp}} \cdot v_{P,1}^2 \cdot \left(1 - \varepsilon^2\right) \tag{1}$$

who introduced an energy-based model to predict crater volume $V_{IMP}$ and particle rebound characteristics (described by the particle mass $m_P$ and its velocity before $v_{P,1}$ and after impact $v_{P,2}$) in solid material erosion processes. They used the coefficient of restitution in eqn. (1)

$$\varepsilon = \frac{v_{P,2}}{v_{P,1}} \tag{2}$$

to assess the energy consumed by the particle–wall interaction.

The defouling erosion model presented is underpinned with data acquired by means of single particle experiments comparable to the DI testing procedure presented by Hutchings *et al.* [20, 21] and Sundararajan *et al.* [19, 22]. From this experiment, it is possible to determine the amount of energy necessary to penetrate and remove certain portions of typical foulants from aircraft compressor airfoils and to predict the amount removed. The experiment is designed under the constraints of the main conditions for DI testing reported in [19, 22], which are

- quasi-static impact behavior,
- negligible stress-wave energy losses,
- negligible particle rotation,
- particle hardness must be greater than target (i.e. fouling) hardness,
- superposition of erosion from normal and tangential forces is possible.

Following [20, 21, 23, 24] it is assumed that the defouling process is independent of particle material and therefore reference material particles, which do not disintegrate on impact,

are used for rebound testing. The results are adapted to dry-ice particles using empirical defouling functions. A procedure comparable to this was reported and extensively examined by PAPINI and SPELT in their decoating studies [23, 25, 26].

Gondret *et al*. [27, 28] investigated various material pairings in a range of particle impact tests and reported similarity in their restitution behavior if the coefficient of restitution is described as a function of the near-wall Stokes number

$$St_c = m_P \cdot \frac{v_P}{6 \cdot \pi \cdot \eta_c \cdot r_P^2} = \frac{1}{9} \cdot \frac{\rho_P \cdot v_P \cdot d_P}{\eta_c} \tag{3}$$

which was derived from the particles ODE of motion in near wall formulation only considering viscous forces (index: c for coating) and which incorporates the influence of particle size (radius *r* and diameter *d*), mass $\rho$, and velocity *v*.

A similar procedure is used in the underpinning experiment of the erosion model used in this work to measure foulant properties with non-disintegrating particles made from reference material and to adapt these findings to dry-ice particles. Comparable normalization approaches have been reported in [29, 30].

Based on the findings reported in [25, 29–31] it was expected that the energetic properties of the defouling process are measurable only in a certain range of normal impact velocities, which was demonstrated in [17]. Furthermore, there various angular dependencies of the defouling rates are considered for various fouling materials following [32]. Brittle and ductile material behavior was taken into account when the impact angles were chosen for the new experiment (i.e. 90° and 30° measured parallel to the wall), following for example [33, 34].

## 3  MODEL DESCRIPTION

The following model description represents a modified formulation of what was reported in [15] by the authors and it is adapted from RUDEK [17]. The model calculates particle energy dissipation during fouling erosion and measures defouling.

Basically following Gondret *et al*. [27, 28], the process is assumed to be dependent on the near-wall Stokes number, eqn. (3) but it utilizes the viscosity of ambient air instead of the viscosity of the coating. The formulation

$$\delta_e^{\{part,fou,a\}} = \frac{\rho_{ref}}{2} \cdot \delta\varepsilon^{\{fou,0\}} \cdot \left( v_1^{\{ref\,EQ,0\}} \right)^2 \cdot F_{IMP}^{\{part,fou,a\}} \tag{4}$$

is used to describe the energy dissipation $\delta\varepsilon^{\{fou,0\}}$ of a certain particle on impact upon a fouled target and to assess the proportion of defouling energy $\delta e^{\{part,fou,a\}}$, which is necessary to indent and to remove a proportion of fouling. It is adapted from the dynamic hardness definition, eqn. (1).

Defouling energy $\delta e$ is related to empirical restitution data from reference particle material impacts (index: *ref* ) and, if necessary, is scaled with a defouling relation $F_{IMP}$ to any particle material. The superscript is important to this formulation and it reads as follows:

- *part* = particle material (i.e. *refEQ* = reference material at equivalent velocity),
- *fou* = fouling material,
- α = impact angle (i.e. 0 = normal to the wall).

The product of the first three contributors to the right-hand side of eqn. (4) describes reference material dissipation at dry-ice equivalent velocity. It is used to consider the difference in dissipated energy from impacts of non-disintegrating reference material particles in the normal direction on clean and fouled targets

$$\delta\varepsilon^{\{fou,0\}} := \left[\left(\varepsilon^{\{0\}}\right)^2 - \left(\varepsilon^{\{fou,0\}}\right)^2\right] \tag{5}$$

and $\delta\varepsilon$ is defined to be the impact dissipation factor. It is derived from experimental data of reference particle rebounds measured in the normal direction to the wall's surface (superscript: 0). Therefore the normal component of reference material particle impact velocity, which is normalized to a dry-ice equivalent (superscript: *ref EQ*) is used in eqn. (4). This dry-ice equivalence is derived from Stokes-number comparison of the investigated particles (here dry-ice) to those made from reference material. The variable $\delta\varepsilon$ is assumed to be dependent on fouling material (superscript: *fou*) only.

The fourth contributor to the right-hand side of eqn. (4) represents the scale function

$$F_{IMP}^{\{part,fou,a\}} = \left(\frac{d_{IMP}^{*\{part,fou,a\}} \cdot d_P^{\{part\}}}{d_{IMP}^{*\{part,fou,0\}} \cdot d_P^{\{ref\}}}\right)^2 \tag{6}$$

and its superscript indicates that it is a function of particle material (*part*), fouling material (*fou*) and impact angle (*α*). The purpose of this function is to scale the proportion of defouling energy calculated by means of the dissipation factor. This dissipation factor is assumed to be dependent on the proportion of fouling removed from reference material indentations and the function above is used to account for actual proportions of defouling energy consumed to indent the same fouling material by any particle material at any impact angle.

Both areas (i.e. that defouled by reference material and that defouled by the actual material investigated) are calculated by means of the experimentally correlated indentation diameter

$$d_{IMP}^{*\{part,fou,a\}} = \begin{cases} 0 & St \le St_{crit} \\ K_2^{\{part,fou,a\}} \cdot \ln(St) + K_1^{\{part,fou,a\}} & St > St_{crit} \end{cases} \tag{7}$$

with the correlation coefficients $K_1$ and $K_2$. The onset of erosion for the particle-fouling combination under consideration is described by the critical Stokes number $St_{crit}$.

The quotient described from eqn. (6) is used to scale the dissipated portion of energy consumed by the defouling from reference material (*ref*) values to actual material (*part*) values. The defouled area $A_{IMP}$ from one single particle impact is consequently calculated:

$$A_{IMP}^{\{part,fou,a\}} = \frac{\pi}{4} \cdot \left(d_{IMP}^{*\{part,fou,a\}}(St) \cdot d_P^{\{part\}}\right)^2 \tag{8}$$

## 4  EXPERIMENTAL SET-UP

A wind-tunnel experiment is designed in order to create an optically accessible validation scenario towards the new defouling erosion model and this set-up is shown in Fig. 1 with the main dimensions. This testing section is directly flanged to the nozzle of the wind-tunnel, which delivers the air flow (a) at various air velocities.
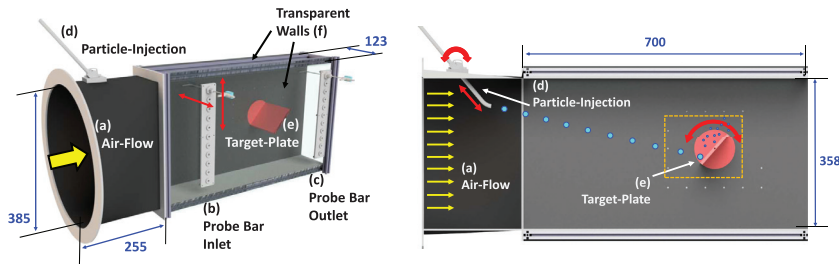
Figure 1: Experiment for numerical validation: schematic (left) and section view (right).

Probe bars (b) and (c) are used for the positioning of Prandtl probes with integrated thermocouples (type K) and these are located at the inlet and the outlet of the rectangular shaped main part of the testing section. These probes are used to measure flow properties such as pressure, velocity and temperature. Flow profiles can be recorded in both horizontal and vertical directions, as indicated by the red arrows in the figure. A number of particles can be introduced into the air-flow via the tubular injection system (d) and these are transported by the flow and impact upon the target plate (e).

The vertical and angular positions of the injection tube as well as the angle of the target plate can be varied, as indicated by the red arrows in Fig. 1, right. The testing section is optically accessible through transparent upper and side walls (f) which make the utilization of HSCs possible for tracking and sizing of primary and secondary dry-ice particles. An exchangeable target plate is used for defouling tests (not shown) with which defouling action is measured after a number of particle impacts. To achieve this, images of the target plate surfaces are recorded before and after particle impacts outside the testing section and these are compared by image post-processing.

## 5 MAIN RESULTS

Initially a pure air-flow run-up study is carried out and a representative selection of results is presented here. Furthermore, the most important findings of the final particle laden flow simulations are highlighted. The whole study presented in [17] comprises a systematic grid study, the discussion of a symmetry assumption and the extensive comparison of numerical to experimental results for air flow properties. Based on this, the numerical set-up for the main validation case investigations of the newly developed models is chosen. A parameter discussion is presented to determine the predictive capabilities of the models in conjunction with Ansys CFX simulations. Experimental data are recorded for defouling erosion and numerical results are compared to experimental data.

It is assumed that the behaviour of the validation experiment can be numerically predicted by considering a mid-plane cut through the rectangular part of the experimental set-up, assuming periodical symmetry at its sides. This assumption is based on preliminary experimental observations of POM and dry-ice particle tracks and flow field measurements. The particles are injected at the mid-channel and in all cases considered they impact the target in the central 33% of the channel. In order to show that side wall effects do not significantly influence the mid-plane flow, flow parameters were measured at a grid of locations across a number of vertical and horizontal positions across the section at the inlet and at the outlet planes of the channel and the results from this study are presented in detail in Rudek [17].

## 5.1  Pure air flow validation

In this section, results from steady-state RANS air flow simulations are compared to experimental data recorded in the mid plane of the channel at all vertical positions. Figure 2 shows simulation results of the two most extreme flow conditions (i.e. case 1 with lowest velocity and lowest target angle and case 4 with highest velocity and highest target angle).

Contours of static pressure are projected to the rear symmetry plane of the numerical volume and velocity streamlines are drawn from the inlet to the outlet plane. A wake region is clearly visible for both cases and the target influence upon the pressure field is also clearly visible. A high forebody and low afterbody pressure field is found to establish and it is mainly influenced by the air velocity and the target plate angle.
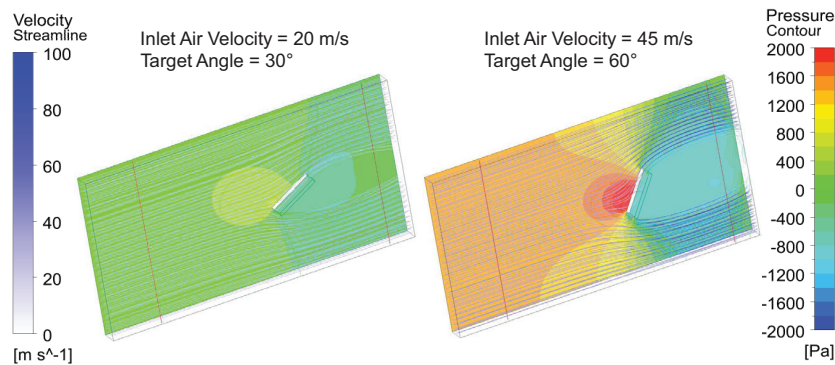


Figure 2: Numerical results for pure air flow in mid-plane symmetry volume for case 1 (left) and case 4 (right) - velocity streamlines and contours of static pressure are shown (Note: steady state RANS simulations cannot capture possible velocity fluctuations downstream the target plate, only the mean flow pattern is predicted).

A typical comparison of pressure and velocity profiles at the afterbody measurement plane (both forebody and afterbody measurement positions are indicated by the red vertical lines in Fig. 2 is shown in Fig. 3 for case 4. The predicted pressure and velocity trends are comparable to the experimental data and the mean deviations between predicted and experimental data
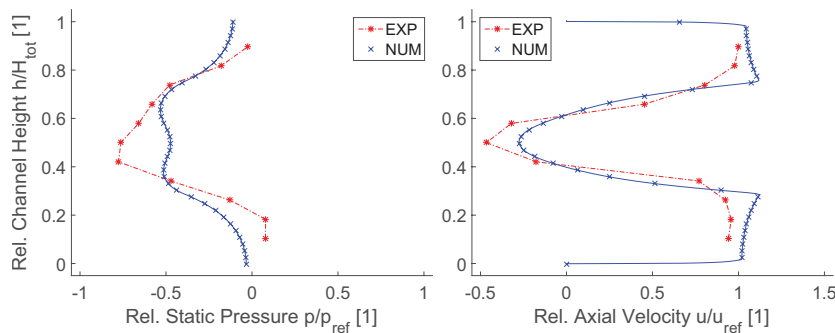


Figure 3: Case 4: air flow pressure (left) and velocity (right) profiles at the outlet plane - comparison of numerical to experimental data.

are 12% for the pressure profile and 16% for the velocity profile. A more detailed discussion of this air-flow validation study is presented in Rudek [17]. Based on these results the set-up is assumed to be valid for the later particle model validation simulations.

## 5.2  Particle tracking validation

In the second step of the run-up study, experiments and simulations using polyoxymethylene (POM, i.e. used as reference material) particles are compared to assess the ability of the simulation to predict particle transportation and impact behavior. Particle injection is implemented in the numerical set-up by setting the initial particle velocity vector and its position in vertical direction at the inlet boundary corresponding to data measured in the experiment.

Whilst the continuous air flow is simulated by means of the Euler approach using the energy equation and Newtons material law, the dispersed particle phase is simulated by means of Lagrangian particle tracking. Therefore, the particle ODE of motion

$$m_P \cdot \frac{d^2 X_P}{dt^2} = \sum_{i=1}^{n} F_i \qquad (9)$$

is solved in the area of interest. It relates particle inertia forces (represented by its mass $m_P$ and its acceleration) to the sum of $n$ external forces $F_i$ acting on this particle.

Figure 4, left, shows a montage of typical experimental recordings of a POM particle with a diameter of 3.0 mm at various instants of time pre- and post-impact. The corresponding pre- and post impact angles of the particles are measured with respect to the horizontal plane of the set-up (indicated in the figure). Hence, negative angle values indicate negative vertical particle velocity components. The particle velocity is post-processed with the recordings using in-house developed procedures such as those presented in [17, 35, 36].

The comparison of the data from the run-up study with various POM particles is displayed in Fig. 4, right. The diagram shows the pre- and post-impact flight path angles of the particles (i.e. measured to the horizontal as explained in the discussion above) and the absolute
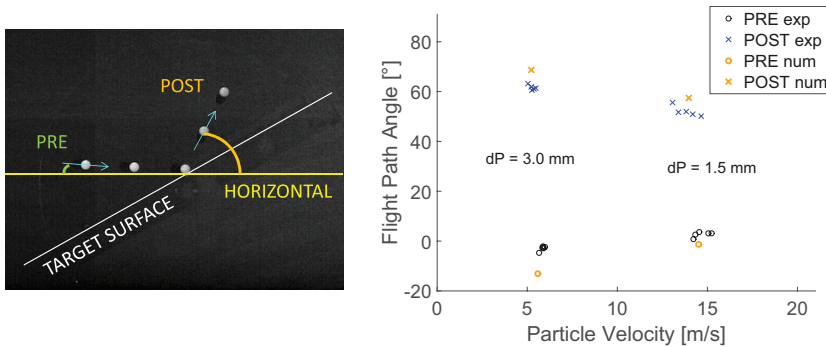


Figure 4: Montage of typical HSC POM particle track recordings at various pre- and post- impact instants of time (left) and comparison of numerical and experimental POM particle tracking results - particle impact behavior (right).

pre- and post-impact velocity values from both numerical and experimental results. Satisfactory agreement between numerical and experimental data is achieved with the simulation set-up chosen.

Particle velocities prior to and after the instant of collision with the target plate are found to be precisely predicted. The impact angles are underpredicted and, as a consequence, the outbound angles are overpredicted. These deviations are more significant for larger particles at lower velocities. Possible causes for the deviations are the simplifications of the simulation assuming constant coefficients of restitution, such as given in eqn. (2), and neglecting rotation of the particles.

The overall agreement of all numerical data compared to experimental results is satisfactory. The mean deviations of the particle velocities range from 1% to 5% and these of the angles range from 5% to 12%. Parts of the study were carried out with the opening boundary condition at the outlet of the numerical control volume and this leads to more significant deviations in the pressure profiles predicted at this position which is discussed in detail in [17]. However, the particle tracks seem to be independent of these deviations and it can therefore be concluded that the set-up chosen is adequate for all validation cases considered.

## 5.3 Defouling erosion validation

The set-up presented above is assumed to be valid for the prediction of the main validation situations presented here and it is used to assess the predictive capabilities of the CFX implementation of the new defouling erosion model. A grid is used which gives results independent from spatial discretization and the mid plane cut is applied because the above study showed no influence of the side walls upon the particle tracks in the middle of the experimental set-up. In addition, the boundary conditions applied showed no negative influence upon the predicted particle tracks.

If the dry-ice particles collide with solid walls they disintegrate into smaller fragments and a proportion of the fouling is removed from the airfoil. To account for this breakup process in the simulations, an experimentally based particle breakup model and the new defouling erosion model for dry-ice particles have been developed and the basic assumption of both models is an energy balance. Mass

$$m_P = \sum_{j=1}^{k} m_i + \delta m_{sub} \tag{10}$$

and kinetic energy (index $kin$)

$$E_{P,kin} = \sum_{j=1}^{k} \left( E_{i,kin} + E_{i,bu} \right) + E_{sub} + E_{er} \tag{11}$$

of the impacting particle (index $P$) are conserved by balancing the impacting particle variables with those of the $k$ secondary particles in the new numerical breakup procedure.

All dispersed secondary particles and the sublimated proportion of primary particle mass (index $sub$) are considered in the mass balance, eqn. (10). The energy balance, eqn. (11), accounts for the kinetic energy, the breakup energy (index $bu$), the sublimated energy proportion and the energy proportion used for the defouling erosion (index $er$) on its right-hand side. The last contribution is derived directly from the dissipated energy portion, eqn. (4), of the

new erosion model. More detailed descriptions of the new particle breakup model can be found in [16, 17] and will be reported by the authors in an additional future communication.

In the validation experiment a HSC is used to record the primary particles impacting the target plate. An exchangeable target surface is used, which is coated with either PTFE or SALT and photographed before starting the experiment. After a certain number of primary particle impingements (i.e. 30–50 per parameter) the target plate is removed and its partially defouled surface is photographed again. A before-after comparison, comparable to what is described in RUDEK *et al.* [15], delivers the desired defouling statistics.

Numerical simulations are carried out of this validation situation and the primary particle injection position, velocity, direction and size distribution are derived from experimental measurements. The experimental parameters used for the defouling tests are approximately 25 and 50 m/s nominal air velocity as well as 30° and 60° nominal target angle. The two artificial fouling materials, PTFE and SALT, are used for each parameter.

This results in a total of 8 tests, each of which was experimentally carried out twice. In the corresponding numerical simulations a total of 30 primary particles was considered for each parameter. Typical results from numerical defouling predictions are presented in Fig. 5: the left-hand image shows little defouling of the SALT layer in the case of 25 m/s nominal air velocity and 30° target angle compared to significant defouling of PTFE with 45 m/s nominal air velocity and 60° target angle.
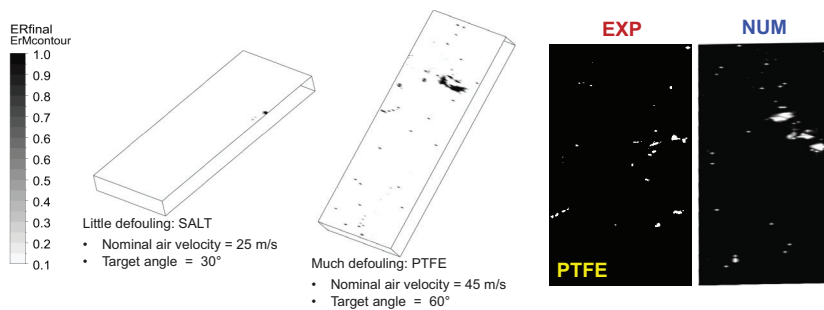


Figure 5: Typical indentation pattern from defouling simulations - little defouling of SALT coating and significant defouling of PTFE coating (both left); qualitative comparison of typical indentation pattern from predicted and experimental defouling of PTFE with the color map inverted (right).

A qualitative comparison of predicted defouling to experimental results is shown in Fig. 5, right, and a typical pattern from PTFE coating is displayed. The comparability of the defouling pattern can be seen. From this comparison it becomes clear that secondary particle indentations play a key role in PTFE defouling. This is not the case for SALT (here without display). For this reason the first comparison of numerical to experimental data deals with the number of indentations per primary particle and this is presented in Fig. 6.

The left-hand display shows results from PTFE testing and the right-hand display those from SALT layer investigations. Both diagrams show mean values from 8 experiments and 4 corresponding simulations. Increasing the primary particle Stokes numbers increases the number of indentations per particle and this can be seen for both PTFE and SALT layers. The mean values for PTFE are higher compared to those for SALT, which indicates that secondary

Figure 6: Number of indentations per primary particle from tests with PTFE
(left) and SALT (right) - numerical (blue markers) and experimental
data (red markers).

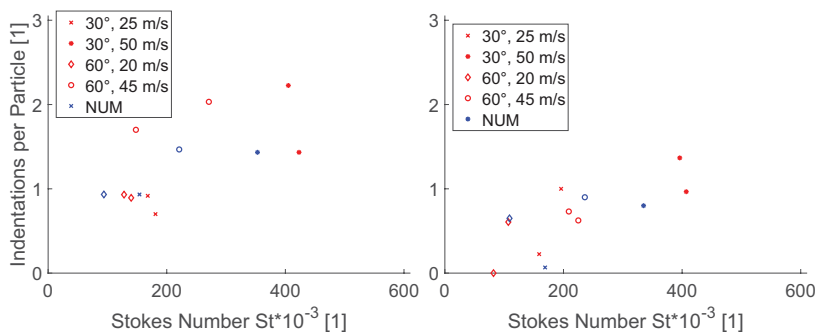particle impacts only partially defoul the PTFE layers. The numerical predictions are compa-
rable to the experimental results and it is therefore concluded that the primary particle
indentation behavior as well as secondary particle indentations are generally captured by the
model set-up presented.

The next comparison deals with the indentation sizes after the defouling tests and it is
presented for PTFE in Fig. 7 and for SALT in Fig. 8. The left-hand display of Fig. 7 shows
the mean values and scattering bars for low target angle (i.e. 30°) and both nominal air
velocities and the right-hand graph shows comparable results from steep target angles
(i.e. 60°).

In both cases the mean numerical values tend to overpredict the mean experimental out-
comes. Good agreement can be seen when comparing the overlapping of the scattering
ranges. However, the lower range of indentation diameters is not captured by the simulations.
This can be attributed to the actual contribution of very small secondary particles defouling,
of which thousands actually exist but just a number is simulated (for details see Rudek [17]).
The predictions for steep target angles are closer to the experimental data compared to these
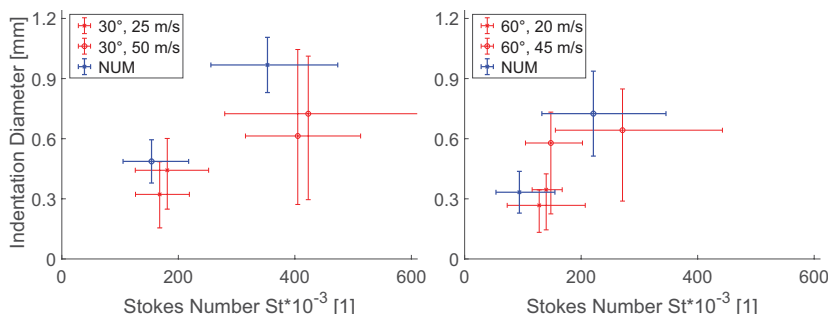for low target angles.



Figure 7: Indentation sizes from tests with PTFE at low (left) and steep target
angles (right) - comparison of numerical (blue markers) to
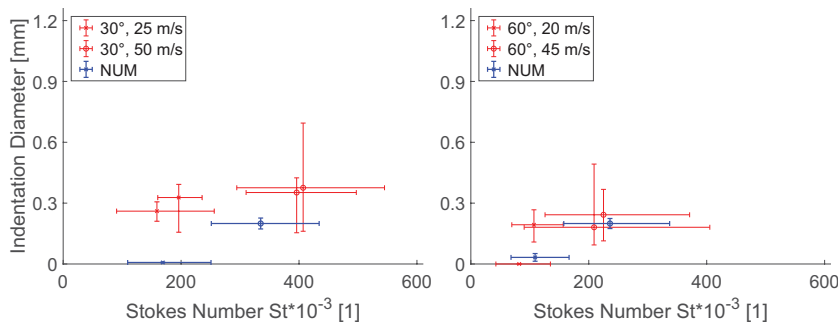experimental data (red markers).

Figure 8: Indentation sizes from tests with SALT at low (left) and steep target angles (right) - comparison of numerical to experimental data.

Results from SALT defouling investigations are shown in Fig. 8 in a comparable representation. The mean numerical results for low target angles clearly underpredict the experimental results. In case of the low nominal velocity there is almost no defouling predicted but there are significant indentations detected in the experiment. The predictions for the higher nominal velocity also underestimate the reality, however these are found to be located in the lower scattering bound of the experimental data. In contrast, the comparison of numerical to experimental data for steeper target angle indentations, Fig. 8, right, shows good agreement of the mean values. The predicted scattering bars of the indentation sizes are much narrower compared to the experimental data. A possible cause for this may be natural scattering experimentally encountered for salt layer defouling, which is not accounted for in the model at the moment (for details see Rudek [17]).

## 6 CONCLUSION AND OUTLOOK

Based on the above results it is concluded that the CFX implementation of the new defouling erosion model, if it is used in conjunction with the new particle breakup model which is not discussed in this communication, adequately predicts actual defouling of PTFE and SALT layers. However, it must be noted that it failed to predict the defouling of SALT in the validation study at low nominal air velocity and low target angle. The lower bounds of the experimental scattering of the PTFE defouling are not captured by the model. In addition the model underpredicts the scatter for SALT defouling. The mean values predicted are in satisfactory agreement with the experimental data for high target angles (mean deviations ca. 15%) but show significant differences for low target angles (mean deviations ca. 40%).

The major differences between the PTFE and SALT layer defouling are well predicted for high target angles and those for the low target angle are found to be within the range of experimental scatter, despite the case where the model failed to predict defouling. Furthermore, the particle breakup model used can be seen to be valid in conjunction with the defouling erosion model because secondary particle indentations are predicted when investigating PTFE defouling.

Potential improvement to the defouling erosion model presented can be achieved by the consideration of scattering in the defouling functions. This can be done by introduction of an additional random parameter which must be derived from statistical data processing of the underpinning experiments. Such an additional variable may improve the range of the scatter predicted as well as the prediction of the onset of erosion, which is a constant threshold at the

moment. This caused the failed SALT layer defouling prediction at low nominal air velocity and low target angle.

In conclusion, both models are considered to be valid for the prediction of axial aircraft compressor defouling simulations and this final application case has been recently addressed in Rudek *et al*. [16] and in more detail in Rudek [17]. The mean deviations encountered in the validation case study must be kept in mind when discussing results from application case simulations.

Four typical coatings which are relevant to commercial aircraft defouling processes were investigated in the framework of the new model development. It is possible to enlarge this statistical database to numerous coating and particle materials in the future using the basic experiment underpinning the model. Some additional experiments with dry-ice and water-ice particles in conjunction with various additional fouling materials are currently investigated at Hochschule Darmstadt by the authors. It is also planned to enlarge the model to further defouling effects such as thermal and chemical and this is currently addressed in another research project at Hochschule Darmstadt in collaboration with Lufthansa Technik.

## REFERENCES

[1] Ackert, S., Engine maintenance concepts for financiers. *Aircraft Monitor*, **2**, pp. 1–43, 2011.

[2] Kurz, R. & Brun, K., Fouling mechanisms in axial compressors. *Journal of Engineering for Gas Turbines and Power*, **134(3)**, pp. 1–9, 2012. https://doi.org/10.1115/1.4004403

[3] Meher-Homji, C.B. & Bromley, A., Gas turbine axial compressor fouling and washing.*Proceedings of tnhe 33rd Turbomachinery Symposium*, Vol. 1, pp. 163–192, 2004.

[4] Syverud, E., Brekke, O. & Bakken, L.E., Axial commpressor deterioration caused by saltwater ingestion. *Proceedings of GT2005—ASNME TurboExpo,* Reno-Tahoe, USA, Vol. 1, pp. 1–11, 2005.

[5] Meher-Homji, C.B., Compressor and hot section fouling in gas tunbines—causes and effects. *Proceedings from the 9th Annual Industrial Energy Technology Conference,* Houston, USA, Vol. 1, pp. 261–269, 1987.

[6] Meher-Homji, C.B., Chaker, M.A. & Motiwala, H.M., Gas turbine performance deterioration. *Proceedings of the 30th Turbomachinery Symposium*, College Station, USA, Vol. 1, pp. 139–175, 2001.

[7] Martn-Aragn, J. & Valds, M., A method to determine the economic cost of fouling of gas turbine compressors. *Applied Thermal Engineering*, **69(1–2)**, pp. 261–266, 2014.

[8] Diakunchak, I.S., Performance deterioration in industrial gas turbines. *International Gas Turbine and Aeroengine Congress and Exposition,* Orlando, USA, Vol. 4, pp. 1–8, 1991.

[9] Oosting, J., Boonstra, K., de Haan, A., van der Vecht, D., Stalder, J.P. & Eicher, U., On line compressor washing on large frame 9-fa gas turbines erosion on r0 compressor blade leading edge field performance with a novel on line wash system. *Proceedings of GT2007: ASME Turbo Expo,* Montreal, Canada, Vol. 1, pp. 1–10, 2007.

[10] Mund, F.C. & Pilidis, P., Gas turbine compressor washing: Historical developments, trends and main design parameters for online systems. *Journal of Engineering for Gas Turbines and Power*, **128(2)**, pp. 344–353, 2006. https://doi.org/10.1115/1.2132378

[11] Mund, F.C. & Pilidis, P., Online compressor washing: a numerical survey of influencing parameters. *Proceedings of the Institution of Mechanical Engineers—Journal of Power and Energy*, **219(1)**, pp. 13–23, 2005. https://doi.org/10.1243/095765005x6881

[12] Brun, K., Grimley, T.A., Foiles, W.C. & Kurz, R., Experimental evaluation of the effectiveness of online water-washing in gas turbine compressors. *Proceedings of the 42nd Turbomachinery Symposium*, Houston, USA, Vol. 1, pp. 1–18, 2013.

[13] Syverud, E. & Bakken, L.E., Online water wash tests of ge j85-13. *Proceedings of GT2005—ASME TurboExpo,* Reno-Tahoe, USA, Vol. 1, pp. 1–9, 2005.

[14] Giljohann, S., Brutigam, K., Kuhn, S., Annasiri, S. & Russ, G., Investigations into the on—wing cleaning of commercial jet engines with $co_2$ dry-ice blasting. *Deutscher Luft- und Raumfahrtkongress*, Vol. 1, pp. 1–9, 2012.

[15] Rudek, A., Zitzmann, T., Russ, G. & Duignan, B., An energy-based approach to assess and predict erosive airfoil defouling. *International Journal of Computational Methods and Experimental Measurements: Materials and Contact Characterization*, **6(3)**, pp. 476–486, 2018. https://doi.org/10.2495/cmem-v6-n3-476-486

[16] Rudek, A., Muckenhaupt, D., Kombeitz, R., Zitzmann, T., Russ, G. & Duignan, B., Experimental and numerical investigation of co2 dry-ice based aircraft compressor cleaning. *Proceedings of 13th European Conference on Turbomachinery Fluid Dynamics & Thermodynamics,* Lausanne, Switzerland, Vol. 13, pp. 1–16, 2019.

[17] Rudek, A., *Development and Validation of a Numerical Model of the CO2 Dry-ice Blasting Process for Aircraft Engine Cleaning Applications*. Ph.D. thesis, School of Mechanical and Design Engineering, Dublin Institute of Technology, 2018.

[18] Grant, G. & Tabakoff, W., Erosion prediction in turbomachinery resulting from environmental solid particles. *Journal of Aircraft*, **12(5)**, pp. 471–478, 1975. https://doi.org/10.2514/3.59826

[19] Sundararajan, G. & Shewmon, P.G., The oblique impact of a hard ball against ductile, semi-infinite target materials - experiment and analysis. *International Journal of Impact Engineering*, **6(1)**, pp. 3–22, 1987. https://doi.org/10.1016/0734-743x(87)90003-0

[20] Hutchings, I.M., Winter, R.E. & Field, J.E., Solid particle erosion of metals: the removal of surface material by spherical projectiles. *Proceedings of the Royal Society of London Series A, Mathematical and Physical Sciences*, **348(1654)**, pp. 379–392, 1976. https://doi.org/10.1098/rspa.1976.0044

[21] Hutchings, I.M., Macmillan, N.H. & Rickerby, D.G., Further studies of the oblique impact of a hard sphere against a ductile solid. *International Journal of Mechanical Sciences*, **23(11)**, pp. 639–646, 1981. https://doi.org/10.1016/0020-7403(81)90018-7

[22] Tirupataiah, Y. & Sundararajan, G., A dynamic indentation technique for the characterization of the high strain rate plastic flow behaviour of ductile metals and alloys. *Journal of Mechanics and Physics of Solids*, **39(2)**, pp. 243–271, 1991. https://doi.org/10.1016/0022-5096(91)90005-9

[23] Papini, M. & Spelt, J.K., Indentation-induced buckling of organic coatings part ii: measurements with impacting particles. *International Journal of Mechanical Sciences*, **40(10)**, pp. 1061–1068, 1998. https://doi.org/10.1016/s0020-7403(98)00018-6

[24] Kleis, I. & Hussainova, I., Investigation of particle—wall impact process. *Wear*, **233–235**, pp. 168–173, 1999. https://doi.org/10.1016/s0043-1648(99)00175-1

[25] Papini, M. & Spelt, J.K., Organic coating removal by particle impact. *Wear*, **213(1–2)**, pp. 185–199, 1997. https://doi.org/10.1016/s0043-1648(97)00062-8

[26] Papini, M. & Spelt, J.K., Indentation-induced buckling of organic coatings part i: theory and analysis. *International Journal of Mechanical Sciences*, **40(10)**, pp. 1043–1059, 1998. https://doi.org/10.1016/s0020-7403(97)00147-1

[27]  Gondret, P., Hallouin, E., Lance, M. & Petit, L., Experiments on the motion of a solid sphere toward a wall: from viscous dissipation to elastohydrodynamic bouncing. *Physics of Fluids*, **11(9)**, pp. 2803–2805, 1999. https://doi.org/10.1063/1.870109

[28]  Gondret, P., Lance, M. & Petit, L., Bouncing motion of spherical particles in fluids. *Physics of Fluids*, **14(2)**, pp. 643–652, 2002. https://doi.org/10.1063/1.1427920

[29]  Barnocky, G. & Davis, R.H., Elastohydrodynamic collision and rebound of spheres: experimental verification. *Physics of Fluids*, **31(6)**, pp. 1324–1329, 1988. https://doi.org/10.1063/1.866725

[30]  Davis, R.H., Rager, D.A. & Good, B.T., Elastohydrodynamic rebound of spheres from coated surfaces. *Journal of Fluid Mechanics*, **468**, pp. 107–119, 2002. https://doi.org/10.1017/s0022112002001489

[31]  Wall, S., John, W., Wang, H.C. & Goren, S.L., Measurements of kinetic energy loss for particles impacting surfaces. *Aerosol Science and Technology*, **12(4)**, pp. 926–946, 1990. https://doi.org/10.1080/02786829008959404

[32]  Djurovic, B., Jean, E., Papini, M., Tangestanian, P. & Spelt, J.K., Coating removal from fiber-composites and aluminum using starch media blasting. *Wear*, **224(1)**, pp. 22–37, 1999. https://doi.org/10.1016/s0043-1648(98)00308-1

[33]  Li, D.Y., Elalem, K., Anderson, M.J. & Chiovelli, S., A microscale dynamical model for wear simulation. *Wear*, **225–229**, pp. 380–386, 1999. https://doi.org/10.1016/s0043-1648(98)00368-8

[34]  Chen, Q. & Li, D.Y., Computer simulation of solid particle erosion. *Wear*, **254(3–4)**, pp. 203–210, 2003. https://doi.org/10.1016/s0043-1648(03)00006-1

[35]  Rudek, A., Russ, G. & Duignan, B., An experimental and numerical validation study of particle laden supersonic flows. *9th International Conference on Multiphase Flow*, Firenze, Italy, **9**, pp. 1–6, 2016.

[36]  Rudek, A., Russ, G. & Duignan, B., Particle laden flow investigations in special purpose dry- ice blasting applications. *Int International Journal of Computational Methods and Experimental Measurements: Advances in Fluid Mechanics*, **4(4)**, pp. 393–402, 2016.

# OIL/WATER FLOW IN A HORIZONTAL PIPE: DISPERSED FLOW REGIME

D. S. SANTOS[1], F. A. P. GARCIA[1], M. G. RASTEIRO[1] & P. M. FAIA[2]
[1] Chemical Process Engineering and Forest Products Research Centre (CIEPQPF), Department of Chemical Engineering, University of Coimbra, Portugal.
[2] Center of Mechanical Engineering, Materials and Processes (CEMMPRE), Electrical and Computers Engineering Department, University of Coimbra, Portugal.

## ABSTRACT

In multiphase fluid flow, the formation of dispersed patterns, where one of the phases is completely dispersed in the other (continuous medium) is common, for example, in crude oil extraction, during the transport of water/oil mixture.

In this work, experimental and numerical studies were carried out for the flow of an oil/water mixture in a horizontal pipe, the dispersed liquid being a paraffin (oil with density 843 kg m$^{-3}$ and viscosity 0.025 Pa s) and the continuous medium a water solution doped with NaCl (1000 μS. cm$^{-1}$). The tests were made for oil concentrations of 0.01, 0.13 and 0.22 v/v and velocities between 0.9 and 2.6 ms$^{-1}$ of the mixture. Experimental work was performed in a pilot rig equipped with an electrical impedance tomography (EIT) system. Information on pressure drop, EIT maps, volumetric concentrations in the vertical diameter of the pipe and flow images were obtained. Simulations were performed in 2-dimensional geometry using the Eulerian–Eulerian approach and the $k$-ε model for turbulence modelling. The model was implemented in a computational fluid dynamics platform with the programme COMSOL Multiphysics version 5.3. The simulations were carried out using the Schiller–Neumann correlation for the drag coefficient and two equations for the viscosity calculation: Guth and Simba (1936) and Pal (2000). For the validation of the simulations, the pressure drop was the main control parameter.

The simulations predicted the fully dispersed flow patterns and the pressure drop calculated when using the Pal (2000) equation for the viscosity calculation showed the best fit. The results of the images of the flows obtained by the photographs and simulations were in good agreement.
*Keywords: dispersed flow pattern, Euler–Euler model, oil/water flows, pressure drop.*

## 1 INTRODUCTION

Multiphase flows in pipe occur in many industrial sectors and are most important in the petroleum industry. In petroleum extraction and production processes, oil transport occurs along with other materials (water, air and solid particles) [1]. Thus, depending on the materials transported, the flow can be biphasic (oil/water, water/air, air/solids, etc.), three-phase (air/water/solid, air/oil/solid, etc.) or multiphasic (more than three phases) [1–4]. The interaction between the fluids, when transported, leads to the formation of flow patterns, being the main ones classified as dispersed, stratified and intermittent [5]. In addition, the long distances that the fluids travel until reaching their destination demand very high energy costs [6]. Studies have been developed in the search for optimization and creation of fluid pumping systems that lead to the reduction of energy consumption. In the literature, experimental studies have been carried out to characterize the different types of flow [2], the presence of the waves at the interface [7, 8], the transition between flow patterns [9], among others. These studies involve filming of the flow, sampling techniques [5] and non-invasive techniques, such as some tomographic techniques. In the latter case, these techniques obtain information about the system through measurement of the electromagnetic, acoustic or electrical properties of the fluids [10–15]. In addition to the experimental studies, flow simulations have also been extensively developed. Numerical simulations have been performed using methods based on the solution of the transport equations for the fluids through the direct simulation of local and

instantaneous equations, such as level-set method [16–18], phase-field method [19, 20] or volume of fluids method [20, 21], or through the solution of the average equations. In the latter case, the systems can be modelled using a homogeneous model, where the phases are treated as pseudofluids with average properties, and in this approach, the flow pattern is treated in a less detailed way [22], through a Lagrangian–Eulerian approach, where one of the phases is treated from an Eulerian perspective (as in the single phase flow) and the other phase receives a Lagrangian treatment [23, 24], or using an Eulerian–Eulerian approach, where each phase is treated continuously and the coupling between the phases occurs through interfacial terms [25–27].

In this work, a numerical simulation study was developed to describe the dispersed oil/water flow in a horizontal pipe (length of 11.5 m and an internal diameter of 0.11 m) and another experimental study to validate the simulations. For the simulation, a Eulerian–Eulerian approach was used in conjunction with the Reynolds-averaged Navier–Stokes (RANS) equations and the $k$-$\varepsilon$ turbulence model implemented in COMSOL Multiphysics 5.3. In the experimental study, electrical impedance tomography (EIT) was used to identify the flow pattern and to determine the distribution of the phases within the pipe. Simulation validation was performed by comparing the pressure drop data.

## 2 EXPERIMENTAL SETUP

The experimental tests for the oil/water dispersed flow were performed in a pilot plant rig (see Fig. 1).

The test fluids were liquid paraffin (density of 843±1 kg m$^{-3}$ and viscosity of 0.025±0.0002 Pa s) and water saline solution doped with NaCl (to allow a higher contrast between the phases in the EIT images), the interfacial tension is 46.0±0.1 mN m. The tests were performed for mixtures with oil concentrations of 0.01, 0.13 and 0.22 v/v and velocities between 0.9 and 2.6 m s$^{-1}$, in a straight section of the rig with length of 11.5 m and internal diameter of 0.11 m. The experiments were carried out at constant temperature. Data on



1 – Oil/water tank;
2 – Butterfly valve;
3 – Differential pressure transducer;
4 – Mixture Injection pump;
5 – Pt 100 temperature probe ;
6 – Mixture flowmeter;

7 – Sampling probe;
8 – Acrylic box;
9 – EIT Electrode ring;
10 – EIT aquisition system;
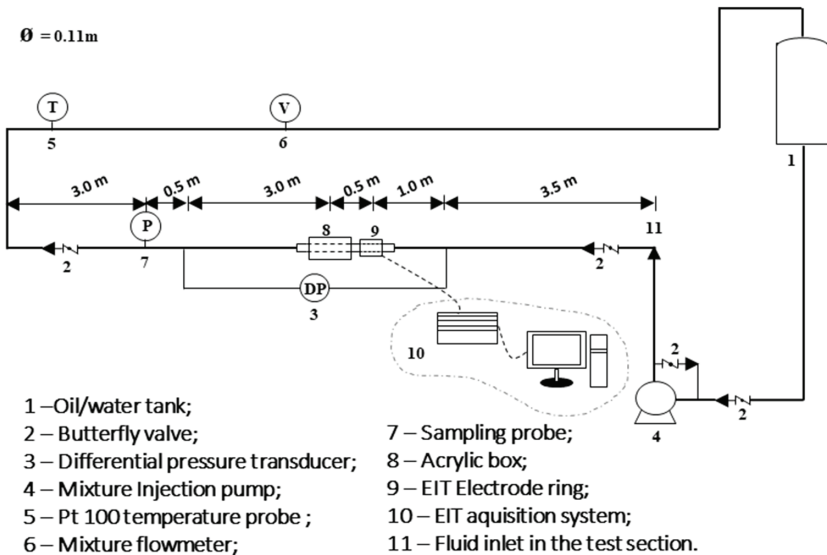11 – Fluid inlet in the test section.

Figure 1: Scheme of the closed-loop pipeline.

pressure drop, flow rate, temperature, samples of the mixture along the vertical radius of the pipe and crude data of the EIT were collected.

For the EIT system, a ring with 32 titanium electrodes, 5 mm in diameter, circumferentially and equally spaced, inserted in the acrylic tube, was used (a more comprehensive description can be found in [13, 28]). Tests were done with an excitation frequency of 60 kHz, with 2 V peak-to-peak amplitude, and acquiring 1000 frames per second. In this manuscript, the opposite injection and measuring protocols were used. For the reconstruction of the images, the open software EIDORS was used off-line [29].

## 3  MATHEMATICAL MODEL DESCRIPTION

In this work a Euler–Euler strategy was considered. Assuming that there is no mass transfer and that both phases are incompressible, the continuity equations for the continuous phase, eqn (1), and dispersed, eqn (2), are

$$\frac{\partial(\rho_c a_c)}{\partial t} + \nabla.(\rho_c a_c u_c) = 0 \tag{1}$$

$$\frac{\partial(\rho_d a_d)}{\partial t} + \nabla.(\rho_d a_d u_d) = 0 \tag{2}$$

The volume fractions are assumed to be continuous functions and their sum is equal to one $a_c = 1 - a_d$, where $\rho$ is the density, $a$ is the volumetric fraction, $t$ is the time, $u$ is the velocity and the subscripts $c$ and $d$ correspond, respectively, to the continuous and the dispersed phases.

The equations for the momentum balance for the continuous phase, eqn (3), and dispersed, eqn (4), are presented below [17]:

$$\rho_c a_c \left[ \frac{\partial}{\partial t}(u_c) + u_c \nabla.(u_c) \right] = -a_c \nabla P + \nabla.(a_c \tau_c) + a_c \rho_c g + F_{m,c} \tag{3}$$

$$\rho_d a_d \left[ \frac{\partial}{\partial t}(u_d) + u_d \nabla.(u_d) \right] = -a_d \nabla P + \nabla.(a_d \tau_d) + a_d \rho_d g + F_{m,d} \tag{4}$$

where $F_m$. is the term for the interfacial momentum transfer, $P$ is the pressure, $g$ is gravity and $\tau$ is the viscous stress tensor.

In this model, the fluid phases are considered Newtonian in both equations and the viscous tensors for each phase can be written as

$$\tau_c = \mu_c \left( \nabla u_c + (\nabla u_c)^T - \frac{2}{3}(\nabla.u_c)^I \right) \tag{5}$$

$$\tau_d = \mu_c \left( \nabla u_d + (\nabla u_d)^T - \frac{2}{3}(\nabla.u_d)^I \right) \tag{6}$$

In this work, two viscosity models were used to predict thrheological behaviour of dispersed system:

Guth and Simba (1936) model—this model considers the interaction between droplets and can be used for a wider range of dispersed phase concentrations [30, 31].

$$n_r = 1 + 2.5a_d + 14.1a_d^{~2} \tag{7}$$

where $n_r$ is the relative viscosity given by

$$n_r = \frac{\mu}{\mu_d} \tag{8}$$

Pal (2000) model—proposes an empirical equation based on experimental data for the viscosity of different emulsion systems, covering a wide range of the viscosity ratio between dispersed phase and continuous phase, $4.1 \times 10^{-3}$ to $1.17 \times 10^3$ [32]:

$$n_r^{-2.5} \left[ \frac{2n_r + 5b}{2 + 5b} \right]^{-2.5} = 1 - b_0 a_d \tag{9}$$

where $b$ is the viscosity ratio between the continuous and the dispersed phases. Regarding $b_0$, if no experimental data is available, the parameter becomes equal to 1.35.

The drag force for the dispersed flow can be defined as

$$F_{drag,c} = F_{drag,d} = \beta u_s \tag{10}$$

$$\beta = \frac{3a_d \rho_c C_d}{4 \varnothing_d} |u_s| \tag{11}$$

where $F_{drag,c}$ is the drag force for the continuous phase, $F_{drag,d}$ the drag force for the dispersed phase, $\beta$ is the sliding force coefficient, $\varnothing_d$ is the droplet diameter, $C_d$ is the drag coefficient for the diluted flow and $u_s$ is the slip velocity between phases and is given by

$$u_s = u_d - u_c \tag{12}$$

The drag coefficient was calculated by the Schiller–Neumann correlation [33]:

$$C_D = \begin{cases} \dfrac{24}{Re_p} \left( 1 + 0.15 Re_p^{0.687} \right) Re_p < 1000 \\ \\ 0.44 \; Re_p > 1000 \end{cases} \tag{13}$$

where $Re_p$ is the Reynolds of the particle and can be defined as

$$Re_p = \frac{\varnothing_d \rho_c |u_s|}{\mu_c} \tag{14}$$

Turbulence model
In this work, the RANS method was used to model turbulent flows. So, in this approach all time-dependent functions are expressed as the sum of a temporal mean and a floating component. The closing equation for the turbulent viscosity is given by [27]

$$\mu_T = \rho C_\mu \frac{k^2}{\varepsilon} \tag{15}$$

where $C_\mu$ is an experimentally obtained constant.

## 4  RESULTS AND DISCUSSION

For the simulations, the following hypotheses were applied: steady state, turbulent flow, incompressible, isothermal and without mass transfer between phases. The following input values were required: the tube wall roughness ($10^{-4}$ m), the fluid inlet velocities, the volumetric oil concentration, the fluid properties and the droplet diameter (120 μm). The boundary conditions used for the simulations were the velocities of the mixture at the inlet, zero pressure at the outlet and no slip at the wall.

### 4.1  Geometry and mesh

The geometry and meshes were implemented using the COMSOL Multiphysics® program. Mesh independency studies were conducted for a volumetric oil concentration of 0.01 and velocity of the mixture of 0.9 ms$^{-1}$. The best mesh (pressure drop independent of further refinement) corresponded to 91371 elements. So, the number of elements of the mesh used in the simulations for a 2D geometry was 91371.

In this study, the simulations compare the results of the tests obtained using two different equations for the viscosity calculation: Guth and Simba (1936) and Pal (2000).

### 4.2  Pressure drop

In Fig. 2, graphs of pressure drop versus velocity of the mixture for the oil concentrations of 0.01, 0.13 and 0.22 v/v and for simulations performed using the equations of Guth and Simba (1936) (a) and Pal (2000) (b), for the calculation of viscosity are presented.

It is observed that for the lower velocities of the mixture, the two equations presented close values, similar to the experimental ones. However, the increase in velocity led the Guth and Simba equation (1936) to obtain values of pressure drop that are further away from the experimental ones, what was not observed for the equation of Pal (2000). In Tables 1–3, we find the experimental and simulated pressure drop values. Pressure drop was obtained for volumetric concentrations of 0.01 (Table 1), 0.13 (Table 2) and 0.22 (Table 3), and for mixing velocities between 0.9 and 2.6 m s$^{-1}$. The results show that the viscosity equation for the mixture has relevant influence on the values of pressure drop.
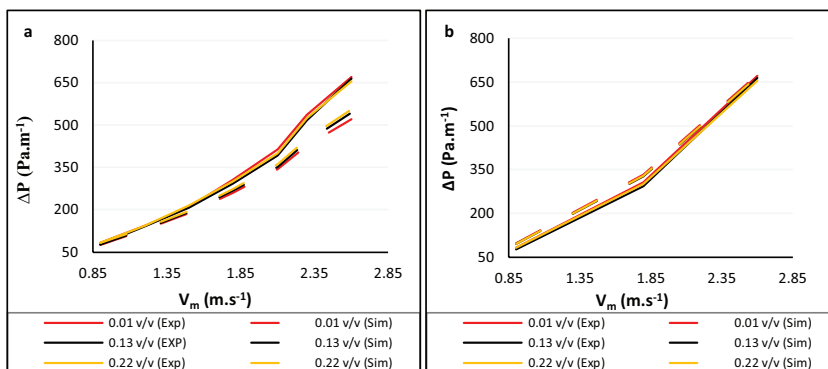


Figure 2: Pressure drop versus velocity of the mixture. Viscosity calculated by (a) the Guth and Simba (1936) equation and (b) the Pal (2000) equation.

Table 1: Experimental and simulated pressure drop values ($\Delta P$) for oil/water dispersed flow. For the simulations, the viscosity is calculated by the Guth and Simba (1936) and Pal (2000) equations. Oil concentration of 0.01 v/v.

| $V_m$ | $\Delta P_{Exp}$ | Schiller–Neumann | | | |
| | | Guth and Simba (1936) (Pa s) | | Pal (2000) (Pa s) | |
| (ms$^{-1}$) | (Pa m$^{-1}$) | $\Delta P_{Sim}$ (Pa m$^{-1}$) | Error (%) | $\Delta P_{Sim}$ (Pa m$^{-1}$) | Error (%) |
|---|---|---|---|---|---|
| 0.9 | 83.3 | 75.7 | 9.7 | 97.7 | 16.6 |
| 1.2 | 143.9 | 129.1 | 10.3 | - | - |
| 1.5 | 210.1 | 187.3 | 10.6 | - | - |
| 1.8 | 307.6 | 260.6 | 15.2 | 332.2 | 8.1 |
| 2.1 | 414.1 | 343.3 | 17.1 | - | - |
| 2.3 | 536.9 | 427.8 | 20.3 | - | - |
| 2.6 | 671.1 | 513.9 | 23.4 | 676.0 | 0.7 |

Table 2: Experimental and simulated pressure drop values ($\Delta P$) for oil/water dispersed flow. For the simulations, the viscosity is calculated by the Guth and Simba (1936) and Pal (2000) equations. Oil concentration of 0.13 v/v.

| $V_m$ | $\Delta P_{Exp}$ | Schiller-Neumann | | | |
| | | Guth and Simba (1936) (Pa s) | | Pal (2000) (Pa s) | |
| (ms$^{-1}$) | (Pa m$^{-1}$) | $\Delta P_{Sim}$ (Pa m$^{-1}$) | Error (%) | $\Delta P_{Sim}$ (Pa m$^{-1}$) | Error (%) |
|---|---|---|---|---|---|
| 0.9 | 77.3 | 77.7 | 0.5 | 97.0 | 25.4 |
| 1.2 | 141 | 132.3 | 6.2 | - | - |
| 1.5 | 206.8 | 192.5 | 6.9 | - | - |
| 1.8 | 293.2 | 267 | 8.9 | 328.0 | 11.8 |
| 2.1 | 393.2 | 352 | 10.4 | - | - |
| 2.3 | 516.3 | 441.3 | 14.5 | - | - |
| 2.6 | 664.5 | 543.8 | 18.1 | 670.1 | 0.8 |

Table 3: Experimental and simulated pressure drop values ($\Delta P$) for oil/water dispersed flow for the simulations, the viscosity is calculated by the Guth and Simba (1936) and Pal (2000) equations. Oil concentration of 0.22 v/v.

| $V_m$ | $\Delta P_{Exp}$ | Schiller–Neumann | | | |
| | | Guth and Simba (1936) (Pa s) | | Pal (2000) (Pa s) | |
| (m s$^{-1}$) | (Pa m$^{-1}$) | $\Delta P_{Sim}$ (Pa m$^{-1}$) | Error (%) | $\Delta P_{Sim}$ (Pa m$^{-1}$) | Error (%) |
|---|---|---|---|---|---|
| 0.9 | 83.6 | 83.8 | 0.2 | 97.0 | 16.0 |
| 1.2 | 142.7 | 135.5 | 5.3 | - | - |

| 1.5 | 214.5 | 196.5 | 8.4 | - | - |
| 1.8 | 301.6 | 273.1 | 9.4 | 328.5 | 8.9 |
| 2.1 | 400.8 | 360.4 | 10.1 | - | - |
| 2.3 | 523.9 | 451.4 | 13.8 | - | - |
| 2.6 | 654.6 | 556 | 15.1 | 670.1 | 2.4 |

### 4.3  Concentration profiles

In Figs. 3–5 the reconstructed images for oil concentrations of 0.01, 0.13 and 0.22 v/v, and mixture velocities of 0.9, 1.5, 2.1 and 2.6 ms$^{-1}$ are presented. For the representation of the variation of the normalized conductivity, a colour system was used, where the red and blue colours indicate the normalized conductivity values for the pure oil and aqueous phases, respectively, and the variation between both colours, corresponds to the mixtures between the two phases. The normalization is done using the reference measurements for the 1000 $\mu S$. cm$^{-1}$ NaCl solution without oil. $\eta$ is the normalized conductivity, $\sigma_m$ is the conductivity of the mixture and $\sigma_o$ is the reference conductivity:

$$\eta = \frac{\sigma_m - \sigma_o}{\sigma_0} \tag{16}$$

In the EIT images, it was not possible to distinguish the oil droplets because of their small size, but a homogeneous pattern was observed for all situations tested, confirming the existence of a dispersed flow pattern. However, as the oil concentration increased, the patterns
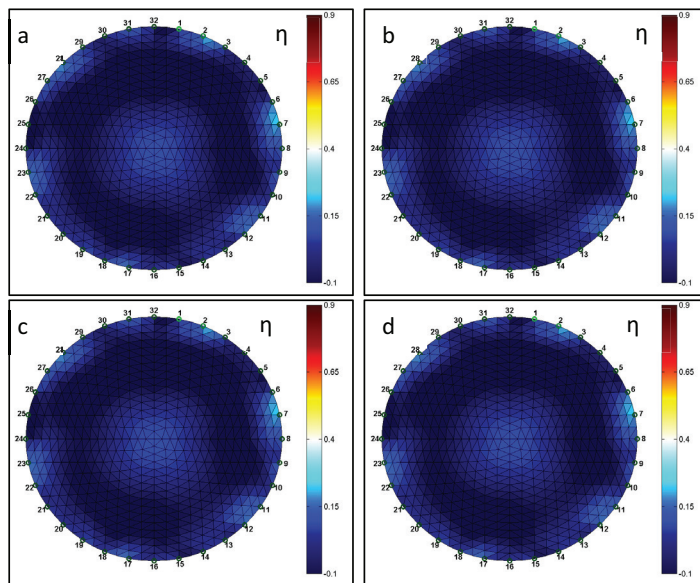


Figure 3: EIT images for oil/water dispersed flow. Oil concentration of 0.01 v/v and velocities of the mixture: (a) 0.9 ms$^{-1}$, (b) 1.5 ms$^{-1}$, (c) 2.1 ms$^{-1}$ and (d) 2.6 ms$^{-1}$.

Figure 4: EIT images for oil/water dispersed flow. Oil concentration of 0.13 v/v and velocities of the mixture (a) 0.9 ms$^{-1}$, (b) 1.5 ms$^{-1}$, (c) 2.1 ms$^{-1}$ and (d) 2.6 ms$^{-1}$.

became more heterogeneous (Figs. 4 and 5), with a higher predominance of the light blue colour (oil/water mixture) when the oil concentration increased.
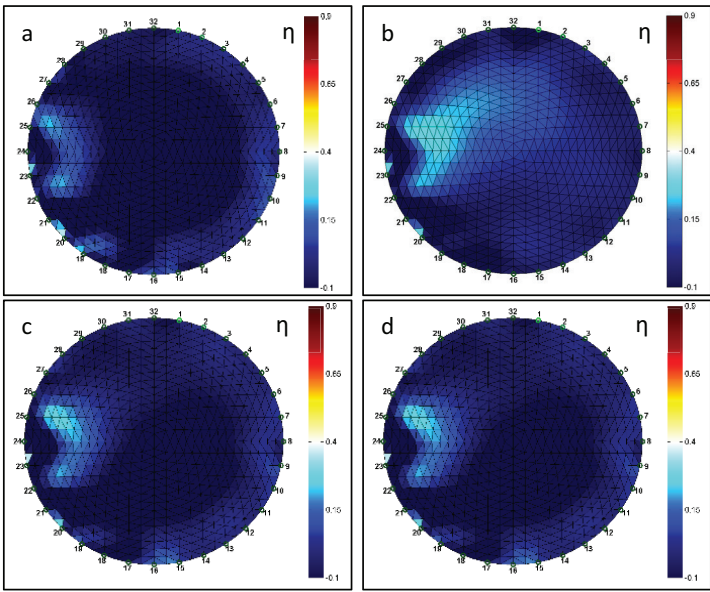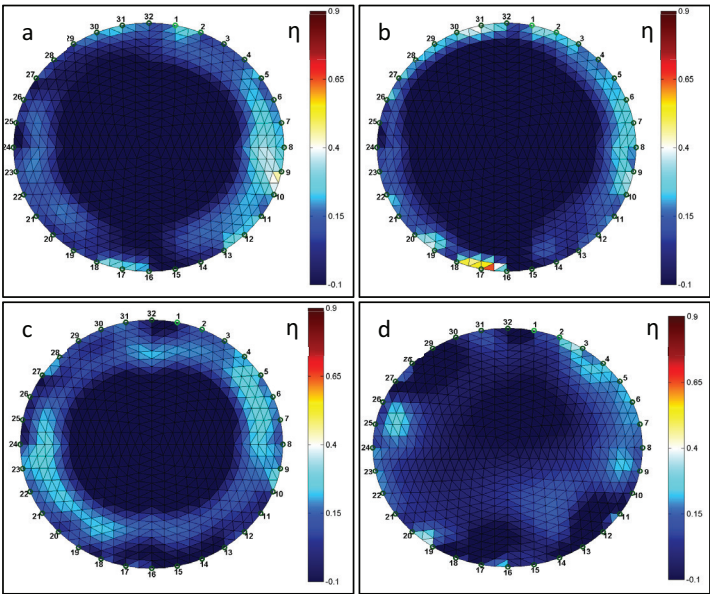


Figure 5: EIT images for oil/water dispersed flow. Oil concentration of 0.22 v/v and velocities of the mixture: (a) 0.9 ms$^{-1}$, (b) 1.5 ms$^{-1}$, (c) 2.1 ms$^{-1}$ and (d) 2.6 ms$^{-1}$.

Figure 6: Radial profile of the oil volumetric concentration (1D) for oil/
water dispersed flow. Velocity of the mixture of 0.9 m s$^{-1}$ and oil
concentration of (a) 0.01 v/v, (b) 0.13 v/v and (c) 0.22 v/v. In the
simulations, (S1) corresponds to the Guth and Simba (1936)
equation and (S2) to the Pal (2000) equation.

In Figs. 6 and 7, the volumetric oil concentration radial profiles (1D) obtained by the sampling/pycnometry and EIT and through the simulations are presented. Those profiles
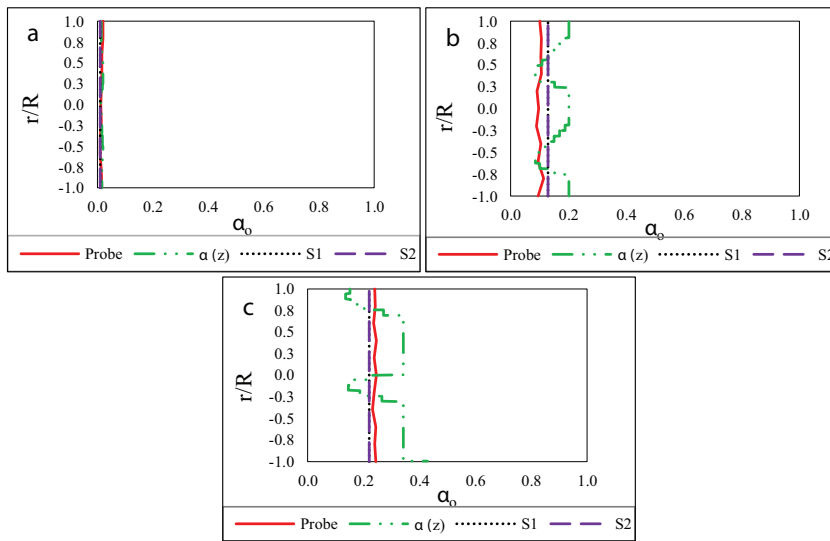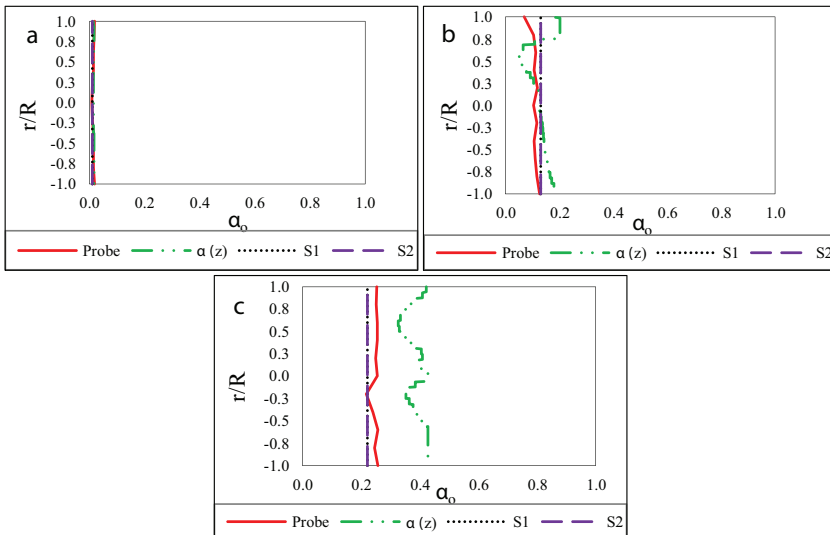


Figure 7: Radial profile of the oil volumetric concentration (1D) for oil/water dispersed
flow. Velocity of the mixture of 2.6 m s$^{-1}$ and oil concentration of (a) 0.01 v/v,
(b) 0.13 v/v and (c) 0.22 v/v. In the simulations, (S1) corresponds to the Guth
and Simba (1936) equation and (S2) to the Pal (2000) equation.

correspond to oil concentrations of 0.01, 0.13 and 0.22 v/v and to the velocities of the mixture of 0.9m s$^{-1}$ (Fig. 6) and 2.6 ms$^{-1}$ (Fig. 7). In the case of the EIT technique, the normalized conductivity profiles were converted to volumetric concentrations of the oil using a methodology that calculates the oil concentration ($\alpha(z)$) through the ratio of the volumetric concentration of the oil ($\alpha_0$) to a control area along the radius ($A_\sigma$) multiplied by the normalized conductivity ($\eta$) eqn (16) [13]:

$$\alpha(z) = \frac{\alpha_0}{A\sigma}\eta \tag{17}$$

The concentration profiles of the oil (EIT) show, for the oil concentration of 0.01 v/v, agreement with the profiles obtained through pycnometry. For the oil concentration of 0.13 v/v, the EIT profiles presented also reasonable agreement. Finally, for the oil concentration of 0.22 v/v, the concentration profiles presented overestimated results, comparing with the data obtained by the probe, for the highest velocity. As for the simulated profiles, (S1) corresponding to the Guth and Simba (1936) equation and (S2) to the Pal (2000) equation, the profiles are identical independently of the equation used, and were able to predict the experimental results satisfactorily.

## 5  CONCLUSIONS

In this work, the experimental tests were able to reproduce the dispersed flow pattern for three volumetric oil concentrations and for a range of velocities of the mixture, in a horizontal pipe, from 0.9 to 2.6 ms$^{-1}$, while using liquid paraffin to mimic the crude oil. The dispersed flow regime was confirmed using the EIT technique.

The best fit between the simulated and experimental values of pressure drop was obtained using the equation of Pal (2000) for the mixture viscosity and the Schiller–Neumann correlation for drag coefficient.

Regarding the 1D radial profiles, EIT agreed reasonably well with the data obtained through sampling/pycnometry, except for the highest concentration and velocity. In general, the 1D simulated oil concentration profiles agreed well with the experimental radial volumetric oil concentration profiles, obtained by sampling and pycnometry.

## REFERENCES

[1] Rodriguez, O.M.H., *Escoamento Multifásico*, ABCM—Associação Brasileira de Engenharia e Ciências Mecânica, Rio de Janeiro, Brasil, 2011.
[2] Trallero, J.L., Sarica, C. & Brill, J.P., A study of oil-water flow patterns in horizontal pipes. *SPE Production & Facilities*, **12**(**3**), pp. 165–172, 1997. https://doi.org/10.2118/36609-pa
[3] Tan, C., Wu, H. & Dong, F., Horizontal oil–water two-phase flow measurement with information fusion of conductance ring sensor and cone meter. *Flow Measurement and Instrumentation*, **34**, pp. 83–90, 2013. https://doi.org/10.1016/j.flowmeasinst.2013.08.006
[4] Grassi, B., Strazza, D. & Poesio, P., Experimental validation of theoretical models in two-phase high-viscosity ratio liquid–liquid flows in horizontal and slightly inclined

pipes. *International Journal of Multiphase Flow*, **34(10**), pp. 950–965, 2008. https://doi.org/10.1016/j.ijmultiphaseflow.2008.03.006

[5]  Wang, W., Gong, J. & Angeli, P., Investigation on heavy crude-water two phase flow and related flow characteristics. *International Journal of Multiphase Flow*, **37(9**), pp. 1156–1164, 2011. https://doi.org/10.1016/j.ijmultiphaseflow.2011.05.011

[6]  Rodriguez, O.M.H. & Baldani, L.S., Prediction of pressure gradient and holdup in wavy stratified liquid–liquid inclined pipe flow. *Journal of Petroleum Science and Engineering*, **96–97**, pp. 140–151, 2012. https://doi.org/10.1016/j.petrol.2012.09.007

[7]  Al-Wahaibi, T. & Angeli, P., Experimental study on interfacial waves in stratified horizontal oil–water flow. *International Journal of Multiphase Flow*, **37(8**), pp. 930–940, 2011. https://doi.org/10.1016/j.ijmultiphaseflow.2011.04.003

[8]  Rodriguez, O.M. & Castro, M.S., Interfacial-tension-force model for the wavy-stratified liquid–liquid flow pattern transition. *International Journal of Multiphase Flow*, **58**, pp. 114–126, 2014. https://doi.org/10.1016/j.ijmultiphaseflow.2013.09.003

[9]  Al-Wahaibi, T., Yusuf, N., Al-Wahaibi, Y. & Al-Ajmi, A., Experimental study on the transition between stratified and non-stratified horizontal oil–water flow. *International Journal of Multiphase Flow*, **38(1**), pp. 126–135, 2012. https://doi.org/10.1016/j.ijmultiphaseflow.2011.08.007

[10]  Wang, M., *Industrial Tomography: Systems and Applications*, Elsevier, MA. Boston, 2015.

[11]  Ismail, I., Gamio, J.C., Bukhari, S.A. & Yang, W.Q., Tomography for multi-phase flow measurement in the oil industry. *Flow Measurement and Instrumentation*, **16(2–3**), pp. 145–155, 2005. https://doi.org/10.1016/j.flowmeasinst.2005.02.017

[12]  Hasan, N.M. & Azzopardi, B.J., Imaging stratifying liquid–liquid flow by capacitance tomography. *Flow Measurement and Instrumentation*, **18(5–6**), pp. 241–246, 2007. https://doi.org/10.1016/j.flowmeasinst.2007.07.007

[13]  Silva, R., Garcia, F.A.P., Faia, P. M., Krochak, P., Söderberg, D., Lundell, F. & Rasteiro, M.G., Validating dilute settling suspensions numerical data through MRI, UVP and EIT measurements. *Flow Measurement and Instrumentation*, **50**, pp. 35–48, 2016. https://doi.org/10.1016/j.flowmeasinst.2016.06.003

[14]  Che, H.Q., Wu, M., Ye, J.M., Yang, W.Q. & Wang, H.G., Monitoring a lab-scale wurster type fluidized bed process by electrical capacitance tomography. *Flow Measurement and Instrumentation,* **62**, pp. 223–34, 2017. https://doi.org/10.1016/j.flowmeasinst.2017.09.005

[15]  Vauhkonen, M., *Electrical Impedance Tomography and Prior Information*, University of Kuopio, Kuopio, Finland, 1997.

[16]  Bilger, C., Aboukhedr, M., Vogiatzaki, K. & Cant, R.S., Evaluation of two-phase flow solvers using level set and volume of fluid methods. *Journal of Computational Physics*, **345**, pp. 665–686, 2017. https://doi.org/10.1016/j.jcp.2017.05.044

[17]  Yap, Y.F., Li, H.Y., Lou, J., Pan, L.S. & Shang, Z.,  Numerical modeling of three-phase flow with phase change using the level-set method. *International Journal of Heat and Mass Transfer*, **115**, pp. 730–740, 2017. https://doi.org/10.1016/j.ijheatmasstransfer.2017.08.076

[18]  Olsson, E. & Kreiss, G., A conservative level set method for two phase flow. *Journal of Computational Physics*, **210(1**), pp. 225–246, 2005. https://doi.org/10.1016/j.jcp.2005.04.007

[19]  Alam, J.M., A wavelet based numerical simulation technique for two-phase flows using the phase field method. *Computers & Fluids*, **146**, pp. 143–153, 2017. https://doi.org/10.1016/j.compfluid.2017.01.015

[20] Zhao, J., Wang, Q. & Yang, X., Numerical approximations to a new phase field model for two phase flows of complex fluids. *Computer Methods in Applied Mechanics and Engineering*, **310**, pp. 77–97, 2016. https://doi.org/10.1016/j.cma.2016.06.008

[21] Pozzetti, G. & Peters, B., A multiscale DEM-VOF method for the simulation of three-phase flows. *International Journal of Multiphase Flow*, **99**, pp. 186–204, 2018. https://doi.org/10.1016/j.ijmultiphaseflow.2017.10.008

[22] Arunkumar, S., Adhavan, J., Venkatesan, M., Das, S.K. & Balakrishnan, A.R., Two phase flow regime identification using infrared sensor and volume of fluids method. *Flow Measurement and Instrumentation*, **51**, pp. 49–54, 2016. https://doi.org/10.1016/j.flowmeasinst.2016.08.012

[23] Angeli, P. & Hewitt, G.F., Pressure gradient in horizontal liquid–liquid flows. *International Journal of Multiphase Flow*, **24**(**7**), pp. 1183–1203, 1999. https://doi.org/10.1016/s0301-9322(98)00006-8

[24] Schillings, J., Doche, O., Tano Retamales, M., Bauer, F., Deseure, J. & Tardu, S., Four-way coupled Eulerian–Lagrangian direct numerical simulations in a vertical laminar channel flow. *International Journal of Multiphase Flow*, **89**, pp. 92–107, 2017. https://doi.org/10.1016/j.ijmultiphaseflow.2016.10.006

[25] Sommerfeld, M., Van Wachem, B. & Oliemans, R. (eds), *Best Practice Guidelines for Computational Fluid Dynamics of Dispersed Multi-Phase Flows*, European Research Community on Flow, Turbulence and Combustion (ERCOFTAC), Brüssel.

[26] Kartushinsky, A., Tisler, S., Oliveira, J.L.G. & van der Geld, C.W.M., Eulerian-Eulerian modelling of particle-laden two-phase flow. *Powder Technology*, **301**, pp. 999–1007, 2016. https://doi.org/10.1016/j.powtec.2016.07.053

[27] Almohammed, N., Alobaid, F., Breuer, M., and Epple, B., A comparative study on the influence of the gas flow rate on the hydrodynamics of a gas–solid spouted fluidized bed using Euler–Euler and Euler–Lagrange/DEM models. *Powder Technology*, **264**, pp. 343–364, 2014. https://doi.org/10.1016/j.powtec.2014.05.024

[28] Faia, P.M., Silva, R., Rasteiro, M.G., Garcia, F.A.P., Ferreira, A.R., Santos, M.J., Santos, J.B. & Coimbra, A.P., Imaging particulate two-phase flow in liquid suspensions with electric impedance tomography. *Particulate Science and Technology*, **30**(**4**), pp. 329–342, 2012. https://doi.org/10.1080/02726351.2011.575444

[29] Polydorides, N. & Lionheart, W.R.B., A matlab toolkit for three-dimensional electrical impedance tomography: A contribution to the Electrical Impedance and Diffuse Optical Reconstruction Software project. *Measurement Science and Technology*, **13**(**12**), pp. 1871–1883, 2002, https://doi.org/10.1088/0957-0233/13/12/310

[30] Pouraria, H., Seo, J.K. & Paik, J.K., Numerical modelling of two-phase oil–water flow patterns in a subsea pipeline. *Ocean Engineering*, **115**, pp. 135–148, 2016, https://doi.org/10.1016/j.oceaneng.2016.02.007

[31] Walvekar, R.G., Choong, T.S., Hussain, S.A., Khalid, M. & Chuah, T.G., Numerical study of dispersed oil–water turbulent flow in horizontal tube. *Journal of Petroleum Science and Engineering*, **65**(**3–4**), pp. 123–128, 2009. https://doi.org/10.1016/j.petrol.2008.12.019

[32] Xu, X.X., Study on oil–water two-phase flow in horizontal pipelines. *Journal of Petroleum Science and Engineering*, **59**(**1**), pp. 43–58, 2007. https://doi.org/10.1016/j.petrol.2007.03.002

[33] Liu, Z. & Li, B., Scale-adaptive analysis of Euler-Euler large eddy simulation for laboratory scale dispersed bubbly flows. *Chemical Engineering Journal*, **338**, pp. 465–477, 2018. https://doi.org/10.1016/j.cej.2018.01.051

# FORMATION OF A FALLING PARTICLE CURTAIN

PETER VOROBIEFF[1], PATRICK WAYNE[1], SUMANTH REDDY LINGAMPALLY[1], GREGORY VIGIL[1],
JOSH LUDWIGSEN[1], DANIEL FREELONG[1], C. RANDALL TRUMAN[1] & GUSTAAF JACOBS[2]
[1] Department of Mechanical Engineering, The University of New Mexico, Albuquerque, USA.
[2] Department of Aerospace Engineering, San Diego State University, USA.

## ABSTRACT
Falling particle curtains are important in many engineering applications, including receivers for concentrating solar power facilities. During the formation of such a curtain, we observe a multiphase analog of Rayleigh–Taylor instability (RTI). It was originally described in 2011 for a situation when air sparsely seeded with glycol droplets was placed above a volume of unseeded air, producing an unstably stratified average density distribution that was characterized by an effective Atwood number 0.03. In that case, the evolution of the instability was indistinguishable from single-phase RTI with the same Atwood number, as the presence of the droplets largely acted as an additional contribution to the mean density of the gaseous medium. Here, we present experiments where the volume (and mass) fraction of the seeding particles in gas is considerably higher, and the gravity-driven flow is dominated by the particle movement. In this case, the evolution of the observed instability appears significantly different.
*Keywords: experiment, hydrodynamic instabilities, multiphase flow, Rayleigh–Taylor instability.*

## 1 INTRODUCTION
In classical hydrodynamics, several important instabilities can be described using the same idealized formulation [1]. Consider an inviscid, incompressible two-dimensional flow with a density interface in the $x - y$ plane near $y = 0$ separating fluids characterized by densities $\rho_1$ in the lower and $\rho_2$ in the upper half-plane. If the $y$-velocity is initially uniformly zero, and the uniform $x$-velocities $U_1$ (lower half-plane) and $U_2$ (upper half-plane) are not equal, the case of $\rho_1 = \rho_2$ will produce pure Kelvin–Kelmholtz instability (KHI). If both fluids are initially at rest, with $\rho_2 > \rho_1$, and are subject to constant acceleration $g$ directed down the $y$ axis, Rayleigh–Taylor instability (RTI) will develop, amplifying any interfacial perturbations. Finally, in the case when sustained acceleration is replaced with an impulsive acceleration (either in the positive or in the negative $y$-direction), Richtmyer–Meshkov instability (RMI) will manifest [2], [3]. KHI, RTI, and RMI play an important role in a wide variety of liquid, gas, and plasma flows and have been extensively studied. For RTI and RMI, the necessary condition for the instability is $\rho_1 \neq \rho_2$ on the interface. The dimensionless parameter essential for the characterization of both RMI and RTI is the Atwood number

$$A = \frac{\rho_2 - \rho_1}{\rho_2 + \rho_1} \tag{1}$$

Now consider multiphase flow where the embedding phase (gas or liquid) has a constant density, but the embedded phase (particles, droplets, etc.) is distributed non-uniformly, leading to the existence of gradients of average density. Recently, it was demonstrated [4]–[6] that analogues of RMI and RTI exist in such flows subjected either to gravity or to impulsive (shock) acceleration. The analogue of RMI [4] is known as shock-driven multiphase instability (SDMI) [6], [7]. As in the case of classical RMI, a dimensionless number similar to the Atwood number (eqn (1)) plays a key role in SDMI: the multiphase Atwood number [8]

$$A_m = \frac{\rho_s - \rho_u}{\rho_s + \rho_u} \qquad\qquad (2)$$

Here, the subscript $s$ characterizes the volume-averaged properties of the *seeded* flow (embedding phase together with embedded phase), and the subscript $u$ the properties of the *unseeded* embedding phase.

Two limit cases can be considered: $A_m \rightarrow 0$ and $A_m \rightarrow 1$. Presently, the former case is somewhat better studied [4], [8]–[10], with investigations mostly focusing on SDMI. For $A_m \rightarrow 0$, gaseous embedding phase, and liquid or solid embedded phase (small micron or submicron-sized droplets or particles), it was shown that the SDMI growth can be (at least in first order) approximated with expressions originally derived for RMI, replacing $A$ (eqn (1)) with $A_m$ (eqn. (2)) [4]. Likewise, in this case shock-accelerated multiphase flow can be modeled (credibly but not perfectly) with models developed for the single-phase variable-density case (RMI) [11]. Differences between SDMI and RMI are nevertheless considerable: while shock-induced RMI is baroclinically driven (vortex formation is precipitated by misalignment between density and pressure gradients), in SDMI, vortex formation is driven by shear (similar to KHI), while shear is produced by massive particles or droplets interacting with the surrounding shock-accelerated gas and slowing it down.

One earlier study was also conducted for the multiphase analogue of RTI [5] for $A_m \sim 0.03$. For the flow under investigation (air with a small volume fraction of micron-sized glycol droplets), it was concluded that morphologically and in terms of instability growth, the results were indistinguishable from classical single-phase RTI, with droplet seeding effectively contributing only to local average density.

But what happens for the other limit case $(A_m \rightarrow 1)$? For the studies summarized in the preceding paragraphs, the flow was dominated by hydrodynamic effects. As $A_m$ increases, particle interactions, particle inertia, etc. begin to play a more prominent role. In the following sections, we describe an experiment where a falling particle curtain forms with particle seeding density leading to $A_m \approx 0.98$. During the formation of this curtain, perturbations on its leading edge grow, similarly to what happens with an RTI-unstable interface. However, the growth rate appears very different from what is observed for classical RTI, and this can be explained by profound differences in the physics of the corresponding flows.

## 2  EXPERIMENTAL SETUP

The motivation for particle-curtain studies described here was twofold. First, we wanted to produce an average density interface characterized by a sufficiently high $A_m$ for studies of its evolution under shock acceleration. Second, we were conducting a study on a related subject, operation of a falling particle curtain receiver used to store heat produced by a concentrating solar power facility [12]. Both the formation and the steady-state condition of the curtain proved much more interesting than anticipated.

Figure 1 shows the schematic (top) and the actual view of the experimental arrangement. In the top view, the particle–curtain setup is shown mounted on the UNM shock tube, which is described in detail elsewhere [8]. The arrangement is comprised of a modular extruded-metal frame used to mount the components, the horizontal element of which is the hopper rail. To the hopper rail, we attach the particle hopper. At the bottom of the hopper, a sliding plate is placed to keep the particles in prior to the beginning of the experiment. The same element serves to mount an electric motor that provides a small-amplitude vibration to the hopper. These components are vibration-isolated from the rest of the setup, the latter
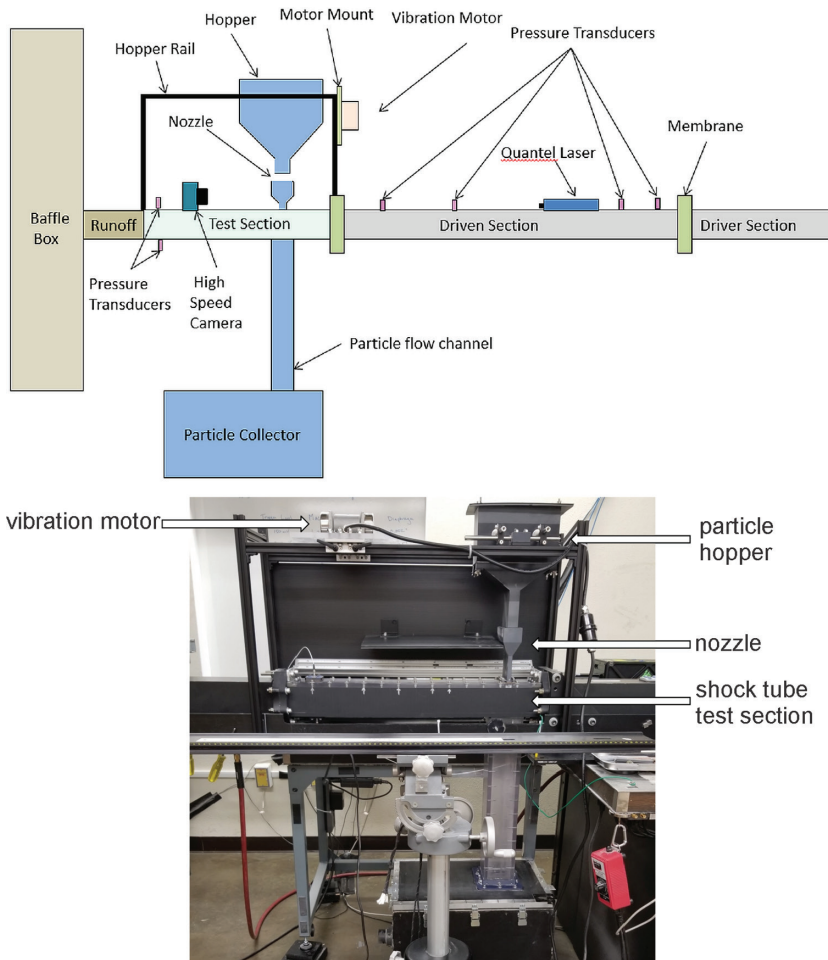
Figure 1: Top: schematic of the side view of the experimental
arrangement, including the UNM shock tube and the particle-
curtain setup. Bottom: close-up photo of the test section of
the shock tube, the hopper rail, and the particle-curtain setup.

including the particle curtain-forming nozzle attached directly to the test section of the shock tube. In the experiments described here, the horizontal dimensions of the nozzle opening were 72 × 2 mm.

In the experiments described below, a typical run proceeded as follows. The hopper (sliding plate closed) was loaded with soda lime particles. The nominal particle diameter ranged between 30 and 50 μm, and the particle density was 1.44 g/cc. Then the vibration motor was turned on, and the sliding plate removed from the bottom of the hopper, releasing the particles into the nozzle below, then into the test section, then into the particle flow channel, and into the particle collector, from which the particles could be extracted for reuse. For experiments with shocked curtain, the location of the camera visualizing the curtain must be chosen outside the shock tube, as shown in Fig. 1, top, however, in the data presented here, the runoff

section of the setup connecting the test section of the shock tube with the baffle box was removed, making it possible to visualize the falling curtain so that the optical axis of the camera lens was at 90° to the plane of the curtain.

A Sony RX IV camera was used to capture images at 960 frames per second in full HD resolution. The camera was turned on shortly prior to the opening of the sliding plate, with data acquisition runs limited to 2 s by hardware. The curtain was illuminated through the transparent sides of the test section with two LED panels.

## 3 OBSERVATIONS AND ANALYSIS

Figure 2 shows (in false color) a sequence of four cropped images tracking the leading edge of the falling curtain. It takes about 60 ms for the edge of the curtain to reach the bottom of the test section and disappear into the particle flow channel. It is important to note that the distance between the bottom of the hopper with the sliding plate and the point where the particle curtain becomes visible is about 12 cm, so the particles are entering the field of view of the camera some time (about 200 ms) after the sliding plate is opened, giving any interfacial perturbations some time to develop. Another important aspect of the observed flow evolution that must be mentioned is that the centerline of the curtain edge in the vertical direction moves downward and accelerates. This necessitates a deviation from the way interfacial perturbations are usually measured in classical RTI studies, where after gravity-driven instability growth commences, bubbles of lighter gas or fluid go up, and spikes of heavier gas or fluid go down, and local instability amplitude can be measured in a stationary reference frame, from top of bubble to bottom of adjacent spike. Here, we have to track the leading



$t = 0$    $t = 16.6$ ms
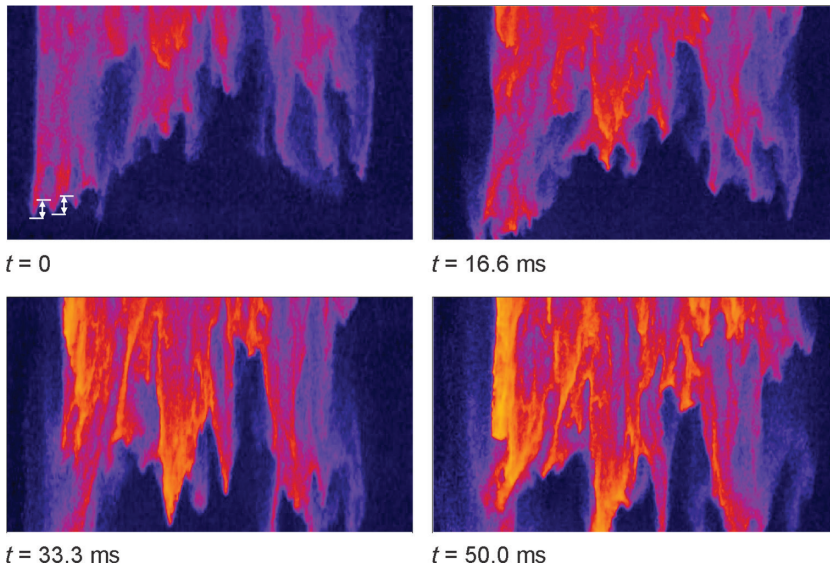
$t = 33.3$ ms    $t = 50.0$ ms

Figure 2: Four images (false-color) tracking the leading edge of the falling particle curtain. Time $t = 0$ corresponds to the moment the leading edge of the curtain clears the nozzle and becomes fully visible in the test section. The width of the field of view is 76 mm. Arrows in the first image show two examples of perturbation amplitude measurements.

edge of the curtain, and make the same measurements (perturbation amplitude bubble-to-spike) in a moving reference frame.

With these caveats, it is still apparent that the leading edge of the curtain is perturbed, and the perturbation is growing.

Three data sequences with identical initial conditions were acquired and analyzed to measure peak-to-peak amplitudes at seven timings, from 0 to 50 ms after the falling curtain enters the field of view of the camera. From each sequence, a single frame at seven timings (0, 8.3, 16.6, 24.9, 33.3, 41.6, and 50 ms) was analyzed, yielding up to 12 bubble-to-spike amplitude measurements. Figure 3 shows the analysis results. Both the images and the plot show considerable variance in the perturbation amplitude, but the overall trend in perturbation growth with time is quite close to linear: the coefficient of determination $r^2 = 0.97$ for the fit shown in the plot.

Additional characterization of the curtain in terms of velocity field and mass flow rate was also undertaken [13]. The mass flow rate was measured directly, by monitoring the initial and transient weight of the particle collector (44.16, 0.12 g/s). Velocity-field measurements of a curtain that reached steady-state [14] reveal that the average vertical velocity grows linearly with downstream distance (and thus with time). With the known average velocity and mass flow rate, the volume fraction of the particles can also be found from simple conservation-of-mass considerations. For the steady-state curtain, it varied from 8.4% at the top of the test section to 2.5% at the bottom. In terms of the multiphase Atwood number (eqn (2)), this translates to $0.98 > A_m > 0.95$. The curtain is indeed in the $A_m \rightarrow 1$ regime.
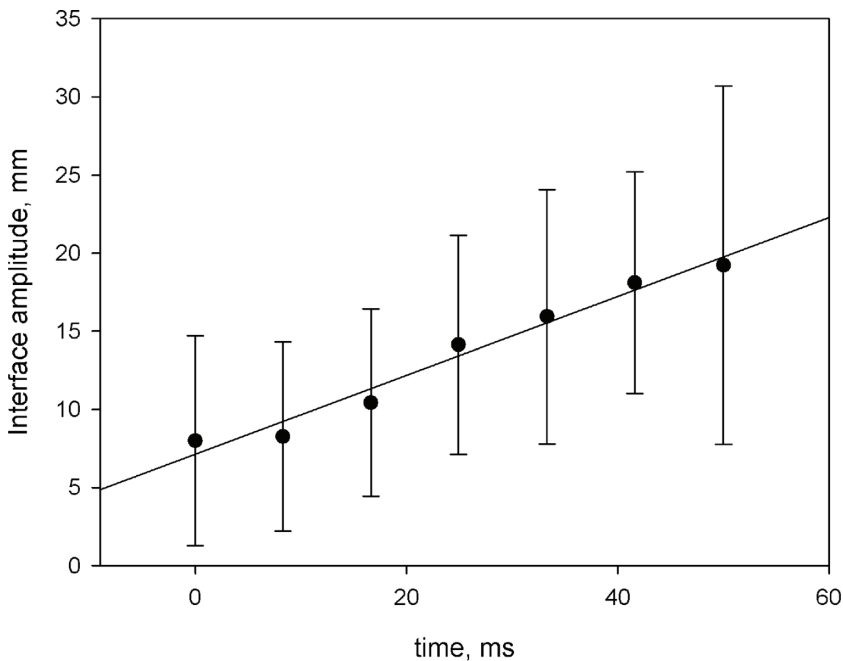


Figure 3: Time history of the perturbation amplitude on the leading edge of the falling curtain. Error bars show the standard deviation at each timing. Straight line: linear fit.

What can account for the stark difference between the interfacial perturbation evolution in classical RTI (quadratic) and what we observe for the falling particle curtain? Two explanations are possible. One possibility is that the observation window used in our experiment is insufficient to track the quadratic growth. The other possibility is that the growth is both dominated by physics somewhat different from the classical RTI and observed in a different (accelerating) reference frame. Based on both mass-conservation considerations and direct measurements [13], as the curtain accelerates downward, its local particle seeding concentration decreases, leading to a small but noticeable and highly repeatable decrease in $A_m$. Now consider the classical quadratic-growth instability amplitude $h$ growth formula for RTI
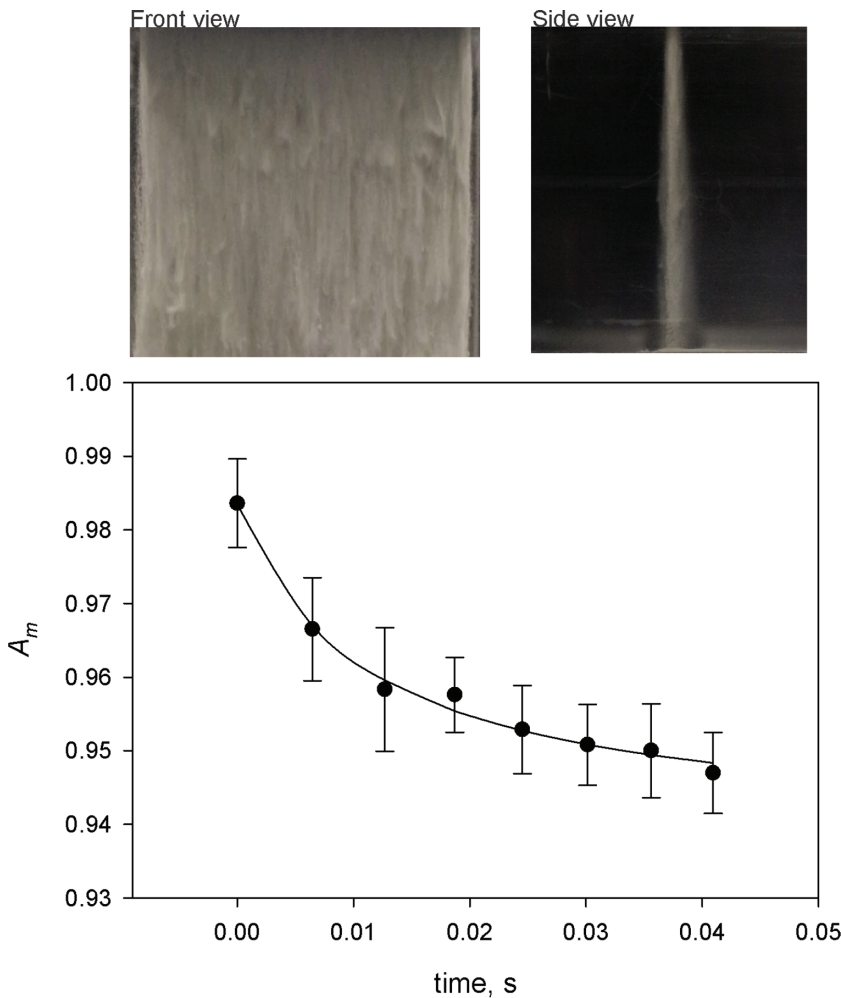


Figure 4: Top: front and side images of the falling curtain showing the entire field of view, top to bottom. Bottom: Multiphase Atwood number in the curtain as a function of time. Time $t = 0$ corresponds to the moment when the flow enters the field of view at the top of the test section. The line is the best fit to the data using eqn (3) with parameters described in the text.

$$h = \alpha A g t^2$$

where $\alpha$ is a constant (on the order of 0.05). Now let us replace $A$ with $A_m$ slowly (at a rate $\varepsilon$) decreasing in time to an equilibrium terminal-velocity value $A_{m,t.v.}$, with a time offset $t_e$ (time to account for curtain development as it leaves the nozzle)

$$A_m = \frac{\varepsilon}{t + t_\mu} + A_{m,t.v.} \tag{3}$$

Then let us transition into a reference frame accelerating at a rate

$$h_{m,t.v.} = \alpha A_{m,t.v.} g t^2$$

This reference frame to first order will correspond to the frame following the falling-curtain edge, and the perturbation growth in that frame will be

$$\delta h = a \frac{\varepsilon}{t + t_e} g t^2$$

For sufficiently late $t$, $t \gg t_e$, and $\delta h \sim t$, manifesting linear growth.

For a more realistic consideration, local particle seeding density variability, leading to local fluctuations of $A_m$, should be taken into account, as it likely produces the velocity differences along the edge of the falling curtain. The relevant physics at $A_m \to 1$ are dominated by particle inertia, unlike $A_m \to 0$ or classical RTI. For $A_m \to 1$, the baroclinic vorticity production mechanism in fluid (vorticity generation proportional to the cross-product of density and pressure gradients) is less relevant, and the most likely key hydrodynamic characteristic is the local terminal velocity of a particle-seeded volume, which would vary with $A_m$.

Figure 4 shows front and side snapshots of the curtain over the entire 7.6 cm vertical extent of the test section, and the plot of the time evolution of $A_m$ based on the data collected earlier [13], [14] for the average velocity and mass-discharge rate of a curtain that achieved a steady state. The fit to the data uses eqn (3), with the parameters as follows: $\varepsilon = 4.9 \times 10^{-4}$, $t_e = 0.011$, $A_{m,t.v.} = 0.939$, time in s. The coefficient of determination for this best fit is $r^2 = 0.991$. Note that these values are largely consistent with the assumptions we made above regarding the order of magnitude of the parameters: $\varepsilon \ll 1$, $t_e \ll t$, and $A_{m,t.v.} \sim 1$.

## 4 CONCLUSIONS

Similar to SDMI, a multiphase gravity-driven instability (MGDI) also appears to exist. As SDMI can be regarded as a multiphase analogue of RMI, so the MGDI corresponds to RTI. Two limit cases exist for MGDI. In terms of multiphase Atwood number $A_m$, the first limit case is $A_m \ll 1$. For this case, behavior similar to RTI was observed, with flow dominated by hydrodynamic effects, and the embedded phase following the flow. We show the second case, $A_m \to 1$, to manifest behaviors distinct from RTI. The $A_m \to 1$ flow is likely to be dominated by particle effects, although fluid mechanics still must play a role. We observe linear growth of perturbations along the leading edge of the curtain and offer a simple explanation based on the flow phenomenology and theory for the linear trend, which is distinct from quadratic growth for classical RTI and consistent with earlier experiment.

Future studies are required to elucidate some features observed in the $A_m \to 1$ falling-curtain flow. Flow visualization shows persistent formation of perturbations with features at similar wavelengths (Fig. 2). The wavelength selection mechanism is presently unclear. A longer observation interval will help determine how long the linear perturbation amplitude growth

persists. It would also be very instructive to study the same falling-curtain formation in vacuum, to determine the actual contribution of hydrodynamic effects. The parameter range for $A_m$ should also be extended through the entirety of the possible values ($0 < A_m < 1$): now we know something about the limit cases (very high and very low values), but a very important special case remains to be studied: flow with both gaseous density gradients ($A \neq 0$) and seeding ($A_m \neq 0$) where neither feature is clearly dominant.

We also seek to understand growth rates by conducting numerical analysis using an approach similar to the Eulerian–Lagrangian study of the particle-laden RMI [6].

## REFERENCES

[1] Currie, I.G., *Fundamental Mechanics of Fluids*, CRC Press; 2002.

[2] Richtmyer, R.D., Taylor instability in shock acceleration of compressible fluids. *Communications on Pure and Applied Mathematics*, **13(2)**, pp. 297–319, May 1960. https://doi.org/10.1002/cpa.3160130207

[3] Meshkov, E.E., Instability of the interface of two gases accelerated by a shock wave. *Fluid Dynamics*, **4(5)**, pp. 101–104, 1 September 1972. https://doi.org/10.1007/bf01015969

[4] Vorobieff, P., Anderson, M., Conroy, J., White, R., Truman, C.R. & Kumar, S., Vortex formation in a shock-accelerated gas induced by particle seeding. *Physical Review Letters*, **106(18)**, p. 184503, 4 May 2011. https://doi.org/10.1103/physrevlett.106.184503

[5] Vorobieff, P., Anderson, M., Conroy, J., White, R., Truman, C.R. & Kumar, S., Analogues of Rayleigh-Taylor and Richtmyer-Meshkov instabilities in flows with nonuniform particle and droplet seeding. *WIT Transactions on Engineering Sciences*, pp. 17–28, 27 May 2011. https://doi.org/10.2495/mpf110021

[6] Gonzalez Izard, R., Lingampally, S.R., Wayne, P., Jacobs, G. & Vorobieff, P., Instabilities in a shock interaction with a perturbed curtain of particles. *International Journal of Computational Methods and Experimental Measurements*, **6(1)**, pp. 59–70, 2017. https://doi.org/10.2495/cmem-v6-n1-59-70

[7] Frost, D.L., Heterogeneous/particle-laden blast waves. *Shock Waves*, **28(3)**, pp. 439–449, May 2018. https://doi.org/10.1007/s00193-018-0825-1

[8] Anderson, M., Vorobieff, P., Truman, C.R., Corbin, C., Kuehner, G., Wayne, P., Conroy, J., White, R. & Kumar, S., An experimental and numerical study of shock interaction with a gas column seeded with droplets. *Shock Waves*, **25(2)**, pp. 107–125, 2015. https://doi.org/10.1007/s00193-015-0555-6

[9] McFarland, J.A., Black, W.J., Dahal, J. & Morgan, B.E., Computational study of the shock driven instability of a multiphase particle-gas system. *Physics of Fluids*, **28(2)**, p. 024105, 2016. https://doi.org/10.1063/1.4941131

[10] Black, W.J., Denissen, N.A. & McFarland, J.A., Evaporation effects in shock-driven multiphase instabilities. *Journal of Fluids Engineering*, **139(7)**, p. 071204, 2017.

[11] Anderson, M., Vorobieff, P., Kumar, S., Conroy, J., White, R., Needham, C. & Truman, C.R., Numerical simulation of a shock-accelerated multiphase fluid interface. *In 28th International Symposium on Shock Waves*, Springer, Berlin, Heidelberg, pp. 923–929, 2012.

[12] Ho, C.K., Kinahan, S., Ortega, J.D., Vorobieff, P., Mammoli, A. & Martins, V., Characterization of particle and heat losses from falling particle receivers. *In Proceedings of the ASME 2019 13th International Conference on Energy Sustainability*, pp. 1–10.

[13] Freelong, D., Reflections of a shock wave off a sparse curtain of particles. *Presented at* 2019 *AIAA Region IV Student Conference*, pp. 29–31, March 2019.

[14] Vigil, G., Vorobieff, P., Freelong, D., Wayne, P. & Truman, C.R., Validating advection-corrected correlation image velocimetry. *Bulletin of the American Physical Society*, **63(13)**, p. 613, 2018.

[15] Asay-Davis, X.S., Marcus, P.S., Wong, M.H. & de Pater, I., Changes in Jupiters zonal velocity between 1979 and 2008. *Icarus*, **211(2)**, pp. 1215–1232, 2011. https://doi.org/10.1016/j.icarus.2010.11.018

*This page intentionally left blank*

# ADJUSTMENT OF REACTOR MODEL IN ORGANIC MATTER REMOVAL FROM WASTEWATER APPLYING NUMERICAL RESIDENCE TIME DISTRIBUTION ANALYSIS

TAMAS KARCHES

Institute of Water Supply and Environmental Engineering, National University of Public Service, Hungary.

## ABSTRACT

Mass balance models in wastewater treatment may overpredict the organic matter degradation in aerated basins, because the simulation tools apply simplified reactor models, which could not represent the actual hydrodynamic and mixing conditions in the reactors. Ineffective reactor zones, short hydraulic circuits could have an effect on the actual performance of treatment process. In this paper, a wastewater treatment plant with a capacity of 10 MLD was investigated, where residence time distribution (RTD) analysis performed with computational fluid dynamics tools determined the actual time for biodegradation, and the biokinetic model could be updated. For the numerical RTD analysis 3D transient multiphase flow with turbulence closure was applied, whereas mass balance modelling used GPS-X simulation tool calibrated by field data. The model results were in good agreement with the measured chemical oxygen demand, total suspended solid values in treated effluent, and this method highlighted the importance of extension of mass balance modelling with hydrodynamic calculations.
*Keywords: mass balance modelling, organic matter, reactor models, wastewater treatment.*

## 1 INTRODUCTION

The majority (90%) of water supply in Hungary is based on subsurface water sources. In order to protect these resources, used water shall undergo a treatment process before releasing it to receiving water bodies. Medium or large size municipalities apply centralized solution with large channel systems, which collect and transport the wastewater to treatment plants, where biodegradation processes reduce the organic matter and nutrient content of wastewater. Nowadays decentralized solutions are again in focus in Hungary aiming to treat the wastewater locally [1], where it is produced by applying the same biochemical processes as in large scale plants.

Wastewater treatment is a combination of various processes which could be separated into mechanical, biological, chemical and post-treatment stages. The mechanical stage applies screens, grit chamber, in some cases primary sedimentation tanks, the biological stage equips various environments (e.g. anoxic, aerobic, etc.) for microorganisms each responsible for different processes (e.g. nitrification, denitrification, enhanced biological removal, etc). Chemical treatment is basically responsible for phosphorous removal and enhance the phase separation [2]. The 4th stage of wastewater treatment is applied for removal of micro pollutants or polishing the effluent in order to close the urban water cycle.

Wastewater treatment modelling is a complex system with numerous sub-models which are interconnected. Each element has its own significance and purpose. The International Water Association Good Modelling Practice Task Group developed a model structure, its key parts were the mass balance, hydrodynamic, aeration and clarifier models, the submodels were the controller, sensor and influent/effluent models. Mass balance modelling takes into account the wastewater constituents as scalars and transport equations describe bio-chemical processes. Activated sludge modelling family (ASM1, ASM2d and ASM3)

describes the suspended growth and decay of biomass, oxygen consumption, organic matter and nutrient degradation [3]. In these models, the hydraulic conditions are simplified, and reactor models are built using the simulation tools to determine the mixing conditions (completely stirred tank reactor, plug flow reactor or any combination of the two idealized reactor model). Calibration of the mass balance model is based on direct measurement of kinetic parameters or following reversed engineering by the knowledge of the actual plant effluent data.

Efficiency of wastewater treatment processes is highly dependent on the flow behaviour and mixing regimes. Wastewater treatment requires oxygenation, which is generally supplied by a diffuser network that provides the required oxygen in aerobic tanks. The aim of aeration is twofold: it provides the necessary oxygen for the biomass and gives movement to the water phase, and it creates appropriate mixing conditions. Mixing is sufficient only if the substrate could be transported to the biomass and side products from the biological activity can be transported out of the system. For understanding these complex features of fluid flow, numerical analysis of fluid flow is required with which the turbulent velocity field can be fully resolved over the simulation domain.

Computational fluid dynamics (CFD) simulation tools are popular in wastewater treatment, numerous research have been done regarding hydraulic aspects of treatment process units, but many processes are not addressed to date [4]. CFD models have primarily been used for design analysis and troubleshooting, but they can be coupled with mass balance (biokinetic) models in which the tank-in-series (TIS) approach is applied widely [5]. It has also been reported that biokinetic models are calibrated by forcing a TIS model to match available data to model parameters, in spite of the fact that TIS neglects the hydrodynamic details of the system [6], especially the small-scale phenomena such as short circuiting and possible dead-zone formation. Applying compartmental models based on CFD calculations [7], the mixing is more detailed compared to TIS, but constructing each compartment zone and connectivity is case-specific.

Biokinetic calculations can theoretically be performed by the extension of the governing equations of fluid flow with scalar equations for biomass, substrate and dissolved oxygen [8], but the processes taken into account are limited. Meister and Rauch [9] were able to couple smoothed particle hydrodynamic approach to ASM1 model, but Reynolds Averaged Navier Stokes (RANS) based models are also proved to be efficient to model an oxidation ditch [10], however more detailed biochemical processes like nitrification/denitrification in ASM2D or Anammox in Mantis model [11] are not effectively coupled with CFD to date.

Based on the literature review, it can be stated that there should be an agreement between the resolution of flow field and the number of biokinetic parameters. Even in simple geometries, transient turbulent multiphase 3D flows have increased the computational capacity need. The aim of this research is to demonstrate the applicability of residence time distribution (RTD) analysis in mass balance modelling.

## 2 MATERIAL AND METHODS

An aerated basin designed for 10,000 $m^3$/d treatment capacity was investigated. The basin geometry is rectangular, and it has a length of 25 m, width of 7.7 m and a depth of 5 m. Disc diffusers with 9" diameter were installed 20 cm from the bottom to prevent fouling from undesired particle settling. Primary-treated wastewater enters the basin 1.5 m above the bottom in a submerged pipe with a diameter of 30 cm, and the effluent leaves the system on the right-hand side as shown in Fig. 1.
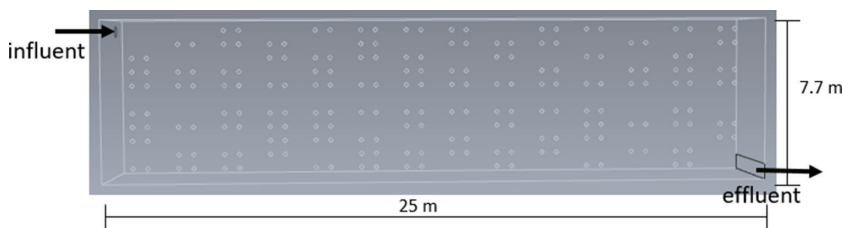
Figure 1: Aerated basin geometry (top view).

The analysis could be divided into the following steps:

- determination of the flow field in aerated basin applying CFD simulation,
- RTD analysis by Lagrangian particle tracking,
- adjustment of TIS model and
- performing mass balance simulations.

## 2.1 Determination of flow field

Flow field simulation procedure includes the following: drawing the geometry, mesh generation (spatial discretization), boundary and initial condition setup, numerical solver selection, iteration and convergence criteria and evaluation of the flow field.

The discretized domain consisted of 383 780 tetrahedral sub-volumes and 779 495 nodes, applying size function at the inlet, outlet section and around the diffusers. Inlet boundary was a constant mass flow neglecting the effect of diurnal pattern of wastewater loading. From the diffuser surface 2 $m^3$/h air is introduced to the system. The surface of the basin lets the gas out from the system (degassing) and the outflow zone was pressure outlet. Steady-state RANS model with $k$–$\varepsilon$ turbulence closure was applied. Despite the fact that this approach assumes isotrophic turbulence [12], it is well tested and widely accepted in wastewater applications [4]. SIMPLE (Semi-Implicit Method for Pressure Linked Equations) scheme was applied for velocity–pressure coupling and second-order upwind techniques was applied for spatial discretization [13]. Convergence criteria were the stability of iteration residuals and the quasipermanent flow field.

Simulation of air-induced flow and the moment of exchange between the gas–liquid phase were modelled by Eulerian–Eulerian approach [14]. Volume fraction of air as a scalar was additionally solved during the entire calculation process.

## 2.2 RTD analysis and TIS model

The objective of introducing a tracer to the system is to gain information of the fluid path lines and the time required to go through the basin. In field experiments the tracer is mainly a conservative material which is not present in the background flow, has no intention for decay or react and relatively easy to detect. In a numerical model, the tracer can have the same properties as the primary fluid. Injecting the tracer to the pre-calculated steady-state flow field could reveal the difference in travel times of the various particles. $E(t)$ is the distribution function of the normalized tracer concentration calculated by the ratio of the exiting
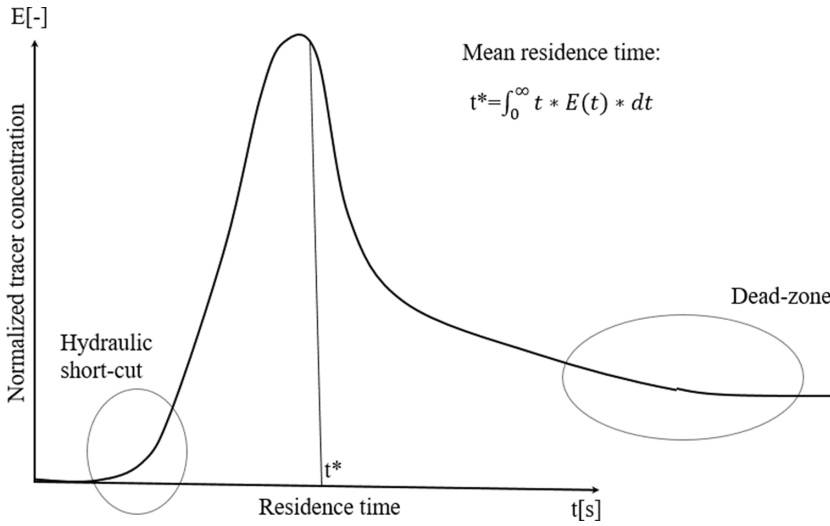
Figure 2: RTD curve.

particles at a given time and the total particles. If some tracer particles are present at the effluent shortly after the injection, it indicates the hydraulic shortcuts in the basin, whereas long travel time means that some particles are trapped in a stagnant zone (see Fig. 2).

The first-order moment of $E(t)$ is the average residence time, and the second-order moment is the standard deviation [15]. From these two variables the Peclet (Pe) number can be calculated that indicates a convective transport rate to diffusion rate. High Pe number means plug flow mixing behaviour without axial dispersion, whereas low Pe indicates completely mixed conditions. In wastewater treatment reactors or basins Pe is normally between 1 and 50 [16], meaning that the actual mixing condition is somewhere between the two idealized approaches. By applying Pe number, the cascading of the completely stirred tank reactors can be determined and then used in mass balance modelling.

## 2.3 Mass balance model

Mathematical formulation of the main scalar variables based on the transport equation, where the kinetic term can be decomposed to process rates and stoichiometric constants. The growth of the heterotrophic biomass can be described as follows:

$$\frac{dX_H}{dt} = (+1) \cdot \mu_H \cdot \frac{DO}{K_{H,O_2} + DO} \cdot \frac{SS}{K_{H,SS}} \cdot X_H \,, \tag{1}$$

where $\mu_H$ is the maximum specific growth rate (1/d), $DO$ the dissolved oxygen concentration (g/L), $K_{H,O_2}$ the half-saturation coefficient of oxygen (g/L), $SS$ the soluble substrate concentration (g/L), $K_{H,SS}$ the half-saturation coefficient of soluble substrate (g/L) and $X_H$ the heterotrophic biomass concentration (g/L).

Calibration of the biokinetic model can be a step-wise procedure by changing the lowest number of parameters. Steady-state calibration follows the logic of adjusting the selected parameters in order to match the effluent composite or state variables describing the organic content: total suspended solid (TSS) and chemical oxygen demand (COD) and COD fractions.
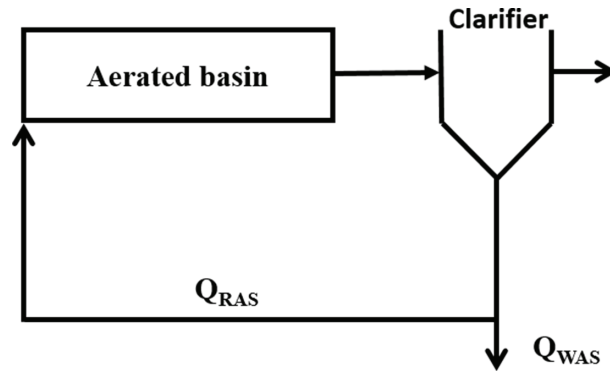
Figure 3: Simplified process scheme of the activated sludge treatment.

Data for calibration was taken from a system, where the biomass amount was stable over time. 24-h composite COD and TSS measurements were performed for a week. Samples were taken from the influent and effluent. After the sampling and laboratory measurements, plausibility check and reconciliation were performed. Dissolved oxygen concentration was 2.5 mg/L, and thus oxygenation is not a limiting factor in organic matter degradation, therefore it is enough to adjust the heterotrophic biomass yield and decay rate in the calibration process.

Only organic matter degradation was aimed in this system, therefore the process scheme could have been simplified (Fig. 3). In order to increase the solid retention in aerated basin, part of the recirculated sludge (RAS: recirculated activated sludge) is reverted to the aeration basin. Wasted activated sludge (WAS) is a portion of sludge sent to the sludge line for stabilization and dewatering. Basically RAS is responsible for maintaining the elevated activated sludge concentration (in other words: mixed liquor concentration, MLSS) in the aerated basin, and WAS controls the solid retention time.

## 3  RESULTS AND DISCUSSION

Steady-state CFD simulations were performed in order to determine the flow field. Average dry weather flow of $Q = 10$ MLD plus RAS flow of 0.8Q was set at the inlet boundary, resulting in a relatively high inlet velocity of 2.1 m/s. The integral averaged velocity in the entire basin was 0.11 m/s, from which the vertical component was only 0.7 cm/s primarily causing the aeration. Horizontal velocity was more than one order of magnitude higher compared to vertical velocity. Figure 4 shows that the influent flow momentum governs the entire flow field, which may cause short circuiting. It will be advisable to apply distributed inlet instead of a point-like influent source.

RTD analysis was performed by releasing 1000 particles through the inlet section at various integration step and time, and in each case the incomplete and existing particles were calculated. The theoretical residence time calculated by the ratio of the basin volume of the incoming flow was 1.28 h. In a tracer study, the first particle appeared at the effluent section only spent 950 s in the reactor, whereas little more than 10% of the particles remained in the system for more than 2 h. The cumulative function of the numerical RTD can be seen in Fig. 5. The average residence time from the curve is 0.83 h, which is lower than the theoretical value. The cause of the difference is in the non-ideal flow field, the presence of turbulent jet caused by the inlet geometry. This result leads to the hypothesis that the mass balance model, which assumes the higher residence time, overpredicts the biodegradation performance of this system.
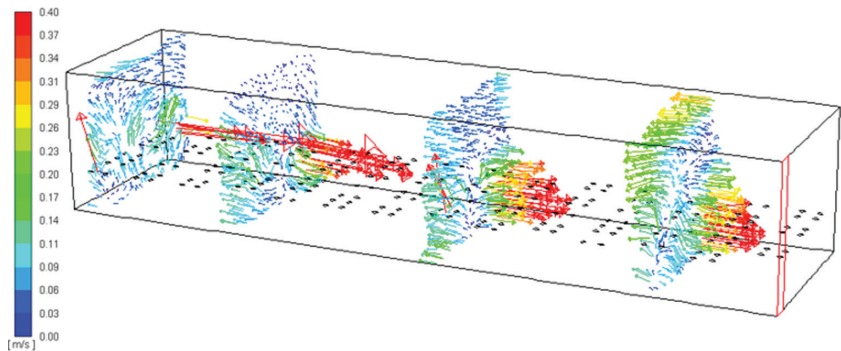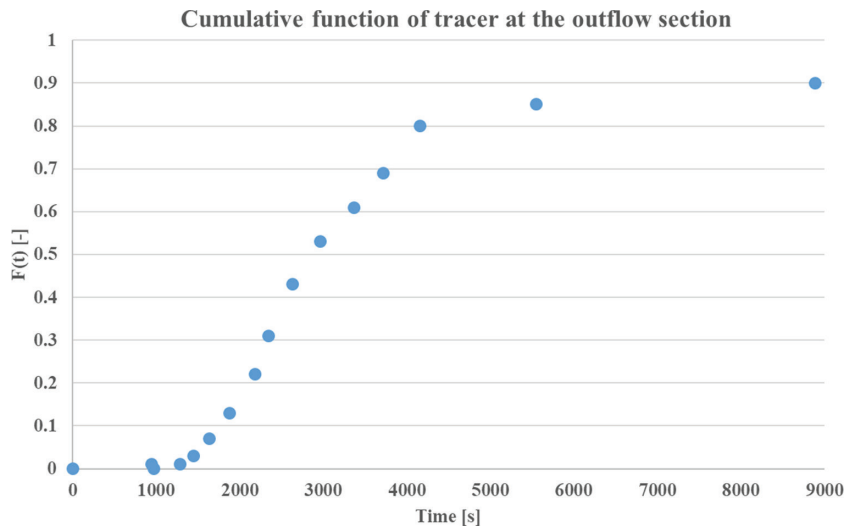
Figure 4: Velocity vectors at sections (m/s).



Figure 5: Cumulative function of tracer at the outflow section.

Standard deviation of the residence time is 915 s. The Peclet number is 21.15, the number of cascaded reactors is approximately 11. The diffusivity is 0.047; a value close to the plug flow reactor's mixing condition [17].

In the following mass balance model was developed as described in Section 2. Firstly, influent characterization was done, various COD fractions were calculated. The incoming 820 mg/L total COD can be fractionated as follows: slowly biodegradable particulate: 425 mg/L, non-biodegradable particulate 102 mg/L, soluble biodegradable 249 mg/L, inert soluble 44 mg/L, reflecting a typical raw communal wastewater quality. The soluble biodegradable fraction is ready for the instant use of heterotrophic microorganisms, thus it projects an effective denitrification process. TSS in the raw influent was 432 mg/L, from which 80% was the organic content. Table 1 shows the detailed influent variables as well as the effluent data. Plant effluent is the measured average treated water quality comes from laboratory measurements.

ASM2d model was applied in GPS-X 6.5 simulation environment, the plant layout was constructed and fed with dimensional and operational data. MLSS concentration in the

Table 1: Wastewater quality in influent and treated effluent.

|  | Raw influent | Plant effluent | Model effluent (1 basin) | Model effluent (adjusted model) |
|---|---|---|---|---|
| COD | 820 | 102 | 75 | 86 |
| $BOD_5$ | 320 | 20 | 14 | 17 |
| TSS | 432 | 23 | 16 | 22 |
| TN | 85 | 22 | 20 | 25 |
| $NH_4$-N | 59 | 2.3 | 1.0 | 1.2 |

aerated basin was 3.5 g/L, the aerobic sludge retention time was 2.4 d which is sufficient for organic removal at temperature of 20°C. Wasted sludge flow was 200 $m^3$/d at dry solid concentration of 7 g/L. The dissolved oxygen concentration was 2.5 mg/L.

Applying calibration process described in Section 2, the aerobic heterotrophic yield and aerobic heterotrophic decay rate was adjusted. The previous one had a value of 0.75 gCOD/gCOD, the latter one was 0.6 1/d.

Two modelling scenarios were calculated. One with a compartment reactor, which is completely mixed, and the other one is a cascaded reactor system, in which the cascade element number came from CFD simulation—adjusted model, assuming 11 reactors in cascade. Table 1 contains the model effluent data showing that one element cascade overpredicted the performance of organic matter degradation. However, there is a discrepancy between the adjusted model and plant effluent COD data. The reasons could be the lack of data on the model variables (fractions). Besides this fact, the clarifier model might have overpredicted thickening, resulting lower TSS value modelled compared to experimental result.

Neglecting these effects a simple sensitivity analysis revealed that if the cascade element number is increased or decreased by 1, 2 or 3 elements, the modelled effluent COD concentrations differed only 2%, 3.5% and 6%, respectively. It should be noted that although there is no significant effect of compartment number at these relatively high reactor numbers, but if one or two reactor number is changed to three or four, the impact would be higher. Other aspect of cascading reactors is the sludge production, which can be reduced in case of plug flow; different substrate concentrations are favoured by the microorganisms, and a so-called food chain could be presented if there is no high axial dispersion. In food chain reactors higher order microorganisms consume the protozoa or simple organisms reduce the TSS.

## 4  CONCLUSIONS

The efficiency of wastewater treatment processes is determined by biological as well as hydrodynamic conditions. Mass balance (biokinetic) modelling often simplifies the mixing conditions in reactors and may cause discrepancies in the estimation of treated effluent wastewater quality. The capacity of wastewater treatment plants can be overestimated that may lead to violation of effluent quality requirement. CFD simulations could reveal the actual mixing conditions within the aeration basin. Multiphase modelling was performed in a biological reactor, in which aeration induced flow creates a vertical flow, the influent discharge is responsible for horizontal movement of the substrate and biomass. Mixing zones were separated and cascade element number was determined by numerical RTD analysis. Reactor compartment number was adjusted in mass balance modelling, the environment and organic

removal was investigated and compared with field data. It could be stated that applying adjusted model is in close agreement with field data, but there are still discrepancies. Furthermore, it can be added that assuming idealized reactor models it may overpredict process performances, therefore the real flow and mixing conditions shall be explored prior mass balance modelling. In the future, process parameters shall also be calibrated against actual flow conditions.

## REFERENCES
[1] Somogyi, V., Pitas, V., Domokos, E. & Fazekas, B., On-site wastewater treatment systems and legal regulations in the European Union and Hungary. *Agriculture and Environment*, **1**, pp. 57–64, 2009.

[2] Tchobanoglus, G., Burton, F. & Stensel, H.D., Wastewater engineering: treatment and reuse. *American Water Works Association Journal*, **95**(**5**), p. 201, 2003.

[3] Henze, M., Gujer, W., Mino, T. & van Loosdrecht, M.C., *Activated Sludge Models ASM1, ASM2, ASM2d and ASM3*, IWA Publishing, 2000.

[4] Samstag, R.W., Ducoste, J.J., Griborio, A., Nopens, I., Batstone, D.J., Wicks, J.D. & Laurent, J., CFD for wastewater treatment: an overview. *Water Science and Technology*, **74**(**3**), pp. 549–563, 2016. https://doi.org/10.2166/wst.2016.249

[5] Wicklein, E., Batstone, D.J., Ducoste, J., Laurent, J., Griborio, A., Wicks, J.... & Nopens, I., Good modelling practice in applying computational fluid dynamics for WWTP modelling. *Water Science and Technology*, **73**(**5**), pp. 969–982, 2016. https://doi.org/10.2166/wst.2015.565

[6] Alvarado, A., Vedantam, S., Goethals, P. & Nopens, I., Compartmental models to describe hydraulics in full-scale waste stabilization ponds. *Water Research*, **46**(**2**), pp. 521–530, 2012. https://doi.org/10.1016/j.watres.2011.11.038

[7] Le Moullec, Y., Gentric, C., Potier, O. & Leclerc, J.P., Comparison of systemic, compartmental and CFD modelling approaches: application to the simulation of a biological reactor of wastewater treatment. *Chemical Engineering Science*, **65**(**1**), pp. 343–350, 2010. https://doi.org/10.1016/j.ces.2009.06.035

[8] Rehman, U., Maere, T., Vesvikar, M., Amerlinck, Y. & Nopens, I., Hydrodynamic-biokinetic model integration applied to a full-scale WWTP. In *9th IWA World Water Congress and Exhibition*, 2014.

[9] Meister, M. & Rauch, W., Wastewater treatment modelling with smoothed particle hydrodynamics. *Environmental Modelling & Software*, **75**, pp. 206–211, 2016. https://doi.org/10.1016/j.envsoft.2015.10.010

[10] Karpinska, A.M. & Bridgeman, J., CFD-aided modelling of activated sludge systems–a critical review. *Water Research*, **88**, pp. 861–879, 2016. https://doi.org/10.1016/j.watres.2015.11.008

[11] Bencsik, D. & Karches, T., Modelling greenhouse gas emissions of a hybrid fixed-film anammox process treating sludge dewatering centrate in wastewater treatment. *British Journal of Environment and Climate Change*, **6**(**4**), pp. 250–258, 2016. https://doi.org/10.9734/bjecc/2016/26725

[12] Launder, B.E. & Spalding, D.B., The numerical computation of turbulent flows. *Numerical Prediction of Flow, Heat Transfer, Turbulence and Combustion*, Pergamon, pp. 96–116, 1983. https://doi.org/10.1016/b978-0-08-030937-8.50016-7

[13] Ferziger, J.H. & Peric, M., Computational methods for fluid dynamics. *Springer Science & Business Media*, 2012.

[14] Pfleger, D., Gomes, S., Gilbert, N. & Wagner, H.G., Hydrodynamic simulations of laboratory scale bubble columns fundamental studies of the Eulerian–Eulerian modelling approach. *Chemical Engineering Science*, **54(21)**, pp. 5091–5099, 1999. https://doi.org/10.1016/s0009-2509(99)00261-4

[15] Fogler, H.S., *Essentials of Chemical Reaction Engineering: Essential Chemical Reaction Engineering*, Pearson Education, 2010.

[16] Ke, T., Tao, T.W.Z.Y.J. & Tian, L.X.L., Impact of Peclet number on heat transfer of oscillatory flow in circular channel. *Cryogenics*, **3**, p. 2, 2011.

[17] Khudenko, B.M. & Shpirt, E., Hydrodynamic parameters of diffused air systems. *Water Research*, **20(7)**, pp. 905–915, 1986. https://doi.org/10.1016/0043-1354(86)90180-6

*This page intentionally left blank*

# FIRST WHOLLY-ANALYTICAL GAS VOLUME FRACTION MODEL FOR VIRTUAL MULTIPHASE FLOW METERING PETROLEUM INDUSTRY APPLICATIONS

ANAND S. NAGOO
Nagoo & Associates LLC, Austin, Texas, USA.

## ABSTRACT

In this seminal contribution, the world's first wholly-analytical gas volume fraction multiphase flow model is formulated and demonstrated in virtual flow meter and production allocation field applications for its differentiated ability to achieve improved reliability of phase flow rate calculations given pressure and temperature measurements at two different locations along multiphase production systems. The presented simple gas volume fraction equation is explicit in form and is validated against both lab data and oilfield flowline data. A crucial requirement for differential pressure flow meters for multiphase production systems, particularly wet gas systems in annular and annular-mist flows, is the calculation of the averaged gas volume fraction. Additional calculations include multidirectional entrainment calculations, which strongly affect the simultaneous entrainment of liquids in the gas phase and the gas in the liquid phases. Historically, prior published gas volume fraction two-phase flow models had closure relations and artificial adjustment (fitting) factors linked to controlled lab-scale conditions involving immiscible fluids that bear no resemblance to the complex petroleum mixtures undergoing phase change in uncontrolled long wellbore and flowline environments. Thus, ambiguous extrapolations were necessary leading to increased uncertainties. Using an asymptotic approximation analysis approach, an analytical gas volume fraction equation is derived that overcomes this empirical-based restriction. In terms of comprehensive validation, the presented analytical gas volume fraction equation is demonstrated first for its ability to reliably reproduce over 2600 two-phase annular and annular-mist flow experimental datasets inclusive of circular and non-circular conduits. Secondly, readily available published experimental data of both constant-diameter as well as variable-diameter sub-critical to critical choke two-phase flows are used for model validation in scenarios involving different flow obstructions. Lastly, an offshore subsea flowline dataset is used to demonstrate the improved reliability of the new equation at field-scale operational conditions.
*Keywords: Multiphase Flow Metering, Oil Production Allocation, Offshore Flowline and Onshore Production Systems, Volume Fractions and Flow Rates Prediction, Wet Gas Virtual Flow Metering.*

## 1 INTRODUCTION

The well-recognized needs for consistently accurate multiphase flow metering (MPFM) in the petroleum industry stem from the fact that a reliable determination of the in-line flow rates of the unprocessed oil, gas and water phases, is necessary for allocating the production from oil and gas assets, for well testing and for continuous monitoring and optimization of production. In contrast to partially and fully separated multiphase flow meters such as test separators on petroleum production systems, in-line MPFM measurements and calculations are meant to determine the oil, water and gas flow rates without any processing or conditioning. Such in-line MPFM technologies and applications have been in wide-spread use since the early 1990's [1]. A good review and description of various available in-line MPFM technologies and devices can be found in [2]. Furthermore, detailed descriptions of prior theories and algorithms used in either the inferred measurements of physical flow meters or in physics-based flow metering models (i.e. virtual flow meters, VFM), can be found in [3] and [2]. In a more recent application of MPFM, an example of using physics-based flow metering models in combination with automatic calibration using artificial data-fitting factors derived from Data Analytics (i.e. 'smart' virtual flow meters, SVFM), can be found in [4].

Among the various approaches used to measure or calculate the three-phase flow rates of a production system, it is well-recognized that those approaches involving the calculation of gas volume fraction will lead to a more consistently reliable prediction of phase flow rates due to the inherent relationship between phase volume fractions, velocities and pressure gradient [2]. This is no surprise since this relationship is merely a manifestation of the law of conservation of total momentum of the flowing multiphase mixture. In particular, MPFM calculation algorithms utilize different forms of this relationship in combination with a viscous loss coefficient and the discernible pressure drop across restricted multiphase flows (such as through nozzles, orifices and critical/sub-critical chokes) to obtain more reasonable estimates of flow rates. The question then arises as to which gas volume fraction model to use in a MPFM calculation algorithm for the best *reliably predictive* results? The answer to this question is the scope of this work.

We emphasize here that our aim is to avoid empirical lab-based correlations for gas volume fraction (i.e. avoid the numerous scaling problems from lab to field) and to avoid calibration in any form since all calibration involving data-fitting decreases predictability since they increase unknowns (increased fitting factors) and lock in the predictive path of models. The practical benefit of a reliably accurate calculation of gas volume fraction for use in VFM or MPFM applications will be to enhance the predictive capability of such devices/algorithms. Additionally, reliable multiphase flow metering calculations present a cost-effective solution for monitoring production at any point along the production system, either standalone or as back-up to installed multiphase flow metering equipment, even in environments where pressure and temperature sensors in wells or flowlines can fail over time.

Last, although the emphasis of this work is on the gas volume fraction analytical model development, other important multiphase calculations that must necessarily go into VFM or MPFM algorithm routines, such as multidirectional entrainment and the thermodynamic conversion of volumetric phase flow rates at standard conditions to in-situ mass flow rates can be found in [5] and [6], respectively. For the generation of all simulation results in this paper, we utilize the analytical multiphase flow methods found in [6].

## 2 DERIVATION OF THE ANALYTICAL GAS VOLUME FRACTION MODEL

Considering above, a correlation-free and mathematically consistent model for gas volume fraction (or gas void fraction) will significantly improve the predictive accuracy and stability of multiphase flow meter calculation algorithms. Firstly, such a model will avoid the large, ambiguous inaccuracies that arise from scaling lab-based low pressure and temperature experiments with immiscible (irrelevant) fluids to field scale environments at high pressure and temperature with complex miscible (petroleum) fluids. Secondly, such a model will avoid artificial data-fitting factors of automated or manual calibration routines, regardless of whether the fitting factors come from tuning/training datasets or not. Indeed, more calibration increases unknowns (more fitting factors) and decreases model predictability in scenarios outside of tuning datasets. Thirdly, such a model must be smooth, continuous and differentiable to enable its use in inverse differential pressure flow meter algorithms that utilize pressure drops to arrive at *unique solutions* to the in-situ mass flow rates. To this end, an asymptotic approximation analysis is invoked below to derive such an analytical gas volume fraction model.

In continuation of the specific terminology and *pipe fractional flow* language of [7], for a generic heavier phase 1 (e.g. a liquid) and a generic lighter phase 2 (e.g. a gas), similar to the slip ratio between phase 2 and phase 1, $H_{2,1}$, we can define another dimensionless velocity ratio which we call the *relative velocity slip ratio*, $\Omega_{2,1}$, which is the ratio of the relative velocity to the mixture velocity of the flowing two-phase mixture:

$$\Omega_{2,1} = \frac{\overbrace{\langle\langle v_2 \rangle\rangle - \langle\langle v_1 \rangle\rangle}^{relative\ velocity}}{\langle u_{mix} \rangle} \tag{1}$$

In eqn. (1), $\langle\langle v_2 \rangle\rangle$ is the averaged in-situ velocity of phase 2, $\langle\langle v_1 \rangle\rangle$ is the averaged in-situ velocity of phase 1, and $\langle u_{mix} \rangle$ is the mixture velocity $= \langle\langle v_2 \rangle\rangle\langle s_2 \rangle + \langle\langle v_1 \rangle\rangle(1 - \langle s_2 \rangle)$ where $\langle s_2 \rangle$ is the averaged phase 2 volume fraction or averaged gas volume fraction in a gas-liquid flow. Therefore, we see with this simple definition, all the in-situ velocities and volume fractions are captured. This is not the case with the slip ratio definition, $H_{2,1}$, which only captures the slip of one phase relative to the other. As noted in [7], from a transport phenomena perspective, the objectively measurable changes in the in-situ phase velocities and volume fractions associated with each flow pattern are the fundamental physical quantities that govern the transport processes of the multiphase flow. It is these transport processes that drive the different mass, momentum and energy exchanges occurring during flow. This is why flow patterns matter because they represent the visual (spatio-temporal) manifestations of the measurable changes in the in-situ velocities and volume fractions during the multiphase flow.

Now, let's start our derivation by postulating what the upper limit (the upper asymptote) of eqn. (1) would look like. In this limit, in terms of the physical mechanisms at play, phase 1 (the liquid phase in the case of gas-liquid flow) is entraining fully into phase 2 (the gas) and therefore, regardless of the other velocities in the multiphase flow, $\langle\langle v_1 \rangle\rangle$ will tend to 0, $\langle s_2 \rangle$ will tend to 1 and thus $\langle\langle v_2 \rangle\rangle$ will tend to $\langle u_2 \rangle$, the superficial velocity of phase 2. This can be expressed as:

$$\Omega_{2,1} = \frac{\langle\langle v_2 \rangle\rangle - \langle\langle v_1 \rangle\rangle}{\langle u_{mix} \rangle} \overset{\substack{in\ an\ upper \\ flow\ limit}}{\longrightarrow} \frac{\overbrace{\langle\langle v_2 \rangle\rangle}^{\substack{approches\ \langle u_2 \rangle \\ in\ upper\ limit}} - \overbrace{\langle\langle v_1 \rangle\rangle}^{\substack{relatively\ negligible \\ in\ upper\ limit}}}{\langle u_{mix} \rangle} = f_2 \tag{2}$$

In eqn. (2) above, $f_2$ is the flowing fraction of phase $2 = \langle u_2 \rangle / \langle u_{mix} \rangle$. Now, if we re-express eqn. (1) in the dimensionless terms of $f_2$ and $\langle s_2 \rangle$, we get:

$$f_2 = \left(1 + \left(1 - \langle s_2 \rangle\right)\Omega_{2,1}\right)\langle s_2 \rangle \tag{3}$$

It is noteworthy at this juncture to point out that eqn. (3) above is the same as eqn. (5) of [7] but this time expressed in terms of the dimensionless relative velocity ratio form. Substituting eqn. (2) in eqn. (3), we will then arrive at:

$$f_2 = \frac{\langle s_2 \rangle}{1 - \langle s_2 \rangle\left(1 - \langle s_2 \rangle\right)} \tag{4}$$

And equivalently, solving for $\langle s_2 \rangle$ (i.e. the gas volume fraction in a gas-liquid flow) in eqn. (4), we arrive at the analytical expression for $\langle s_2 \rangle$ in terms of the flowing fraction, $f_2$, as:

$$\langle s_2 \rangle = \frac{f_2 + 1 - \left[ (f_2 + 1)^2 - 4(f_2)^2 \right]^{\frac{1}{2}}}{2f_2} \tag{5}$$

Equations (4) and (5) above are the *main results of this paper* – the wholly-analytical, correlation-free equation for gas (phase 2) volume fraction in a two-phase flow. Equation (4) is referred to as 'ANSLIP' (meaning analytical slip) in [6]. In terms of dependencies, it is important to note that although the gas volume fraction, $\langle s_2 \rangle$, in eqn. (5) is given as a direct function of gas flowing fraction, $f_2$, all the other parameters and dependent variables in a multiphase pipe flow such as pipe inclination, diameter, flowing area, densities, viscosities, etc. will be found in the calculation of the gas flowing fraction, $f_2$, when eqn. (5) is used in a multiphase flow computational simulator environment (e.g. as in [6]). Therefore, the same variables and parameters involved in the calculation of superficial and mixture velocities of the gas flowing fraction (which are functions of pressure and temperature) contribute implicitly to the calculation of the gas volume fraction.

In terms of mathematical form, although from the derivation above one might initially expect eqn. (4) to be best applicable to high gas volume fraction flows (i.e. churn-annular, annular, annular-mist, wet-gas flows), a plot of $f_2$ versus $\langle s_2 \rangle$ reveals a broader, behaviour-capturing nature of this equation, as seen in Fig. 1 below. It is notable that the major multiphase flow pattern regions of bubbly (or dispersed) flows at about $\langle s_2 \rangle < 0.3$, transitional (or slug/churn) flows at about $0.3 < \langle s_2 \rangle < 0.75$, and annular (or separated) flows
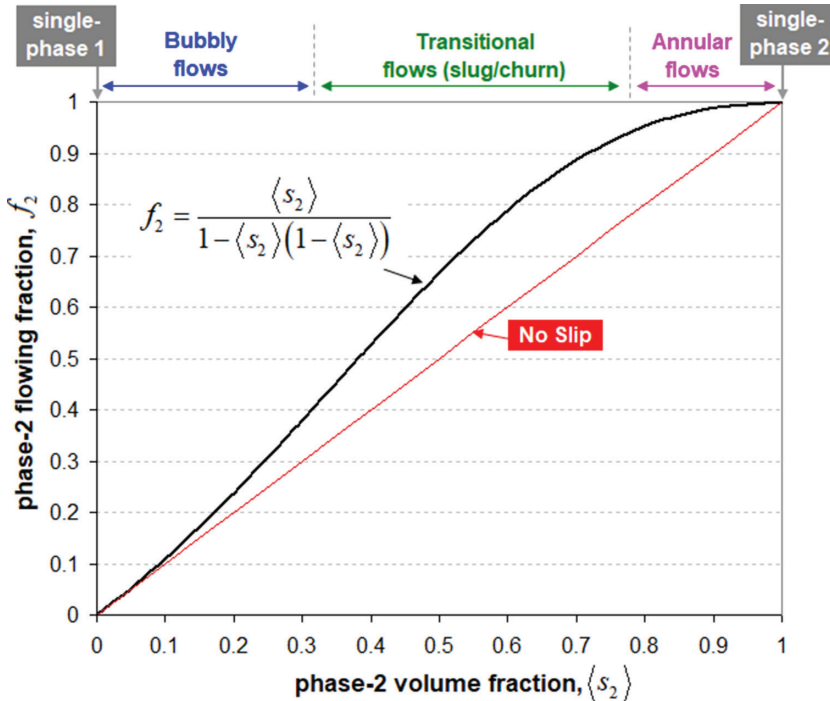


Figure 1: Graphical representation of eqn. (4), the main result of this work.

at about $\langle s_2 \rangle > 0.75$ are captured in terms of their relationships to the amount of slip these flow patterns display. The amount of slip in the *fractional flow plot* of Fig. 1 is depicted by the distance of the model from the *no slip* line. As can be seen, slug and churn flows will typically have the highest slip followed by annular flows and then bubbly flows. Therefore, by analysing the form of eqn. (4), which is graphically depicted by Fig. 1, we can expect that eqn. (4) will find applicability to a wide range of vertical-up, up-inclined and horizontal multiphase flows, and will have its highest accuracy for high gas volume fraction (or high gas rate) flows.

In terms of the limiting applicability of eqn. (4), we note that the lower gas volume fraction predictions for down-inclined flows are not generally expected to follow eqn. (4) since Fig. 1 shows that the equation does not functional represent the portion of the *fractional flow plot* below the *no slip* line at lower gas volume fractions, which indicates regions where phase 1 flows faster than phase 2. Also, for specific types of gas-liquid flows where the bubbly flows will not exhibit a low-slip (or dispersed bubbly flow) behaviour, such as heavy oil and gas flow or flows with high slip at low gas volume fractions, eqn. (4) is not expected to accurately describe such gas volume fraction behaviours. In this latter case, a gas volume fraction model that allows for high slip at low gas volume fractions should be used (e.g. as found in [8]).

### 3  MODEL VALIDATION AGAINST PUBLISHED LAB AND FIELD DATASETS

For the remainder of this work, we compare the performance of eqn. (4) in both validation tests (below) and in new VFM algorithms for calculating three-phase flow rates (next section).

### 3.1  Non-obstructed lab multiphase flows – constant-diameter closed conduit

In the first validation lab dataset for constant-diameter closed conduits, we select the large database of published experiments given in [9]. In this reference for annular flows, inclusive of churn-annular to annular mist flows, an empirical correlation for gas volume fraction is obtained through the traditional means of non-linear parametric regression. The datasets over which the regressed correlation is drawn spans a gas (phase 2) volume fraction range of $0.7 < \langle s_2 \rangle < 1$, and includes 2,633 datapoints for circular tubes covering macroscale to microscale flow conditions and 40 additional datapoints for non-circular channels.

In order to compare the predictive reliability of eqn. (4) against this database, we plot the empirical correlation of [9] against eqn. (4) for the common experimental flow loop conditions of air density = 1.2 kg/m$^3$ and water density = 1000 kg/m$^3$. As is evident from Fig. 2, the very close match of eqn. (4) with this large experimental database (captured by the empirical correlation) demonstrates the accuracy of eqn. (4) and signifies that the time-consuming approach of gathering large amounts of data and regressing upon adjustable parameters of a model can be overcome by simple and mathematically consistent physical arguments (i.e. careful reasoning rather than 'brute force').

### 3.2  Obstructed (restricted) lab multiphase flows – variable-diameter chokes & nozzles

In the second validation lab dataset for constant-diameter closed conduits, we select the large database of published experiments given in [10]. The datasets of this reference include the full range of flow patterns. In Fig. 3 above, one gas volume fraction and total pressure gradient dataset corresponding to run names of 'WR4.01' to 'WR4.15' in the reference, are selected to show how eqn. (4) is used to first predict the gas volume fraction (Fig. 3a), and then the
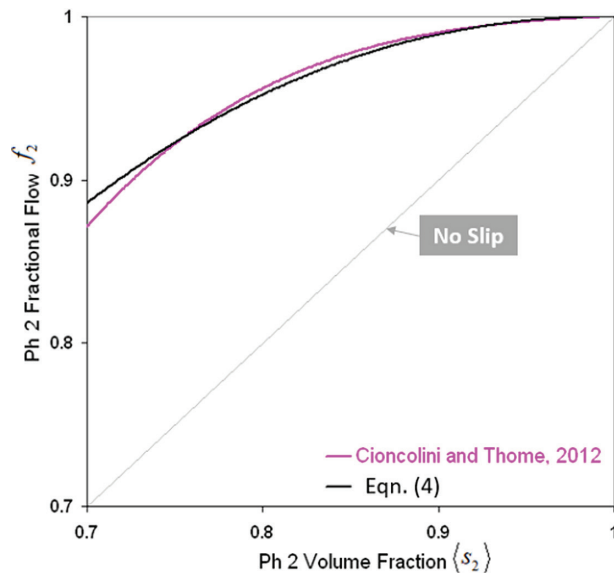
Figure 2: Comparison of the wholly analytical eqn. (4) against a vapor (phase 2) and liquid (phase 1) annular flow empirical correlation [9] inclusive of churn-annular to annular-mist boundaries. The underlying experimental database for the correlation contains 2,633 datapoints for circular tubes covering macroscale to microscale flow conditions and 40 additional datapoints for non-circular channels.
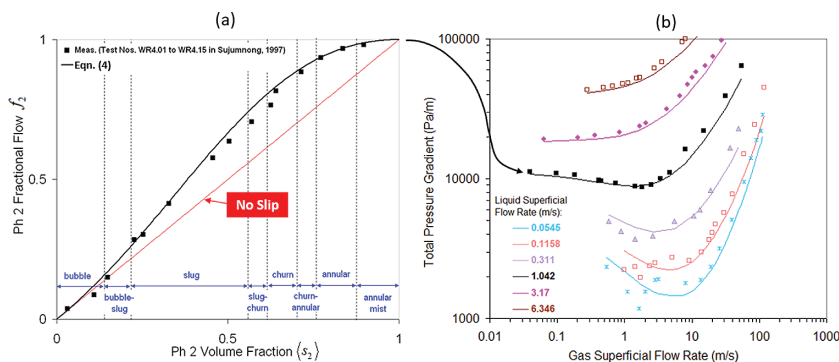


Figure 3: Demonstrating how eqn. (4) can be used to predict both the air volume fraction (in b) and pressure drops (in a) of three different sub-critical to critical horizontal air-water choke flow datasets of [11]. Lines are calculations (outlet specified) and points are data.

predicted gas volume fraction is used within the total pressure gradient model for predicting the total pressure gradient dataset at a liquids superficial flow rate of 1.042 m/s (Fig. 3b). It should be noted how eqn. (4) smoothly transitions through each flow pattern and integrates the different slip velocity transitions as the flow pattern changes. Finally, for comparison, other predictions of pressure gradients using eqn. (4) for the gas volume fraction calculation at different liquid superficial flow rates are additionally shown in Fig. 3b.

### 3.3 Obstructed (restricted) lab multiphase flows – variable-diameter choke

In addition to the constant diameter lab datasets above, we now validate eqn. (4) against three restricted, variable diameter two-phase flow lab datasets sourced from the horizontal multiphase choke flow datasets in [11]. In the reference, we select datasets transitioning the boundary from sub-critical choke flow (runs '21171' and '21170') to critical choke flow (run '21169'). This validation serves an important application of the use of eqn. (4) for gas volume fraction calculations in applications involving critical to sub-critical choke multiphase flows. Note that for the datasets in this section (as well for the remainder of this paper), eqn. (4) is used within the analytical simulator in [6] in which the variable-diameter flow path is carefully discretized into a multi-segmented pipe system that conforms to the flow path. This discretization can be similarly applied to sharp, short obstructions (such as plate orifices or small constrictions) in addition to smooth, long obstructions as given in this choke example and nozzles. Clearly, the character and magnitude of the pressure gradients and phase volume fractions will change in accordance with both the varying segment axial length and varying segment cross-sectional areas along the profile of each differently discretized system.

In Fig. 4 above, each run starts at the specified outlet pressure (varying from low to high pressure) and the gas volume fraction and total pressure gradient calculations are performed
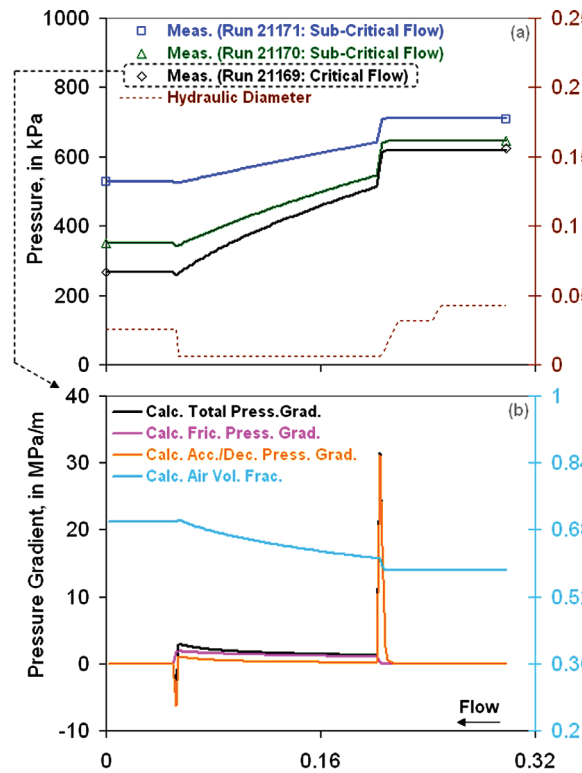


Figure 4: Demonstrating how eqn. (4) can be used to predict both the air volume fraction (in *b*) and pressure drops (in *a*) of three different sub-critical to critical horizontal air-water choke flow datasets of [11]. Lines are calculations (outlet specified) and points are data.

along the segmented choke system denoted by a dotted line profile shown by the right axis of Fig. 4a. Note that all subcritical and critical choke multiphase flows are accurately predicted using eqn. (4). It is also important to highlight that in varying diameter flows, as depicted in Fig. 4 above, the convective acceleration/deceleration pressure gradient term will dominate during the contraction and expansion parts of the choke device, where the flow will accelerate (positive pressure gradient) during contractions and decelerate (negative pressure gradient) during expansions. Additionally, the frictional pressure gradient will dominate along the constant small-diameter section of the choke.

### 3.4 Validation against published offshore (subsea) flowline field dataset

Next, in addition to validation comparisons of eqn. (4) against the lab-scale datasets above, we now shift attention to a published, field-scale gas-condensate subsea flowline dataset with real petroleum fluids exhibiting gas dew point mass exchange behaviours (e.g. gas coming out of condensate and condensate dropping out of gas) found in [12]. These tests examine the validity of eqn. (4) in scenarios of changing flowing fractions along the system flow path representing the always-changing superficial gas velocities and mixture velocities during the multiphase flow as pressure and temperature drops.

For this validation, we select the published offshore North Sea Frigg to St. Fergus gas-condensate subsea flowline dataset of [12], in which both surface pressure and temperature measurements and pigged flowline condensate volumes measurements are readily available for comparisons against both total pressure gradient and gas volume fraction simulations using eqn. (4). Additionally, this is a very long 226 miles, 32-inch diameter subsea flowline that flows gas and condensate from the Frigg offshore platform to an intermediate 'MCP01' platform and then on to the St, Fergus onshore complex as shown in the elevation (seabed) profile Fig. 5a. The prevailing flow pattern is annular flow with a very high gas-to-condensate ratio (GCR) of 1 MMscf/BBL at various condensate rates as shown in Fig. 5b. Pressure and temperature data are available on surface at the Frigg platform and the St. Fergus complex and sometimes available at the intermediate platform for each for the condensate flow rates shown in Fig. 5b.
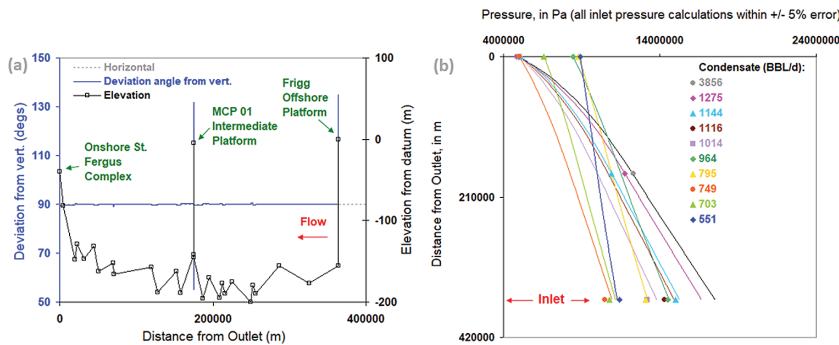


Figure 5: Demonstrating how eqn. (4) can be used to predict both the condensate holdup (or condensate volume fraction) and total pressure drops in *b*, for the elevation profile of the 226 miles long, 32-inch diameter North Sea subsea Frigg flowline [12] in (*a*). In (*b*), lines are our analytical simulations and points are pressure gauge data.

As is clear from the results of Fig. 5b, eqn. (4) is ideally suited for this annular flow dataset and yields a high accuracy for *all* the reported pressure gauge data within +/- 5 % error. For these data, all simulations started with the fixed outlet pressure and the pressure profiles and inlet flowline pressures were predicted using eqn. (4).

## 4  NEW ALGORITHM FOR CALCULATING FLOWLINE FLOW RATES USING KNOWN SURFACE PRESSURE AND TEMPERATURE DIFFERENCES

In this final validation section, we will utilize eqn. (4) in a new algorithm for field-scale virtual multiphase flow metering calculations presented below by utilizing the pressure and temperature differences along a subsea pipeline to calculate its producing condensate and gas flow rates. For this calculation, we select one of the flow rates of the North Sea Frigg subsea flowline dataset from the previous section, i.e. the dataset at condensate rate of 1144 BBL/d. The corresponding outlet MCP01 platform pressure of 10.92 MPa and temperature of 5.5ºC will be used as the starting point in our simulations. For the given inlet Frigg platform pressure of 15 MPa and temperature of 47ºC, our goal then is to find the flow rates that yield the minimum absolute difference between the calculated pressure drop between the Frigg and MCP01 platforms ($\Delta P_{calc}$) using eqn. (4) and the measured pressure drop between these platforms of 15 MPa – 10.92 MPa = 4.08 MPa ($\Delta P_{meas}$). This absolute difference is shown on the y-axis of Fig. 6 below.

In setting up this dataset for VFM simulations, we note the total pipeline measured distance (MD) from the Frigg platform to the MCP01 platform = 188,400 m, a horizontal pipeline profile assumption is used, a linear flowing temperature gradient assumption is used, condensate gravity = 70ºAPI, gas gravity = 0.68 (Air = 1.0) and the internal pipeline diameter = 0.7747 m. For our VFM algorithm, we first specify increasing condensate rates in 50-BBL/d increments from 100 to 2000 BBL/d at GCR = 0.5 MMscf/BBL (simulation run # 1 to 39 of Fig. 6), then at the same condensate increments at GCR = 1 MMscf/BBL (simulation run # 40 to 78 of Fig. 6), and finally at the same condensate increments at GCR = 1.5 MMscf/BBL (simulation run # 79 to 117 of Fig. 6).

As clearly seen in Fig. 6, the unknown flow rates can be *uniquely* found for the presented dataset. Simulation number 61 represents the condition of 1150 BBL/d and GCR of 1 MMscf/
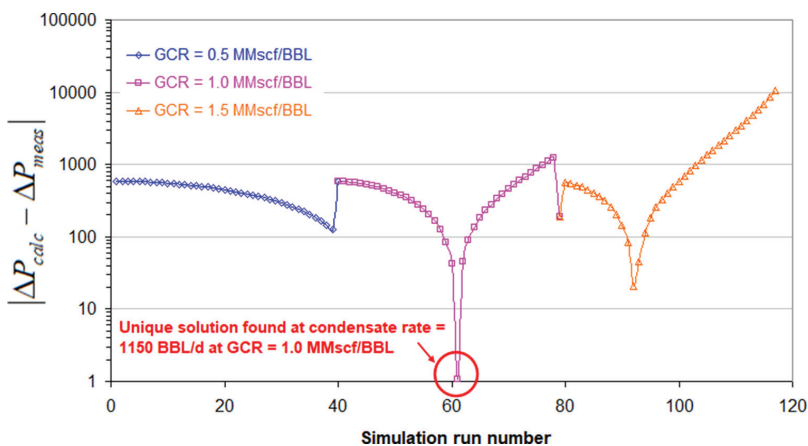


Figure 6: Demonstrating how eqn. (4) can be used to predict the condensate and gas flow rates of one published dataset of the North Sea Frigg subsea flowline in [12].

BBL, which is very close to the actual rates. This procedure of specifying the flow rate combinations and determining the minimum value of $\left|\Delta P_{calc} - \Delta P_{meas}\right|$ can be applied to any flowline.

Last, it should be noted that a similar VFM algorithm to that described above can be applied to oilfield wellbores for predicting three-phase flow rates at the wellhead. In such applications, the calculations of flowing bottom hole pressure (FBHP) from the outlet specified conditions at the wellhead using eqn. (4), i.e. $P_{wf,calc}$, will be compared to the FBHP specified from an inflow performance relationship (IPR) that relates the FBHP to the gas-to-oil ratio (GOR), water cut, total fluids productivity index (PI) and an averaged reservoir pressure, i.e. $P_{wf,IPR}$. The absolute difference to be minimized in this scenario will be $\left|P_{wf,calc} - P_{wf,IPR}\right|$. Additionally, in contrast to the flowline VFM application above, in the wellbore VFM application, only the gas rate needs to be specified in increments from a chosen low value to high value since the corresponding oil rates will be provided from the given GOR and the corresponding water rates will be provided from the given water cut.

## 5 CONCLUSIONS

The validation results of the lab and field case studies given in this work clearly show the *predictive* value of using the presented correlation-free, wholly-analytical gas volume fraction model (eqn. 4) that is smooth, continuous and differentiable, in that unique phase flow rate combinations result when used in conjunction with analytical multiphase flow modelling methods. This is a practically significant finding that is useful for both forward models (using phase flow rates to calculate pressure gradient) as well as inverse models (VFM optimization algorithms using pressure gradient to calculate phase flow rates). The presented model will find ideal use in virtual multiphase flow meter and production allocation field applications in the petroleum industry for its differentiated ability to achieve improved reliability of flow rate predictions.

## REFERENCES

[1] Corneliussen, S., Couput, J.P., Dahl, E., Dykesteen, E., Frøysa, K. E., Malde, E. … & Tunheim, H., Handbook of multiphase flow metering, *Norwegian Society for Oil and Gas Measurement* (NFOGM), Revision, 2, March 2005.

[2] Falcone, G., Hewitt, G.F., Alimonti, C. & Harrison, B., Multiphase flow metering: current trends and future developments. *Journal of Petroleum Technology*, **54(4),** 2002. https://doi.org/10.2118/74689-ms

[3] Mwalyepelo, J.Y., *Analysis of Selected Multiphase Metering Concepts*, M.S. Thesis, Norwegian University of Science and Technology, July 2015.

[4] Whitfield, S., Production monitoring gets smarter with virtual flow metering. *Oil and Gas Facilities*, May 2019.

[5] Nagoo, A.S., *Analytical Modeling of Multidirectional Entrainment in Three-Phase Gas-Liquid-Liquid Flows with Oilfield Applications in High Gas Rate Wellbores and Flowlines*, 10th Intl. Conf. Multiphase Flow, Rio De Janeiro, Brazil, 2019.

[6] Nagoo, A.S., Multiphase Analytical Prediction Engine (MAPe)—an analytical multiphase flow simulator, http://www.nagoo-associates.com, 2018.

[7] Nagoo, A.S. & Sharma, M.M., Finer theoretical aspects of the drift flux family of equations for simulating averaged volume fraction in multiphase flows. *International Journal of Computational Methods and Experimental Measurements*, **6(2)**, pp. 240–250, 2017. https://doi.org/10.2495/cmem-v6-n2-240-250

[8]  Woldesmayat, M.A. & Ghajar, A.J., Comparison of void fraction correlations for different flow patterns in horizontal and upward inclined pipes. *International Journal of Multiphase Flow*, **33(4)**, pp. 347–370, 2007. https://doi.org/10.1016/j.ijmultiphaseflow.2006.09.004

[9]  Cioncolini, A. & Thome, J.R., Void fraction prediction in annular two-phase flow. *International Journal of Multiphase Flow*, **43**, pp. 72–84, 2012. https://doi.org/10.1016/j.ijmultiphaseflow.2012.03.003

[10] Sujumnong, M., *Heat Transfer, Pressure Drop and Void Fraction in Two-Phase, Two-Component Flow in a Vertical Tube*, Ph.D. Dissertation, University of Manitoba, 1997.

[11] Pilehvari, A.A., *Experimental Study of Subcritical Two-Phase Flow Through Wellhead Chokes*, Research Report, Tulsa U. Fluid Flow Projects, September 1980.

[12] Lagiere, M., Miniscloux, C. & Roux, A., Computer two-phase flow model predicts pipeline pressure and temperature profiles, *Oil and Gas Facilities*, April 1984.

*This page intentionally left blank*

# THERMAL-HYDRAULIC RESPONSE OF A REACTOR CORE FOLLOWING LARGE BREAK LOSS-OF-COOLANT ACCIDENT UNDER FLOW BLOCKAGE CONDITION

YOUNG SEOK BANG & JOOSUK LEE
Korea Institute of Nuclear Safety.

## ABSTRACT
Since the revision of the requirements to consider the effect of fuel burnup on emergency core cooling system performance was proposed, flow blockage in reactor core has been one of the important issues in the thermal-hydraulic analysis of loss-of-coolant accident (LOCA). The present paper describes how much flow blockage would be expected following a large break LOCA based on the actual nuclear design data including the power and burnup of the fuel rods. A system thermal-hydraulic code, MARS-KS, is used for calculation where the burnup specific data of the fuel rods is supported by a fuel performance code, FRACON3. To recover the weakness of the system code in which the flow blockage under multiple rods configuration cannot be automatically simulated in hydraulic calculation, a special modelling scheme is developed and applied to the calculation. The effect of flow blockage on the thermal-hydraulic response of the reactor core is also discussed. To compensate for the uncertainty of the present flow blockage model, additional calculations are attempted for a wide range of the level of blockage.
*Keywords: Effect of Fuel Burnup, Flow Blockage in Reactor Core, Hydraulic Modelling of Swelling and Rupture of Cladding, Large Break LOCA, MARS-KS Code.*

## 1  INTRODUCTION
Flow blockage of the reactor core can occur due to swelling and rupture of the cladding of fuel rods following a large break loss-of-coolant accident (LBLOCA) in nuclear power plants (NPPs) and has been required to consider for the analysis of Emergency Core Cooling System (ECCS) performance [1]. Swelling of the cladding is reasoned for the pressure difference between gap and the fluid outside the cladding induced by a significant depressurization following a LOCA, and the degradation of heat transfer to the fluid outside the cladding. Swelling can lead to an excessive plastic deformation and eventually to rupture of cladding when exceeding a certain level of deformation [2]. Accordingly, the level of blockage is dependent on the swelling and rupture over the core.

As the requirement of the consideration of the effect of fuel burnup on ECCS performance was recently proposed [3], the flow blockage has been one of the important issues in the thermal-hydraulic analysis, because it can be severe for the high burnup fuel, and it would cause an unexpected change in thermal-hydraulic response of the core following a LOCA.

The present paper describes firstly how much flow blockage would be expected following a LBLOCA based on the actual nuclear design data including the distributions of power and burnup. For this purpose, a system thermal-hydraulic code, MARS-KS [4], was used and the burnup dependent data of the fuel rods was supported by a fuel performance code, FRACON3 [5]. Since the flow blockage occurred during the transient is not directly simulated in hydraulic calculations of the current system codes, such as MARS-KS and RELAP5 [6], when adopting multiple fuel rods, a special modelling scheme to address this problem was developed in the present study. Use of multiple fuel rods modelling was found in some researches [7], however, the specific treatment of the flow blockage using the system thermal-hydraulic code was not clearly discussed.

Secondly the effect of flow blockage on the thermal-hydraulic response of the reactor core was discussed. Generally, it has been known that the blockage is to improve heat transfer both

upstream and downstream of the blocked region and that a blockage up to 60% has an insignificant effect on core heat transfer [2]. However, it is still questionable whether those results are valid for an actual LBLOCA due to several differences including flow bypass in the core between the experiments [2] and the actual NPP. Accordingly, the uncertainties of the code and calculation of the swelling and rupture in the actual reactor core should be considered to cover sufficiently the effect of those differences. For this aspect, additional calculations were attempted for a wide range of level of flow blockage to cover such uncertainties.

## 2 MODELLING SCHEME

### 2.1 Hydraulic modelling

Figure 1 shows one of the four quadrants that make up the reactor core, which is composed of several fuel assemblies (FAs) having fuel rods. Each FA and each fuel rod have a different power and different burnup from the neighbouring FAs and fuel rods.

In the existing safety analysis of the NPP, LBLOCA has been calculated using a lumped system model, in which the core was modelled by one average channel and one hot channel. The former simulated all the FAs except one hot FA and the latter simulating one hot FA with one hottest rod. Moreover, all the inputs were prepared for the condition of the begin-of-life (BOL) of the first cycle, in which burnup of all the fuel rods were less than 5 Giga-Watts Days per Metric Tons of Uranium (GWD/MTU). Accordingly, the results of the calculation did not properly address the actual fuel rod behaviour at higher burnup conditions. As the burnup increases, the thermal conductivity of the pellet degrades, accordingly, the fuel stored energy increased at the same fuel power, and the peak cladding temperature (PCT) following a LOCA may increase. Therefore, the calculation considering the higher burnup has been strongly requested since other performance parameters might also be affected by the burnup.

To establish a regulatory position on these issues, a modelling scheme of multiple channels with multiple fuel rods reflecting the actual core design was developed by the author in their previous study [8]. As shown in the lumped system model of Fig. 1, several hydraulic channels can be used. The number of hydraulic average channel is determined by grouping of the FAs. An FA power ratio or an FA burnup level can be a grouping criterion. Each group has



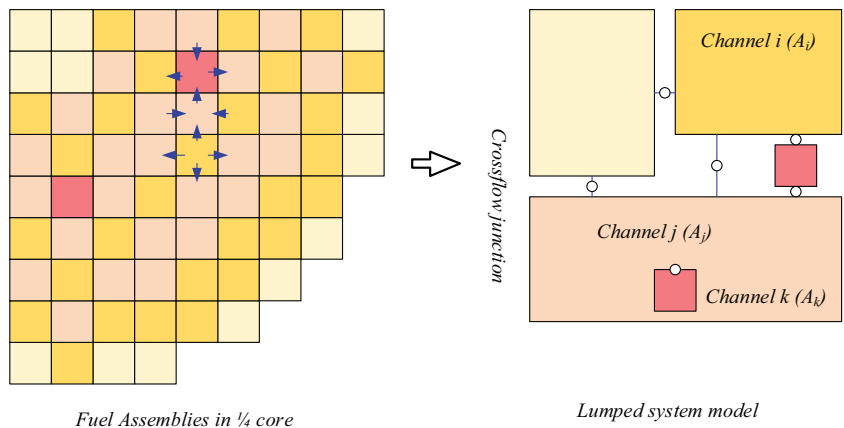*Fuel Assemblies in ¼ core*        *Lumped system model*

Figure 1: Reactor core modelling scheme.

one average channel with/without a hot channel and it is inter-connected with crossflow junctions. Several heat structures simulating the fuel rods within the group and the FA and special rods to be investigated can be allocated.

## 2.2 Flow blockage modelling

Figure 2 shows a concept of the flow blockage model. Consider the fuel rods in the FA $k$ was geometrically changed by swelling and rupture following an accident. Then the flow area change of the FA $k$ can be as follows:

$$F_k = A_k - A_{0k} = \sum_{i=1}^{n_k} \left( a_{k,i} - a_{0k,i} \right) = \sum_{i=1}^{n_k} \pi(r_{0k,i}{}^2 - r_{k,i}{}^2), \tag{1}$$

where $n_k$ denotes number of fuel rod per FA and subscript 0 mea initial state. If the rod was ruptured, then $a_{k,i} = 0$ is applied. The radius of the fuel rod cladding is calculated by the cladding deformation and rupture model [9] of the MARS-KS code.

Since eqn (1) is a sum of changes of area of all the rods in an FA and this equation will be applied to all the FA, tens of thousands of calculations on cladding deformation are needed. For convenience, it is assumed that the range of radial power peaking factor ($Fxy$) and burnup of the fuel rods can be subdivided into $M$ and $N$ sections, respectively, and the number of fuel rods corresponding to each section can be counted. Generally, the hydraulic channel $i$ has several fuel rods, thus, the change of flow area of the channel $i$ is as follows:

$$G_i = A_i - A_{0i} = \sum_{m=1, n=1}^{m=M, n=N} D_{i,m,n} f_{m,n}. \tag{2}$$

where, $m, n$ denote the section number of power and burnup and their maximums are $M$ and $N$, respectively. $D_{i,m,n}$ means a matrix of the number of fuel rod at the $m$-th burnup interval and the $n$-th peaking factor interval, and belonging to $i$ channel. And the area change of the fuel rod, $f_{m,n}$, can be calculated as follows:

$$f_{m,n} = a_{m,n} - a_{0m,n} = \pi \left( r_{0,m,n}{}^2 - r_{m,n}{}^2 \right), \tag{3}$$

Therefore, one can calculate the level of flow blockage due to swelling and rupture by (1) the information of initial cladding radius, power, and burnup for the entire fuel rods, (2)



*Fuel Rods in FA k before accident*          *Fuel Rods in FA k after accident*
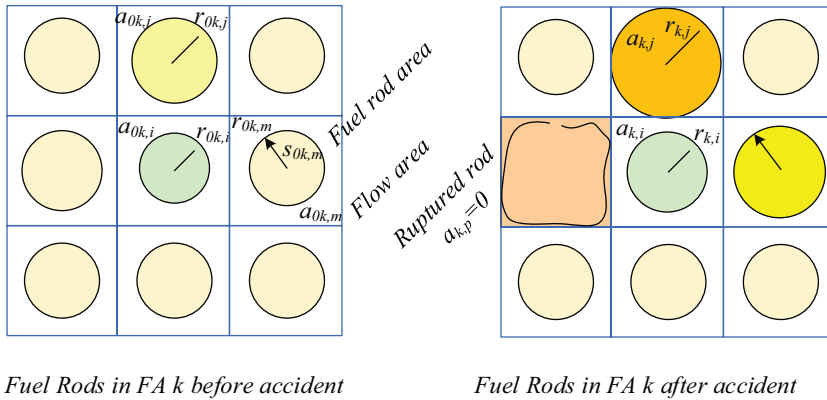
Figure 2: Concept of fuel rod swell and rupture model.

number of fuel rods at each section of power and burnup, and (3) cladding outer radius following an accident calculated by MARS-KS code. The level of the flow blockage can be implemented into the area change of the hydraulic channel using a SERVO valve model [4] of the MARS-KS code. The normalized value of $G_i$ of eqn (3) is used for that model.

### 3 PLANT CORE MODELING

The flow blockage modelling described above was applied to the core at the end-of-life (EOL) of Cycle 2 of Shinkori Unit 3 [10], the first plant of the advanced power reactor (APR) 1400. The multiple fuel rod modelling scheme was also applied. Based on the information provided by the fuel vendor [11], the reactor core was modelled by two groups (one average channel and one hot channel per each group) as shown in Fig. 3.

In total, 30 heat structures were used to represent the fuel rods as shown in Table 1 and Fig. 4. Some of the rods were for the flow blockage calculation (representative rods). Ranges
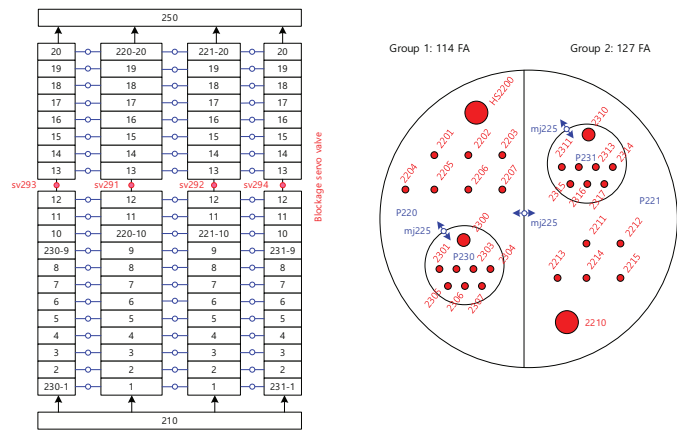


Figure 3: MARS-KS model for Reactor Core and Heat Structures.

Table 1: Radial peaking factors and burnup of heat structures.

| HS number | Description | Radial peaking factor, $Fxy$ | Burnup (GWD/MTU) |
|---|---|---|---|
| 2200 | Average rods in Group 1 | 1.1239 | 21.4 |
| 2201~2207 | Representative rods to Fxy/Burnup sections | 1.1, 1.2, 1.3, 1.2 1.3, 1.4, 1.45 | 25, 25, 25, 35, 35, 35, 35 |
| 2210 | Average rods in G-2 | 0.8846 | 34.06 |
| 2211~2215 | Representative rods | 1.1, 1.2, 1.1, 1,2, 1,1 | 35, 35, 45, 45, 55 |
| 2300 | Average rods in hot FA, G-1 | 1.3577 | 22.97 |
| 2301~2307 | Representative rods and hot rods | 1.1, 1.4, 1.45, 1.54, 1.54, 1.54, 1.4 | 15, 25, 25, 10, 20, 30, 40 |
| 2310 | Average rods in hot FA, G-2 | 1.0381 | 30.5 |
| 2311~2317 | Representative rods and hot rods | 1.1, 1.1, 1.2, 1.48, 1.28, 1.25, 1.18 | 25, 35, 35, 35, 40, 45, 50 |
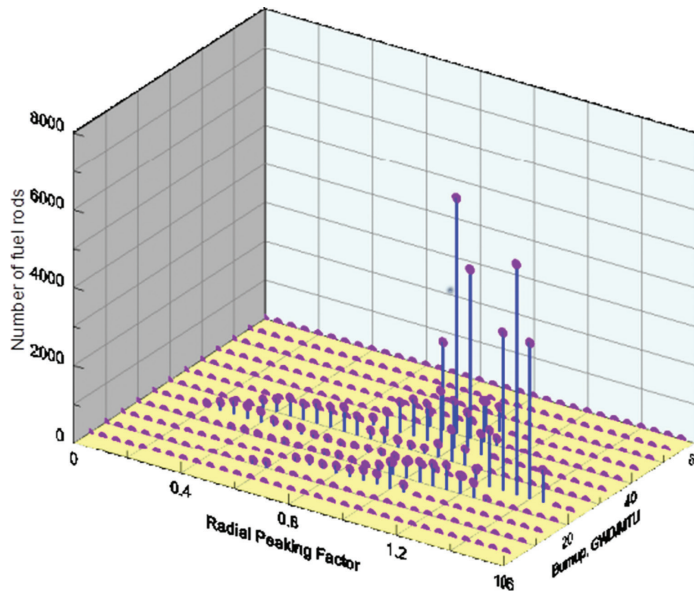
Figure 4: Burnup, radial peaking factors and number of
rods for each heat structure.

of burnup and *Fxy* were 10–55 GWD/MTU and 0.1–1.45 and discretized with intervals of
10 GWD/MTU and 0.1, respectively.

## 4  RESULT AND DISCUSSION

### 4.1  Base case

Figure 5 shows the calculated cladding radii of all the simulated fuel rods. As shown in the
figure, the rods having *Fxy* less than 1.1 even did not swell while others swelled and/or
ruptured. From the results, one can find the high powered rods in the Group 1 were
ruptured while the hot rods in Group 2 remained non-ruptured. This was due to the differ-
ence in fluid temperature outside the fuel rods, which was caused by the difference of *Fxy*
of hot FA.

The calculated flow blockage at all the hydraulic channels using those results is shown in
Fig. 6. As shown in the figure, flow area reductions were 10% and 86% at the average channel
and the hot channel of Group 1, respectively, while both were less than 1% in Group 2. Such
a high blockage at the hot channel of Group 1 was due to the conservatism in the assumption
of complete blockage of the flow area belonging to the ruptured rod, the division of the *Fxy*
and burnup sections, the estimation of the number of rods for each section, and the use of
conservative core decay model, ANS73 model [12], built-in the MARS-KS code.

Figure 7 shows a comparison of the cladding temperatures at 17 fuel rods of interest. The
presented calculation shows a significant difference in cladding heatup behaviour between
the fuel rods in the average channel and the rods in the hot channel, and also difference
between Group 1 and Group 2. Also the decrease of cladding temperature by return to nucle-
ate boiling during blowdown period was found in Group 2, which is due to the relatively
lower power. At the time of significant increase of blockage during 50–75 seconds (in Fig. 6),
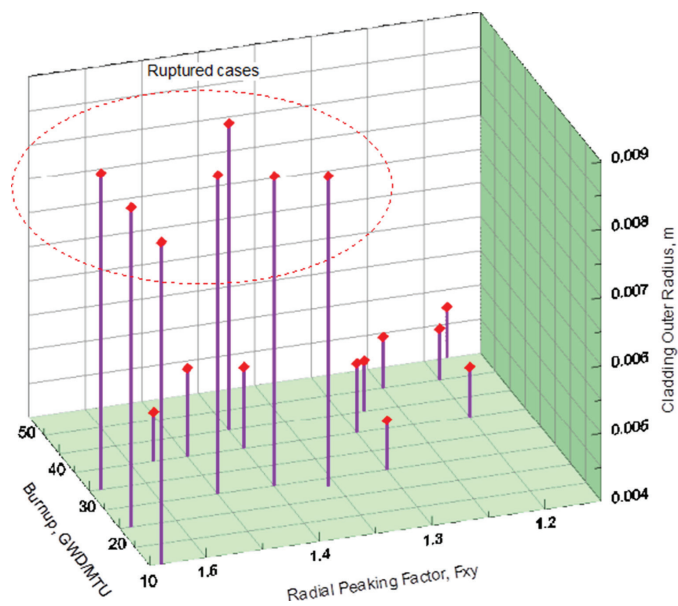
Figure 5: Calculated cladding radius.

one can find the decrease and re-increase in cladding temperature for the fuel rods at the hot channel. This can be regarded as an effect of flow blockage, i.e. a cooling by flow acceleration and a restriction of reflooding. One can find the effect of high blockage at the hot channel of Group 1, i.e. the heating up behaviour and delay in quenching time.

Figure 8 shows comparison of the calculated PCTs during blowdown phase and reflood phase versus *Fxy*, respectively. It is shown that PCTs increased as the *Fxy* increased and the burnup has a tendency to expand this increase. This trend is valid in PCT during the reflood phase with the exception of fuel rods in the hot FA of Group 2. The fuel rods have experienced the return to nucleate boiling, as shown in Fig. 7, which led to a quietly low reflood PCT.
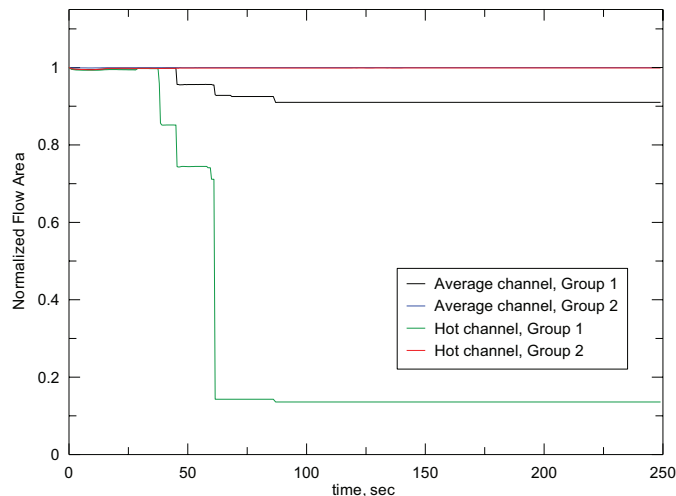


Figure 6: Calculated flow area.
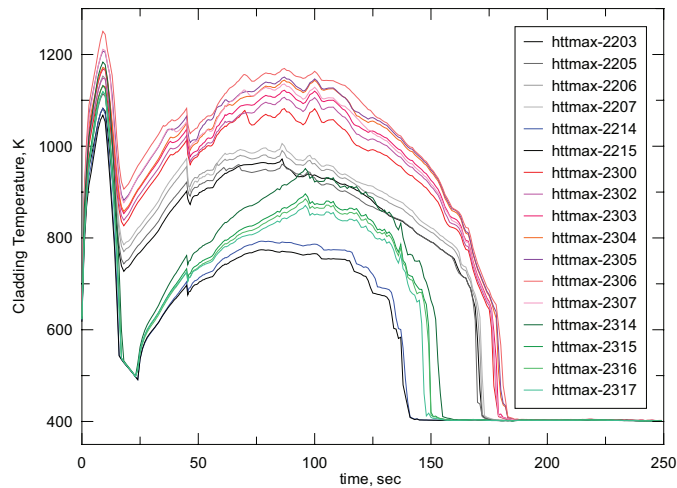
Figure 7: Calculated cladding temperatures.

Figure 9 shows the calculated oxide thickness of all the fuel rods. Similar to PCT, the transient oxide thickness increases as the *Fxy* and the burnup increase, and the maximum was less than 6 μm.

## 4.2  Sensitivity case

In the base case, the calculated change of cladding outer radius was directly implemented into the flow area change. As discussed, the estimate of blockage may involve uncertainties in several parameters such as the swell and rupture model of the code, the discretization of power and burnup, and the determination of the number of the fuel rods at each section. To compensate for those uncertainties, a sensitivity study was attempted regarding the several levels of blockage from 0% to 86 % of the flow area of hot channel.
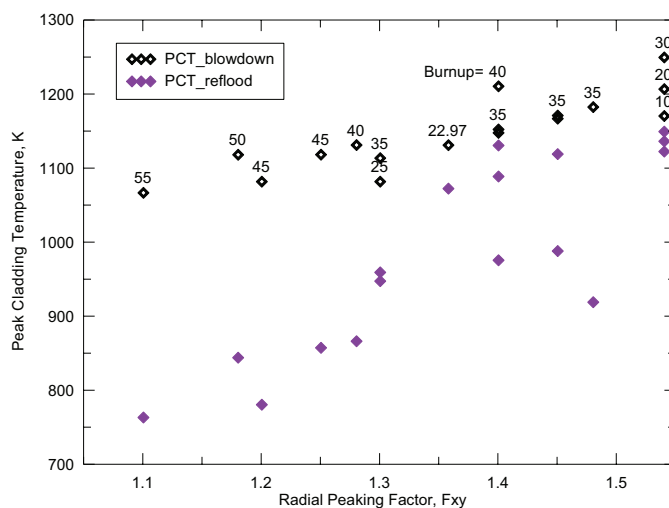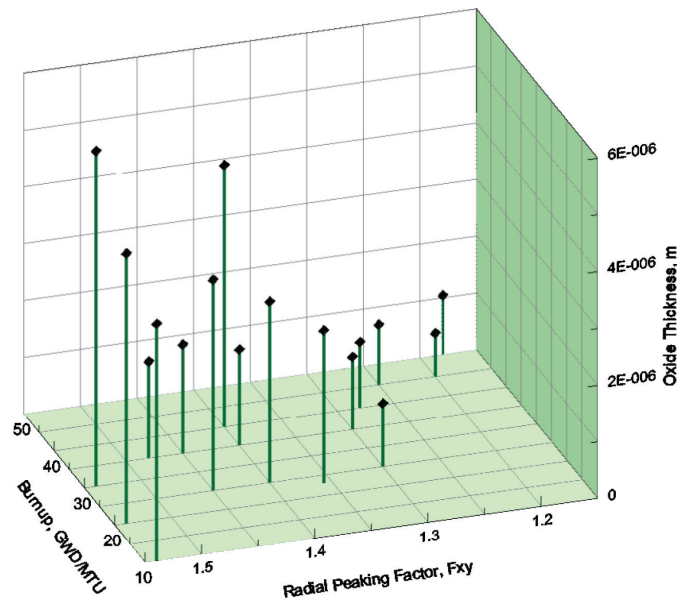


Figure 8: PCT versus *Fxy*.

Figure 9: Calculated oxide thickness.

Figure 10 shows a comparison of cladding temperature for seven cases of flow blockage. The blockage level was adjusted by decreasing the multiplier to the number of fuel rods. As shown in the figure, the PCT during blowdown was the same for all the cases, while the PCT during reflood was tended to increase by the blockage level with the exception of the interval around 40% (see Fig. 10b). Moreover, a significant increase in PCT was found at around 80% blockage. The unexpected result in the reflood PCT at 43% blockage was considered due to the interaction of several code models and needs a further study. Based on the above findings, the effect of flow blockage due to swelling and rupture from the no blockage to 86% blockage can be 40 K in reflood PCT.

As discussed above, the use of conservative core decay heat model was considered as one of the reasons for such a high blockage. To confirm it, a calculation was conducted with



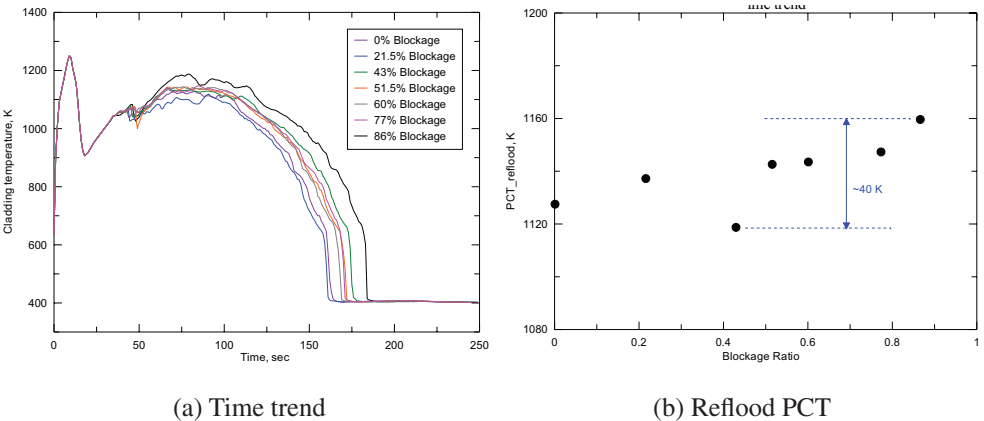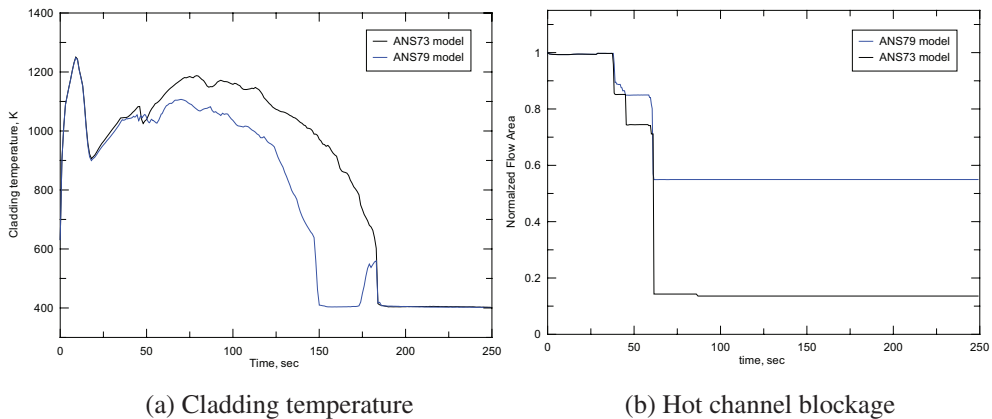(a) Time trend

(b) Reflood PCT

Figure 10: Cladding temperatures versus flow blockages.

(a) Cladding temperature　　　　　(b) Hot channel blockage

Figure 11: Cladding temperatures and flow blockage for two decay
heat models.

adopting ANS79 core decay heat model [4]. Figure 11 shows a comparison of cladding temperatures for two cases. As shown in the figure, a significantly low reflood PCT was predicted by the ANS79 model. The predicted flow blockage was shown in Fig. 11(b), which indicated only 45% blockage due to swelling and rupture. This means that the flow blockage due to the swelling and rupture is sensitive to the core decay power.

## 5  SUMMARY AND CONCLUSION

In the present study, a flow blockage modelling scheme was developed suitable for the calculation of large break LOCA using the system thermal-hydraulic code, MARS-KS. The modelling was setup such that the data of radial peaking factor and burnup of all the rods supplied by the core designer are divided into several sections. Moreover, the number of fuel rods corresponding to each section is determined with the combination of these two variables. The calculated cladding outer radii of the fuel rods in each section were used to calculate the level of flow blockage by introducing the servo valve model of the MARS-KS code. The present modelling scheme was applied to an analysis of a LBLOCA of an actual APR1400 NPP. The followings can be concluded:

1. Swelling and rupture were predicted for the fuel rods having a higher radial peaking factor and its magnitude was expanded by the level of fuel burnup. The level of the swelling and rupture was significant at the hot channel having a higher fluid temperature outside the fuel rods, i.e. higher hot channel peaking factor.
2. Flow blockage was predicted to be higher than 80% at the hot channel and the reflood PCT increased, in overall sense, by that level of blockage. The maximum impact on PCT increase was expected to be about 40 K for the range up to 86% blockage.

REFERENCES

[1] USNRC, Regulatory Guide 1.157, *Best-Estimate Calculations of Emergency Core Cooling System Performance*, Washington, D.C., USA, 1989.

[2] USNRC, *Compendium of ECCS Research for Realistic LOCA Analysis*, NUREG-1230, Washington, D.C., USA, 1988.

[3] USNRC, *Proposed Rule, Performance-Based Emergency Core Cooling Systems Cladding Acceptance Criteria*, (ADAMS Accession No. ML12283A174) Washington, D.C., March, 2014.

[4] KINS, *MARS-KS Code Manual, Volume II: Input Requirements*, KINS/RR-1282, Rev.1, 2016.

[5] Geelhood, K.J. & Lusher, W.G., *FRAPCON3.5: A Computer Code for the Calculation of Steady-State, Thermal-Mechanical Behaviour of Oxide Fuel Rods for High Burnup*, NUREG/CR-7022, May 2014.

[6] USNRC, *RELAP5/MOD3 Code Manual*, NUREG/CR-5535, Washington D.C., 2001.

[7] Zhang, H., Szilard, R., Epiney, A., Parisi, C., Vaghetto, R., Vanni, A. & Neptune, K., *Industry Application ECCS/LOCA Integrated Cladding/ Emergency Core Cooling System Performance: Demonstration of LOTUS-Baseline Coupled Analysis of the South Texas Plant Model*, INL/EXT-17-42461, Idaho Falls, USA, 2017.

[8] Bang, Y.S, et al, *Multiple Fuel Rods Modeling for LBLOCA Analysis of APR1400 under High Burnup Condition*, 27th International Conference of Nuclear Energy for New Europe, Portoroz, Slovenia, 2019.

[9] Powers, D.A. & Meyer, R.O., *Cladding Swelling and Rupture Models for LOCA Analysis*, NUREG-0630. April 1980.

[10] KHNP, *Final Safety Analysis Report, Shinkori Units 3 and 4*, KHNP, Seoul, Korea, 2015.

[11] KEPCO, N.F., *The Nuclear Design Report for Shin-Kori Nuclear Power Plant Unit 3 Cycle 2*, KNF-S3C2-18011, Rev.0 (Proprietary), Daejeon, Korea, 2018.

[12] American Nuclear Society, *Decay Energy Release Rates Following Shutdown of Uranium Fueled Thermal Reactors*, Draft ANS-5.1/N18.5, October 1973.

# EXPERIMENTAL AND COMPUTATIONAL STUDIES ON BIOMASS GASIFICATION IN FLUIDIZED BEDS

TOMMY BASMOEN, CHIDAPHA DEERASKA, CHIMUNCHE NWOSU, EBRAHIM QAREDAGHI, RAJAN JAISWAL, NORA C. I. S. FURUVIK & BRITT M.E. MOLDESTAD
University of South-Eastern Norway, Norway.

## ABSTRACT

The world's energy consumption is increasing, and research regarding utilization of renewable energy sources is crucial. Biomass for direct heating has been used for thousands of years, while in the last decades alternative ways to exploit biomass have emerged. In order to increase the efficiency and to produce more applicable products, gasification of biomass is becoming a more and more promising technology. For the gasification technology to be competitive, the understanding of the various aspects regarding the gasifier operation, which in turn influences the quality of the product gas, is of utmost importance. The main objective of this work is to investigate the effect of the air to biomass ratio on the produced gas composition in terms of the high-energy components $H_2$, $CH_4$ and CO. Experiments were performed with wood chips in a pilot scale gasification reactor. The results show that an air-to-biomass ratio less than one gives the most applicable gas composition. Biomass, like wood chips, has a peculiar shape, has a large particle size, is cohesive, and is therefore difficult to fluidize. In a fluidized bed gasifier, a bed material is used to improve the fluidization quality. Experiments were carried out in a cold bed model to study the fluidization properties of the bed material. Minimum fluidization velocities were predicted based on pressure drop in the bed.
*Keywords: Baracuda, biomass, bubbling fluidized bed, CPFD, gasification, multiphase flow.*

## 1 INTRODUCTION

The world's energy consumption is increasing, and research regarding competitive renewable energy sources is constantly crucial. The utilization of biomass for direct heating reaches back to thousands of years, while in the last decades alternative ways to exploit biomass have emerged. Burning biomass directly for producing steam, which in turn operates steam turbines, is frequently utilized. However, combustion of biomass gives limited efficiencies and field of application. In order to increase the efficiencies along with producing a more applicable product, gasification of biomass is becoming a more and more promising technology. For the gasification technology to be competitive, the understanding of the various aspects regarding the gasifier operation, which in turn influence the product quality, is of utmost importance. Different types of reactors can be used for biomass gasification, and this article focuses on bubbling fluidized bed gasifiers. Biomass, like wood chips, has a peculiar shape, has a large particle size, is cohesive, and is therefore difficult to fluidize. In a fluidized bed gasifier, a bed material (inert sand or particles with catalytic effect) is used to improve the fluidization quality. Fluidized bed gasifiers are used to achieve uniform material and heat distribution, and thereby enhancing the reaction rates and conversion efficiency of the biomass [1], [2], [3].

Gasification is a process where different types of biomass are converted into a combustible gas mixture, which has a variety of applications depending on the composition. The reaction temperature is typically 700–1100°C, and the supplied amount of oxygen should be kept relatively low to avoid combustion of the biomass. The biomass is converted into a product gas containing CO, $CO_2$, $H_2$, $CH_4$, $H_2O$ and tars. Tars are heavy hydrocarbons that usually condense at temperatures around 300°C, and ideally should be broken down into lighter components [4].

When fluidized beds are used for gasification of biomass, it is important to ensure that all the zones of the bed are kept in the fluidized regime during the entire operation time. It is therefore crucial to study the fluidization properties of the bed material. The aim of this work is to collect and analyze data from the operation of a gasifier. Special attention is put towards air flow to biomass ratio and the quality of mixing in the gasifier.

## 2  MATERIAL AND METHOD

Experiments are performed both in a cold fluidized bed and in a fluidized biomass gasifier.

### 2.1  Cold fluidized bed

Experiments are performed in a cold bed to study the fluidization properties. It is important to know at which velocity different types of bed materials start to fluidize, and the range of velocities that will keep the bed in the bubbling fluidized regime. Therefore, a cold bed can be used to study the fluidization behavior of the bed material used in a gasification reactor. The results can further be scaled to satisfy the conditions in the gasifier, or the gasifier conditions can be scaled to give the actual cold bed conditions. The results from the cold bed can also be used to verify a computational particle fluid dynamics (CPFD) model, which can be further used to simulate the flow behavior in the biomass gasifier.

The cold bed setup is presented in Fig. 1. The setup consists of transparent cylinder with a height of 1.63 m and a diameter of 0.084 m. Pressure sensors are installed along the height of the cylinder, and the distance between the sensors is 0.1 m. The cylinder is open to atmosphere at top. Desired amount of bed material is poured down from top to form an initially fixed bed. The air distributor is a porous plate and the location is indicated in the figure. The pressure sensor, P2, is located 0.035 m above the gas distributor. The pressure sensors are connected to a LabVIEW program, where the pressure data are logged and stored. The program also controls and registers the air flow rates.

Sand particles with mean diameter of 296 μm and 636 μm were used in the experiments. The mean diameter is determined from sieving analysis, and is based on mass. The density of
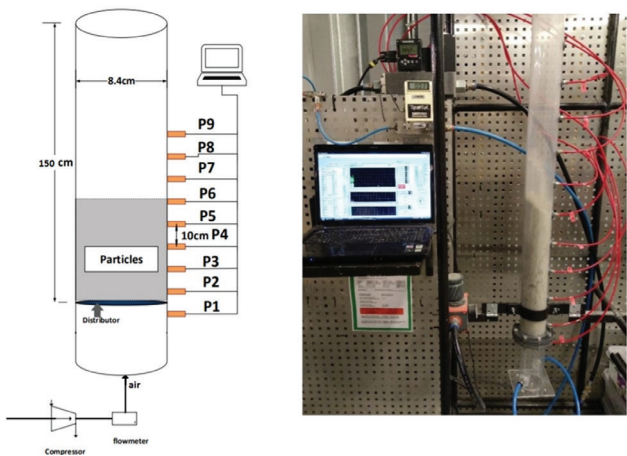


Figure 1: Experimental setup for the cold fluidized bed.

Table 1: Properties of sand particles and air.

| | |
|---|---|
| Particle density | 2,650 kg/m$^3$ |
| Particle sphericity (round sand) | 0.85 |
| Mean particle size (smaller particles) | 296 μm |
| Range of particle sizes (smaller particles) | 200–425 μm |
| Mean particle size (larger particles) | 636 μm |
| Range of particle sizes (larger particles) | 425–800 μm |
| Bulk density (smaller particles) | 1,398 kg/m$^3$ |
| Bulk density (larger particles) | 1,388 kg/m$^3$ |
| Air density | 1.225 kg/m$^3$ |
| Air viscosity | 1.78·10$^{-5}$ Pa s |
| Bed height | 0.21 m |

the sand particles is 2,650 kg/m$^3$. Air at ambient pressure and temperature was used as the fluidizing gas. The bed height was 0.21 m, which corresponds to an aspect ratio (bed height/diameter) of 2.5. The gas flow rate was varied stepwise to determine the transition from fixed to fluidized and bubbling bed. The bulk density was measured to be 1,398 kg/m$^3$ for the smaller particles and 1,388 kg/m$^3$ for the larger particles. The properties of air and sand are summarized in Table 1.

## 2.2 Gasifier

Experiments were also carried out in a pilot fluidized bed gasifier. The purpose of the experiments was to study the operation of a biomass gasifier and how the composition of the product gas was affected by different operational parameters. Special considerations for these experiments were put towards the air flow to biomass ratio. The experiments also aim to investigate whether proper mixing of biomass, bed material and air takes place in the reactor during the gasification process. The degree of mixing is evaluated based on the temperature in the reactor.

The experimental setup consists of a cylindrical column with a height of 1.0 m and an internal diameter of 0.10 m. To minimize heat loss, the inner wall of the bed reactor is coated with a refractory material. Electrical heaters are installed at the reactor wall to supply the heat needed during operation. The biomass, in this case wood chips, was fed to the reactor via screw conveyors. The conveyors were calibrated for the actual type of biomass before the tests. The flow rate of biomass is controlled from a programmable logic controller. Air was preheated and fed to the gasifier at a desired flow rate. The gasifier was preheated up to 300°C to avoid cold spots [5]. Samples of the product gas were taken regularly at intervals of 10 min. A gas chromatograph was used to analyze the samples with respect to the gas composition. Figure 2 shows a schematic illustration of the biomass gasification reactor. Specification of the gasification reactor and the operating conditions are summarized in Table 2.
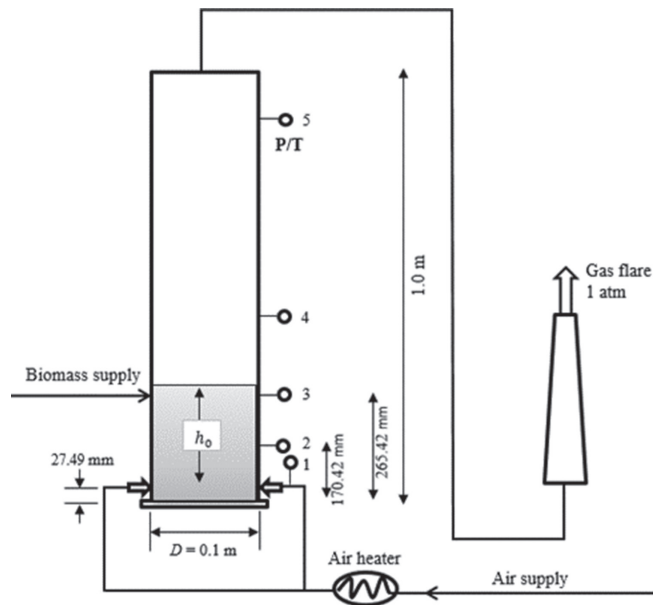
Figure 2: A schematic illustration of the biomass gasification reactor. P/T indicate pressure and temperature sensor probes and $h_0$ is the initial bed height above the air introduction points [6].

Table 2: Operational properties.

| Operational properties | |
| --- | --- |
| Bed height | 26.5 cm |
| Biomass feeding | 2 cm below top of the bed |
| Air feeding | 2 cm above bottom of the bed |
| **Bed material: Sand** | |
| Density (sand) | 2,650 kg/m$^3$ |
| Range of particle sizes (sand) | 400–750 μm |
| Mean particle size (sand) | 610 μm |
| **Biomass: Wood chips** | |
| Density | 411 kg/m$^3$ |
| Length | 5–12 mm |
| Width | 5–12 mm |
| Thickness | 1–5 mm |
| Shape | Rectangular |
| Mean diameter | $d_p = 6.87$ mm |
| Shape factor | 0.75 |

| Fluidizing agent: Air | |
|---|---|
| Air density (800°C) | kg/m$^3$ |
| Air viscosity (800°C) | Pa s |
| Air density (900°C) | kg/m$^3$ |
| Air viscosity (900°C) | Pa s |

## 3  RESULTS

This chapter presents results obtained from experiments in a cold fluidized bed and in a bio-mass gasifier. In addition, results from modelling and simulation of the cold bed and the gasifier are also presented.

### 3.1  Cold bed experiments

The experiments were performed with sand with a mean diameter of 296 μm and 636 μm to determine the minimum fluidization velocities and the range of velocities that can be used to keep the fluidization in the bubbling regime. The results are shown in Figs. 3 and 4 for the small and large particles, respectively. The results are presented as pressure drop per meter height of the particle bed versus superficial velocity. The minimum fluidization velocity is determined as the velocity when the pressure drop is at the maximum value. The minimum fluidization velocity is 0.09 m/s for the small particles and 0.33 m/s for the larger particles, which means that the minimum fluidization velocity increases significantly with increase in particle size. This is important to take into consideration when choosing bed material for the biomass gassifier. The bed containing small particles can be run in the bubbling regime at least up to a superficial velocity of 0.18 m/s. The tests with the larger particles were run with velocities up to 0.62 m/s, and the plot indicates that the bed will stay in the bubbling regime in the range of velocities from 0.33 m/s to 0.62 m/s.

### 3.2  CPFD modelling and simulation

The results from the cold bed experiments were further used to validate a CPFD model using the commercial software Barracuda VR 17.1.0. In Barracuda, the Eulerian approach is used
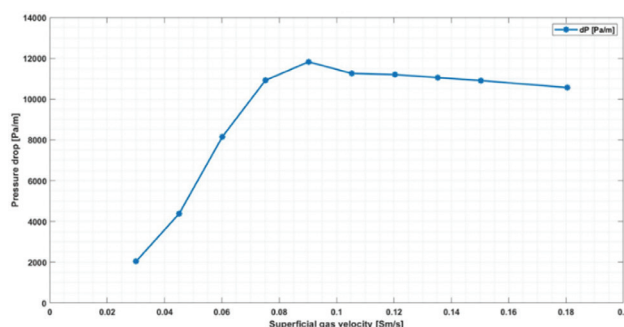


Figure 3: Pressure drop and minimum fluidization velocity from fluidization experiments using 296 μm sand, with aspect ratio of 2.5.
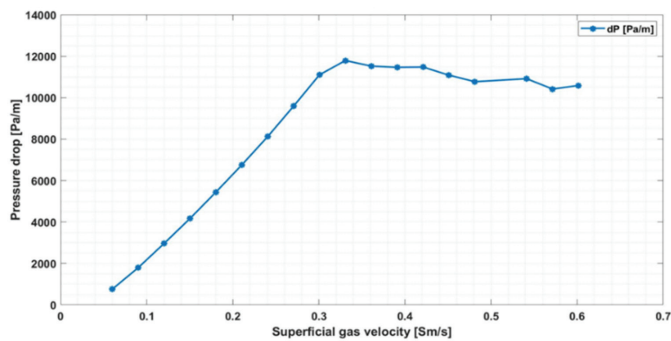
Figure 4: Pressure drop and minimum fluidization velocity from fluidization experiments using 636 μm sand, with an aspect ratio of 2.5.

for solving the fluid phase and the Lagrangian approach for the modelling of the particle phase [7]. The Wen and Yu drag model is used in the simulations [8]. The sphericity was set to 0.84 and the close pack volume fraction was set to 0.54. Detailed information about transport equations, solvers and model development in Barracuda is presented in [9], [10], [11]. The validation of the model is performed with particles with a mean diameter of 293 μm. The computational and experimental plots are compared in Fig. 5. The simulations agree very well with the experimental data regarding the minimum fluidization velocity and the pressure drop in the bubbling regime. Deviations are observed in pressure drop through the fixed bed, which may be due to variations in particle size distribution in the simulation compared to the experimental study. The deviation can also be due to the value of the maximum packing used in the simulated fixed bed. However, the model will be used to predict flow behavior in the bubbling
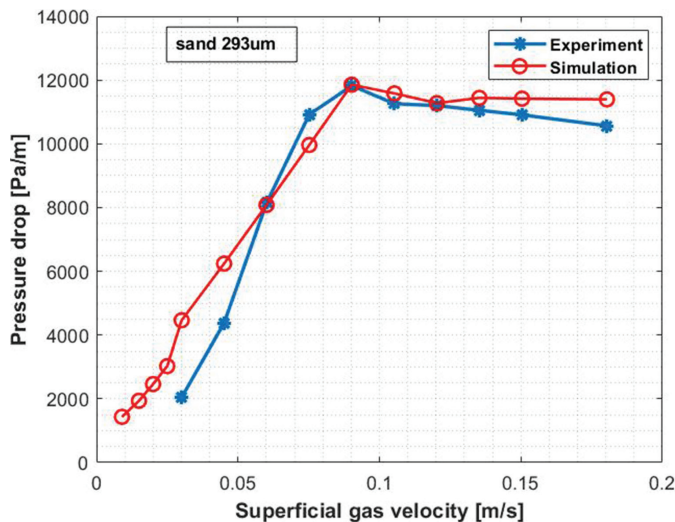


Figure 5: Comparison of experimental and simulated results; sand particles with a mean particle size of 293 μm.
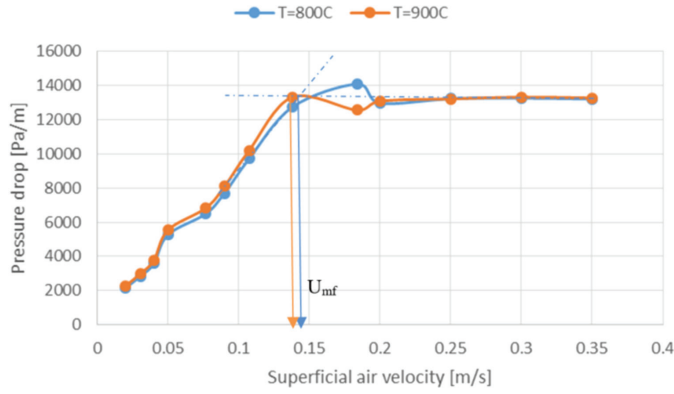
Figure 6: Pressure drop and minimum fluidization velocities from simulations using 610 μm sand particles, aspect ratio of 2.5 and temperatures 800°C and 900°C.

fluidized bed gasifier, and it is most crucial that the model is capable of predicting the bubble regime well.

The gasifier operates at temperatures between 800°C and 900°C. If small particles are used in the gasifier, entrainment of bed material may occur at the required gas flow rates. It was therefore decided to run the gasifier with sand particles with mean diameter of 610 μm as the bed material. Simulations based on the validated model were performed to find an acceptable range of gas velocities that could be used to keep the bed in the bubbling regime. The results are presented in Fig. 6. The minimum fluidization velocity is 0.144 m/s at 800°C and 0.138 m/s at 900°C. This indicates that it is necessary to run the gasifier at velocities well above 0.144 m/s to ensure that the bed is fluidized.

3.3  Gasification of biomass

Three different air-to-biomass ratios were used to study the effect on the composition of the product gas. The biomass flow rate was kept constant at 2.03 kg/h, whereas the air flow rates were 1.70 kg/h, 2.30 kg/h and 3.00 kg/h. The corresponding air to biomass ratios were 0.84, 1.13 and 1.48. The superficial velocities at 800°C and 900°C are presented in Table 3.

The total chemical reaction that occurs during the gasification process is an endothermic reaction, which implies that the process need heat supply. It is important to keep the oxygen supply low to obtain gasification and produce a high energy gas containing mainly CO, $H_2$ and some $CH_4$. If the air flow rate is too high, combustion or partly combustion will occur, and the product gas will contain more $CO_2$ and $H_2O$ and less of the gas components with high calorific value.

If cellulose $(C_6H_{10}O_5)$ is assumed to be the organic molecule in wood-chips, the stoichiometric air to biomass ratio can be calculated from:

$$C_6H_{10}O_5 + \left(6 + \frac{10}{4} - \frac{5}{2}\right)(O_2 + 3.76\,N_2) \rightarrow 6CO_2 + 5H_2O + (3.76 \cdot 6)\,N_2 \qquad (1)$$
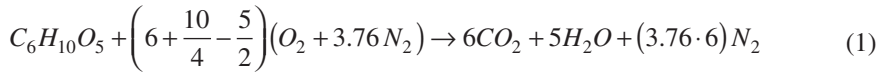
According to the balanced equation, the stoichiometric air to biomass ratio (mass of biomass/mass of air) is 5.08. The equivalence ratio, $\phi$, is the actual air to biomass ratio divided by the stoichiometric air to biomass ratio:

$$\phi = \frac{\left(\text{Air}\big/\text{Biomass}\right)_{\text{actual}}}{\left(\text{Air}\big/\text{Biomass}\right)_{\text{stoich}}} \tag{2}$$

The equivalence ratios for the gasification experiments are given in Table 3, and are low in all the experiments. Figure 7 shows the composition of the product gas for the three different air-to-biomass ratios. When the air-to-biomass ratio is low, the equivalence ratio is also low, and gasification is promoted. At air-to-biomass ratio of 0.84, the superficial gas velocity is about 20% above the minimum fluidization velocity at 800°C, and this velocity was considered as the lowest velocity that could be used to ensure fluidization. The results show that the content of $H_2$ and CO and $CH_4$ in the product gas decreases with increasing equivalence ratio, which is in agreement with the theory. However, the superficial gas velocity, and thereby the equivalence ratio has to be kept high enough to avoid defluidization. The temperature in the gasifier may vary with time, and it has to be taken into consideration that the minimum fluidization velocity increases with decreasing temperature.

The biomass gasification reactor is operated in the bubbling fluidized bed regime to achieve proper mixing in the gasifier. The degree of mixing in the gasifier influences on the quality of the product gas and proper mixing entails that the biomass is not accumulated in a part of the gasifier, but is evenly distributed in the reactor together with the bed material and the gas. Figure 8 shows the time averaged temperatures for different zones in the reactor, for the three different air-to-biomass ratios used in the experiments. The positions of the temperature sensors are shown in Fig. 2.

A good indication of the degree of mixing is the deviation in temperature over the gasifier. If a good mixing is achieved, the temperature will be rather constant over the entire bed. The highest air-to-biomass ratio (1.48) gives the lowest temperature deviation and hence the best mixing. The air-to-biomass ratio of 1.13 gives a constant value over the bed, but the temperature increases a little in the freeboard. The lowest air-to-biomass ratio (0.84) gives the largest temperature deviation in the reactor, which indicates that the mixing is not good enough.

Table 3: Gasification parameters.

| | | | |
|---|---|---|---|
| Air to biomass ratio (kg air/kg biomass) | 0.84 | 1.13 | 1.48 |
| Mass flow rate of air (kg/s) | 1.7 | 2.3 | 3.0 |
| Mass flow rate of biomass (kg/s) | 2.03 | 2.03 | 2.03 |
| Superficial gas velocity (m/s), $T = 800°C$ | 0.170 | 0.230 | 0.300 |
| Superficial gas velocity (m/s), $T = 900°C$ | 0.186 | 0.252 | 0.328 |
| Minimum fluidization velocity sand (m/s), $T = 800°C$ | 0.144 | 0.144 | 0.144 |
| Minimum fluidization velocity sand (m/s), $T = 900°C$ | 0.138 | 0.138 | 0.138 |
| Equivalence ratio | 0.17 | 0.22 | 0.29 |
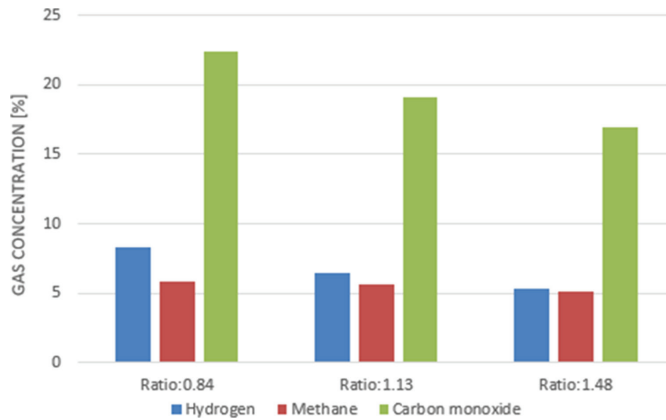
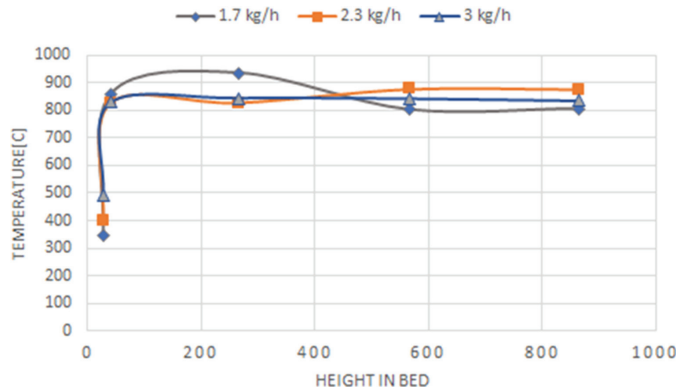Figure 7: Comparison of product gas composition for different air to biomass ratios.



Figure 8: Average temperature over bed height for varied air flow rate.

However, the lowest air-to-biomass ratio yields the product gas with the highest calorific value. More experiments are needed to study the degree of mixing in the gasifier.

## 4  CONCLUSION

The main objective of this work was to investigate the effect of the air to biomass ratio on the produced gas composition in terms of the high-energy components $H_2$, $CH_4$ and CO. Biomass, like wood chips, has a peculiar shape, has a large particle size, is cohesive, and is therefore difficult to fluidize. In a fluidized bed gasifier, a bed material is used to improve the fluidization quality. Experiments were carried out in a cold bed model to study the fluidization properties of the bed material. Minimum fluidization velocities were predicted based on pressure drop in the bed. The experimental results were used to validate a CPFD model using Barracuda. The validated model was used to predict the minimum fluidization velociy and the transition to the bubbling regime in a gasifier run at temperatures 800˚C and 900˚C. The data were used for gasification tests to ensure that the gasifier was operated in the bubbling

fluidization regime. The experiments were performed with wood chips in a pilot scale gasification reactor. The results show that a rather low air-to-biomass ratio of 0.84 gives the most applicable gas composition. More experiments are needed to study the degree of mixing at low air to biomass ratios.

## REFERENCES

[1] Zou, Z., Zhao, Y.L., Zhao, H., Zhang, L.B., Xie, Z.H., Li, H.Z. & Zhu, Q.S., Hydrodynamic and solids residence time distribution in a binary bubbling fluidized bed: 3D computational study coupled with the structure-based drag model. *Chemical Engineering Journal*, **321**, pp. 184–194, 2017. https://doi.org/10.1016/j.cej.2017.03.110

[2] Ghaly, A.E. & MacDonald, K.N., Mixing patterns and residence time determination in a bubbling fluidized bed system. *American Journal of Engineering and Applied Sciences*, **5(2)**, pp. 170–183. https://doi.org/10.3844/ajeassp.2012.170.183

[3] Timmer, K.J., *Carbon Conversion During Bubbling Fluidized Bed Gasification of Biomass*, Retrospective Thesis and Dissertations; Iowa State University: Iowa, 2008.

[4] Molino, A., Chianese, S. & Musmarra, D., Biomass gasification technology: The state of the art overview. *Journal of Energy Chemistry*, **25(1)**, pp. 10–25, 2016. https://doi.org/10.1016/j.jechem.2015.11.005

[5] Jaiswal, R., *Computational Modelling and Experimental Studies on Fluidized Bed Regimes*, Master Thesis, University of South-Eastern Norway, 2018.

[6] Agu, C.E., Pfeifer, C., Eikeland, M., Tokheim, L.A. & Moldestad, B.M.E., *Measurement and Characterization of Biomass Mean Residence Time in an Air-Blown Bubbling Fluidized Bed Gasification Reactor*, Revised and resubmitted to Fuel, 2019.

[7] Thapa, R.K. & Halvorsen, B.M., Stepwise analysis of reactions and reacting flow in a dual fluidized bed gasification reactor. *WIT Transactions on Engineering Sciences*, **82**, pp. 37–48, 2014. https://doi.org/10.2495/afm140041

[8] Wen, C. & Yu, Y., Mechanics of fluidization. *Chemical Engineering Progress Symposium Series*, **62**, pp. 100–111, 1966.

[9] Thapa, R.K., Frohner, A., Tondl, G., Pfeifer, C. & Halvorsen, B.M., Circulating fluidized bed combustion reactor: Computational particle fluid dynamic model validation and gas feed position optimization. *Computers & Chemical Engineering*, **92**, pp. 180–188, 2016. https://doi.org/10.1016/j.compchemeng.2016.05.008

[10] Chladek, J., Jayarathna, C.K., Moldestad, B.M.E. & Tokheim, L.A., Fluidized bed classification of particles of different size and density. *Chemical Engineering Science*, **177**, pp. 155–162, 2018. https://doi.org/10.1016/j.ces.2017.11.042

[11] Jayarathna, C.K., Moldestad, B.E. & Tokheim, L.A., Validation of results from Barracuda® CFD modelling to predict minimum fluidization velocity and pressure drop of Geldart A particles. *Proceedings of the 58th SIMS conference*, 2017.

# Author index

*This page intentionally left blank*

**WIT**PRESS  ...for scientists by scientists

# Computational and Experimental Methods in Multiphase and Complex Flow X

*Edited by:* **S. HERNÁNDEZ**, *University of A Coruña, Spain and* **P. VOROBIEFF**, *University of Nwe Mexico, USA*

Composed of papers presented at the 10th conference on Multiphase flow this book presents the latest research on the subject. The research included in this volume focuses on using synergies between experimental and computational techniques to gain a better understanding of all classes of multiphase and complex flow.

The presented papers illustrate the close interaction between numerical modellers and researchers working to gradually resolve the many outstanding issues in our understanding of multiphase flow.

Recently multiphase fluid dynamics have generated a great deal of attention, leading to many notable advances in experimental, analytical and numerical studies. Progress in numerical methods has permitted the solution of many practical problems, helping to improve our understanding of the physics involved.

Multiphase flows are found in all areas of technology and the range of related problems of interest is vast, including astrophysics, biology, geophysics, atmospheric process, and many areas of engineering.

The papers in the book cover a number of topics, including: Experimental measurements; Numerical methods; Multiphase flows and Flow in porous media.